MODELING THE ELASTIC PROPERTIES OF CARBON NANOTUBE ARRAYS AND THEIR COMPOSITES

By
Behnam Ashrafi
June, 2004

Department of Mechanical Engineering
McGILL University, Montreal, QC, Canada, H3A 2K6

A thesis submitted to
McGILL University
in partial fulfillment of the requirements for the degree of
Master of Engineering

Your file Votre référence
ISBN: 0-494-06542-7
Our file Notre référence
ISBN: 0-494-06542-7

Abstract

The superior mechanical properties of carbon nanotubes would make them excellent candidates for the next generation of composite materials. Researchers have tried to demonstrate the potential of that novel material with various degree of success. In order to complement the experimental efforts in this new field, the modeling of these new material systems is required. One challenge when modeling nanotube composites is the large scale span between the nanotube itself and the final component. The present study focuses on the creation of a framework and methodology to span three orders of magnitude in scale with interconnected models that relate performance of single-walled carbon nanotubes (SWNT) at the nanometer scale to a *nano-array*, *nano-wire* and *micro-fiber* with self-similar geometries. The geometry chosen is the helical array composed of discontinuous SWNT. The five elastic constants of the twisted SWNT fibers are then predicted using a finite element analysis combined with the strain energy method. It is shown that the Young's modulus of carbon nanotube fiber decreases dramatically even for small twist angles (less than *20°*) without any contribution to the transverse properties. Moreover, it was shown that adding the polymer and its properties can have important effects on the elastic properties of the SWNT/polymer fiber. Finally, this model is compared to the experimental data and theoretical models found in the literature.

Résumé

Grâce à leurs propriétés mécaniques supérieures, les nanotubes de carbone sont d'excellents candidats pour les nouvelles générations de matériaux composites. De nombreuses études ont été faites pour essayer de démontrer le potentiel de ces nouveaux matériaux avec plus ou moins de réussite. Afin de compléter les recherches dans ce nouveau domaine, une modélisation de ces matériaux et de leurs comportements doit être maintenant envisagée. Un des défis pour la modélisation des composites à nanotubes de carbone est la compréhension et l'intégration de la large différence d'échelle entre le nanotube et le composé final. La présente étude à pour objectif de déterminer une méthodologie pour décrire trois ordres de grandeur, de l'échelle nanométrique au nano-faisceau, nano-fil et micro-fibre, en utilisant des modèles décrivant les performances des nanotubes de carbone à paroi simple (single-walled carbon nanotubes SWNT) à géométries similaires. La géométrie choisie est la géométrie hélicoïdale composée de SWNT discontinus. Les cinq constantes élastiques des fibres en SWNT sont ensuite prédites par une méthode d'analyse par éléments finis combinée avec une méthode basée sur l'énergie de déformation. Il apparaît que le module d'Young des fibres en nanotubes de carbone diminue considérablement même pour de faibles angles d'hélice (inférieur à *20°*) sans aucune contribution des propriétés transverses. De plus, on peut remarquer que l'ajout d'un polymère et de ses propriétés dans le modèle numérique peut avoir un effet important sur les propriétés élastiques d'une fibre SWNT/polymère. Finalement, ce modèle a été comparé à des données expérimentales, et des modèles théoriques trouvés dans la littérature.

Acknowledgements

The author wishes to express his sincere gratitude to his master research supervisor, Professor Pascal Hubert, Assistant Professor, Department of Mechanical engineering for suggesting the topic of research, his extensive guidance, encouragement and support during this research.

Sincere thanks and appreciation goes to Professor Larry Lessard, Associate Professor, Department of Mechanical engineering for his helpful advices and corrections to drafts of the thesis.

Sincere thanks and appreciation goes to Dr. Gregory Odegard, Staff Scientist at the National Institute of Aerospace in Hampton, Virginia, for his valuable assistance, discussions and advices with the ANSYS programming used in this research.

Many thanks to Ms Loleï Khoun for her help for the abstract French translation, and to Mr. Eric St-Amant for the design of the figures showing the nanotube twisted arrays.

Finally, I would like to acknowledge the Canadian Natural Sciences and Engineering Research Council (NSERC) for their financial support.

Table of Contents

List of Tables

List of Figures

List of Symbols

Latin symbols

A	Cross section area
A^f	Dilute mechanical strain concentration tensor
A_{eff}	Effective cross section area
A_{NT}	Nanotube cross section area
A_t	Cross sectional area of carbon nanotube array
a	Graphite lattice constant
$\boldsymbol{a_1}$	first chirality vector
$\boldsymbol{a_2}$	second chirality vector
b	Carbon-carbon bond length
C^f	Fiber stiffness tensors
C^m	Matrix stiffness tensors
$\boldsymbol{C_h}$	Chiral Vector
C_{ij}	Stiffness constants
C_{ijkl}	Effective elastic modulus
c	Graphite interplanar spacing
c_n	perpendicular distance between tubes
D	Nanotube diameter
d	Tube distance
E	Beam elastic modulus
E_{22}, E_{33}, E_2, E_3	Transverse Young's modulus
E_a	SWNT array Young's modulus
E_c	Composite Young's modulus
E_{eff}	Effective Young's modulus
E_M	MWNT Young's modulus
E_m	Composite Young's modulus
E_f	Fiber Young's modulus

E_{NT}	Effective Young's modulus
E_n	SWNT Young's modulus
$E_n \mid_{D_n}$	Composite elastic modulus
E_r	SWNT reduced modulus,
F	Resultant axial force
f_s	Shape factor
G	Beam shear modulus
G_1, G_{12}, G_{13}	Axial shear modulus
G_g	Graphite shear modulus
$G_{z\vartheta}$	Transverse shear modulus
I	Identity tensor
I_1	Eshelby constant
I_3	Eshelby constant
I_c	Moment of inertia
i	Indicial notation
j	Indicial notation
K	Bulk modulus
K_{23}	Transverse bulk modulus
L	Beam suspended length
l	Layer thickness
M_w	Carbon atomic weight
m	First chirality constant
m_i	Atomic mass
N	Layer number
N_a	Avogadro's number
N_i	MWNT density constant
n	second chirality constant
Q	Eshelby constant
$q(x)$	Distributed applied load

R	Carbon nanotube fiber radius
R_n	Nanotube radius
R_{me}	MWNT external radius
R_{mo}	Internal radius
R_{na}	Array effective radius
R_{ne}	SWNT effective radius
r_i	Atomic spatial coordinates
S	Eshelby's tensor
s	Aspect ratio
T	Resultant torque
t	Turns per unit length
t_c	Nanotube layer thickness
u	Displacement
u_i^0	Averaged displacement
V	System empirical potential
V_a	Array volume fraction
V_f	Carbon nanotube volume fraction
V_n	carbon nanotube Volume fraction
W	Strain energy
w_0	Extensional strain
W_n	SWNT weight fraction
X_{CN}	Carbon nanotube properties
X_F	Fiber properties
X_P	Polymer index
x_j	Surface coordinates
Y	Graphite Young's modulus

Greek symbols

α	Helical angle
β_i	Beam constant
δ_B	Bending deflection
δ_{ij}	Kronecker delta
δ_S	Shearing deflection
ε_{kl}^0	Averaged strain
ε_{NT}	Nanotube strain
ε_{eff}	Effective fiber strain
ζ	Fiber geometry coefficient
θ	Carbon nanotube chiral angle
θ_i	Layer chirality
Λ	Nanotube radius constants
λ	SWNT array separation distance
μ	Van der Waals equilibrium distance
ν	Equilibrium standoff distance between the SWNT and the adjacent medium
v_f	Fiber volume fraction
$\xi(D)$	Probability distribution of nanotubes
ρ	Density
ρ_a	SWNT array density
ρ_m	MWNT density
ρ_n	MWNT Density
ρ_p	Polymer density
σ_{ij}^0	Averaged stress
v_0	Shearing strain
v_1, v_{12}, v_{13}	Axial Poisson's ratio
v_{23}	Transverse Poisson' ratio
$v_{Z\theta}$	Transverse Poisson's ratio

$\psi(D)$	Volume distribution of nanotubes per unit length
ω_i	Natural frequency

Chapter 1

Introduction

Nanoscale materials can be defined as those with characteristic length scale lying within the nanometric range, i.e. at least one dimension less than 100 nm, more typically less than 50 nm [1]. Within this length scale, the properties of matter are sufficiently different from individual atoms or molecules and from bulk materials that their study has been recently recognized as a new area of science, called *Nanoscience*. The term *Nanotechnology* relates to the ability to build functional devices based on the controlled assembly of nanoscale objects, for specific applications [2].

Nanotechnology has become an identifiable field of research and emerging applications in recent years. It is one of the most visible and growing research areas in materials science. Nanostructured materials include atomic clusters, layered films, filamentary structures, and bulk nanostructured materials [1]. One specific category of nanomaterial is *Nanocomposites*. The definition of nanocomposite material has broadened significantly to encompass a large variety of systems such as one-dimensional, two-dimensional, three-dimensional, and amorphous materials, made of distinctly dissimilar components and mixed at the nanometer scale.

The discovery of carbon nanotubes and their exceptional properties has the great potential to lead the next revolution in the development of high performance materials. Several research groups [3-10] have tried to make carbon nanotube/polymer fibers or plates. Because of the high cost of nanotubes, and the difficulties of making nanotube composites, the trial-and-error approach to developing these new materials can be very expensive and time consuming. Therefore, this work tries to investigate the elastic properties of carbon nanotube/polymer composites. Using the modeling approach will help in understanding the principal mechanisms that control the nanotube composite properties. This work is organized as follows:

An extensive review of the literature related to this work is presented in Chapter 2. In Chapter 3, a finite element model of the carbon nanotube fibers is presented and all elastic constants are determined by using a strain energy method. The question also whether the nanotube moduli change from the nanoscale to the microscale where conventional continuum mechanics is valid has to be answered. Therefore, in Chapter 4, the idea of *self-similar* analysis is used to relate the elastic properties of carbon nanotubes at the nanoscale to those of a carbon nanotubes/polymer fibers at the microscale. Next, the elastic properties of the polymer composites reinforced by a twisted carbon nanotube fiber are determined by using traditional micromechanics (Chapter 5). Finally, the results of this work are summarized in Chapter 6.

Chapter 2

Literature Review and Research Objectives

In this chapter, a review of the literature relevant to this research is presented. In Section 2.1, a brief review of the history of the discovery of the carbon nanotube is presented and two major microscopic technologies used to characterize nanotubes are presented. In section 2.2, a description of the different forms of carbon product is presented. The structure and properties of the carbon nanotubes are then introduced in Sections 2.3 and 2.4. In the following section, a review of three common methods to produce carbon nanotube is presented. Next, the characteristics of carbon nanotube bundles and their properties are given in Section 2.6. Then, in Sections 2.7 and 2.8, a summary of the experiments on the carbon nanotubes/polymer fibers and composites and three relevant nanotube composite models are summarized. Finally, the research objectives of this work are presented in Section 2.9.

2.1 Background

In 1985, Kroto *et al.* [12] used a high-powered laser to evaporate graphite and discovered a new carbon molecule, later called buckminsterfullerene (C_{60}) or simply the bucky ball, shown in Figure 2.1. The discovery of C_{60}, the third type of all-carbon crystalline structure other than the well-known graphite and diamond, marked the beginning of a new era in carbon science. Five years later, Krastschmer used a simple carbon arc instead of a high-powered laser to vaporize graphite in an atmosphere of helium to produce 90% of C_{60} [13]. The overall advantage of this method over the technique used by Kroto *et al.* was the possibility of bulk production of buckminsterfullerene.

In 1991, Iijima [14], an electron microscopist at NEC laboratories in Japan, discovered a new carbon molecule called the carbon nanotube. Iijima employed transmission electron microscopy (TEM) to study the soot produced by Krastschmer's technique. He accidentally discovered carbon nanotubes on the surface of the graphite cathode previously considered as "junk". Figure 2.2, an image of soot containing carbon

nanotubes, shows that carbon nanotubes are accompanied by other carbon products such as nanoparticles (hollow, fullerene-related structures) and some disordered carbon. The structure of the carbon nanotube consists of a long graphite cylinder closed at each end by one buckminsterfullerene molecule cut in half (Figure 2.3). In general, the nanotubes found by Iijima had lengths varying from a few tens of nanometers to several micrometers and outer diameters of 2-30 nm [15]. These carbon nanotubes, generally made of two or more graphite layers, were called multi-walled carbon nanotubes, MWNT. In 1993, Iijima and Ichihashi of NEC, and Donald Bethune of IBM independently reported the synthesis of single-walled carbon nanotubes, SWNT [15,16]. SWNT are made of a single layer of graphite sheet and have an outer diameter typically around 1 nm.

2.1.1 Experimental techniques

Because of the extremely small dimensions of carbon nanotubes, all aspects of carbon nanotube testing such as placing carbon nanotubes in proper testing configuration, applying proper load and finally measuring deformation are quite challenging. A brief review of the equipment used to observe and test carbon nanotubes is presented here.

Electron Microscopy (EM): Electron microscopes work exactly as optical microscopes except that they use a focused beam of electrons instead of light to "image" the specimen. EM can be used for different observations such as topology of a surface, morphology, composition and crystallographic information. They use high-energy electron beams in a range from several keV to several hundred keV. Because of the extremely short wavelength of electron, a fraction of an Angstrom or sub-nanometer resolution becomes possible. Two widely used types of electron microscopy are Transmission Electron Microscopy (TEM) and Scanning Electron Microscopy (SEM). In TEM, an accelerated electron beam from a thermal or a field emitter transmits through the sample and passes several electromagnetic lenses, and finally projects the image of the sample to a phosphor screen. In SEM, a nanoscale electron beam is rastered across the sample surface and the amplified image of the sample surface is formed by the signal from secondary electrons [32]. Figure 2.2 is an example of an image taken by TEM.

Atomic or Scanning Force Microscopy (AFM, SFM): Atomic force microscopes are widely used for studying carbon nanotubes mechanical behavior. They are considered as a standard tool for surface characterization of any material. An AFM consists of a force sensitive cantilever with a sharp tip with a radius of curvature around 10 nm. While scanning the sample surface in the x and y direction, the deflection of the cantilever is constantly monitored by a simple optical method. Controlling the deflection and keeping a constant contact force between the surface and the tip can achieve a surface profile of the sample. AFM can also be used to measure force-displacement behavior at the nanoscale.

2.2 Description of the different forms of carbon

A free carbon atom has an electronic structure $(1s)^2(2s)^2(2p)^2$ (see Appendix 1 for further explanation on the electronic structure). For covalent bonds, one of the *2s* electron is promoted to *2p*, and the orbitals can be hybridized in four possible configurations to produce four different carbon products: graphite, diamond, buckminsterfullerene, and nanotube.

2.2.1 Graphite

In graphite, one of the *2s* is hybridized with two of the *2p*'s and forms three sp^2 orbitals at 120° relative to each other in a plane, while the remaining orbital, p_z, remains perpendicular to the sp^2 plane (Figure 2.4). These three sp^2 orbitals form a strong σ-bond with other carbons in the graphite planes. On the other hand, p_z or π makes the Van der Waals bonds between planes. This π-bond is weak compared the strong σ-bond. The reason for graphite's high electrical conductivity is the overlap of π orbitals on adjacent atoms in a given plane. A single carbon layer of the graphite structure is also called *graphene*. The stacking sequence of the layers of graphite, mostly for either natural graphite or high-quality synthetic one, is generally *ABAB*, with an interlayer spacing of 3.355 Å, as can be seen in Figure 2.5. In less perfect graphite called turbostatic, this distance can be significantly larger than the value for single crystal (typically 3.44 Å), and layers are randomly rotated respect to each other, so *ABAB* stacking sequence cannot

be seen any more. Table 2.1 summarizes the structure and properties of the perfect graphite crystal.

2.2.2 Diamond

For diamond, each carbon atom is joined to four neighbors in a tetrahedral structure. The bonding here is sp^3 and results from the mixing of one *2s* and three *2p* orbitals; the angles between these bonds are 109° (Figure 2.6). Diamond is less stable than graphite so at the atmospheric pressure and a temperature of 1700°C, diamond is converted to graphite. Table 2.2 gives the characteristics of the diamond crystal.

2.2.3 Buckminsterfullerene

The most general form of buckminsterfullerene is C_{60}, also called the "bucky ball" in which 60 carbon atoms are bonded in an icosahedral structure made up of 20 hexagons and 12 pentagons (Figure 2.1). Each carbon atom in C_{60} is joined to three neighbors, so the bonding is sp^2 (same as graphite), although there may be a small amount of sp^3 due to the curvature. Because of Van der Waals forces, bucky balls tend to form clusters as shown in Figure 2.7. Table 2.3 gives the characteristics of buckminsterfullerene.

2.2.4 Carbon nanotubes

The bonding for carbon nanotubes is sp^2, although once again there may be some sp^3 in regions of high curvature. There are two possible symmetric structures for carbon nanotube called *zigzag* and *armchair* configurations (Figure 2.8). In practice, most carbon nanotubes never have these specific structures and form structures in which hexagons are arranged helically around the tube axis (Figure 2.9).

2.3 Carbon Nanotubes

2.3.1 Structure

The atomic structure of nanotubes is described in terms of the tube chirality, or helicity, defined by the chiral vector, C_h, and the chiral angle, θ. In Figure 2.10 by cutting the graphene along the dotted lines and rolling the remaining so that the tip and the tail of the vector C_h match, carbon nanotube helicity can be modeled. Two special cases, zigzag and armchair, are also shown. The chiral vector C_h can be described by the equation:

$$\vec{C}_h = n\vec{a}_1 + m\vec{a}_2 \tag{2.1}$$

where n and m ($n \geq m$) are two integers showing the magnitude of the unit vectors a_1 and a_2 ($m \neq n$ for chiral carbon nanotube, $m = 0$ for zigzag tubes and $m = n$ for armchair tubes). Since in graphene sheets, $\left|\vec{a}_1\right| = \left|\vec{a}_2\right| = 0.246\,nm$ the magnitude of the C vector is:

$$\left|\vec{C}\right| = 0.246\sqrt{n^2 + nm + m^2} \tag{2.2}$$

The chiral angle θ determines the amount of twist in the tube. The angle θ varies between 0° (zigzag) and 30° (armchair). Figure 2.11 shows these two special cases, zigzag and armchair. The chiral angle is given by:

$$\theta = \tan^{-1}\left(\frac{\sqrt{3}}{1+2n/m}\right) \tag{2.3}$$

Figure 2.12 shows the C vectors and θ angles for six different carbon nanotubes.

Moreover, multi-walled carbon nanotubes (MWNT) have several graphene layers. Figure 2.13 shows a 2-layer carbon nanotube. There are two models for describing structure of multi-walled carbon nanotubes. The first one is called nested or Russian-doll (Figure 2.14-a), while the other is called scroll-like or Swiss-rolled (Figure 2.14-b). Most experimental studies indicate that MWNT are nested or concentric [18] while a few have scroll-like structures [21]. The interlayer spacing can range from 0.34 nm to 0.39 nm

depending on the nanotube diameter; smaller diameter tubes have the largest spacing because of the higher repulsive intertube force as a result of higher curvature. If we consider that graphene tubes are separated by a distance of 0.34 nm then successive tubes should have a $2\pi \times 0.34 \approx 2.1$ nm difference in circumference. Therefore, it is not possible for zigzag structures forming successive tubes because 2.1 nm is not a precise multiple of 0.246 nm (the distance is equal to the first lattice parameter of graphite, a = 0.246 nm, shown in Figure 2.5). The closest approximation to the correct separation can occur when two successive tubes differ by 9 rows of hexagons (by a 0.352 nm distance) as can be seen in Figure 2.15. In this figure, three zigzag tubes form a multi-walled carbon nanotube. As can be seen 9 and 18 atoms are added respectively to form a three-walled carbon nanotube. It is also clear from Figure 2.15 that the *ABAB* stacking is not present in most part of the tube. On the other hand, in the case of armchair tubes, *ABAB* stacking can be maintained by considering a 2.1 nm circumference difference between each successive layer. A radial distance of 0.34 nm between every layer is possible since 2.1 nm is close to $5 \times 0.426 \approx 2.1$ nm (0.426 nm is the length of the repeat unit to form armchair tubes).

2.3.2 Geometry

By considering the carbon nanotube as a rolled graphite sheet, it is possible to theoretically calculate the radius of single-walled nanotubes. Figure 2.16 shows a schematic of a SWNT cross-section where the nanotube radius can be expressed by [23]:

$$R_n = \frac{b}{2\pi}\sqrt{3}\Lambda \tag{2.4}$$

where Λ is a function of m and n (helicity factors of carbon nanotubes) and, given by:

$$\Lambda = \sqrt{n^2 + m^2 + mn} \tag{2.5}$$

and, b is the *C-C* bond length ($b = 0.142$ *nm*). The effective radius, R_{ne}, can be expressed by:

$$R_{ne} = \frac{b}{2\pi}\sqrt{3}\Lambda + \frac{\nu}{2} \tag{2.6}$$

Several investigators have taken the SWNT equilibrium separation distance ν to be equal to that of graphene at about 0.34 nm. The SWNT length is a function of different parameters such as processing technique, purification method, handling and mixing of SWNT with the polymer [23]. A study by Dresselhaus *et al.* [63] reveals a distribution of lengths with a mean length of 480 nm while Thess *et al.* [64] have measured lengths of up to 20,000 nm.

The geometry of multi-walled carbon nanotubes can be expressed by the external radius (R_{me}), internal radius (R_{mo}), Van der Waals equilibrium distance (μ), and the number of layers (N) (Figure 2.17):

$$R_{me} = R_{mo} + N\mu \tag{2.7}$$

The internal radius R_{mo} can be expressed by:

$$R_{mo} = R_n - \frac{\mu}{2} = \frac{b}{2\pi}\sqrt{3}\Lambda - \frac{\mu}{2} \tag{2.8}$$

However, interlayer spacing (μ) is not constant and varies between 0.34 to 0.39 nm depending on the tube diameter [24]. Equation 2.9 can be used to compute the interlayer spacing as a function of the tube diameter (D) [24]:

$$\mu = 0.344 + 0.1e^{-D/2} \tag{2.9}$$

Table 2.4 shows the diameters of different single-walled and multi-walled carbon nanotubes obtained from Equations 2.6, 2.7 and 2.8.

2.4 Properties of carbon nanotubes

2.4.1 Mechanical properties

Young's modulus: From the Young's modulus of graphite and considering the carbon nanotube as a graphite layer rolled to form a tube, we can compute the Young's modulus of carbon nanotubes. The Young's modulus of graphite (Y) can be expressed as a function of stiffness constants C_{11} and C_{12} [24]:

$$Y = \frac{C_{11}^2 - C_{12}^2}{C_{11}} \tag{2.10}$$

The coordinate system used to define C_{11} and C_{12} is shown in Figure 2.5. Direction *1* is along the graphite layers while direction *2* is perpendicular to them. Now, by using an effective cross-section area for the carbon nanotube (Figure 2.18), the Young's modulus of the single walled carbon nanotube can be expressed by [23]:

$$E_n = \frac{8YR_n\nu}{4R_n^2 + 4R_n\nu + \nu^2} \tag{2.11}$$

Replacing R_n from Equation 2.4, E_n can be expressed by:

$$E_n = \frac{4\sqrt{3}\pi Y\Lambda\nu}{3b^2\Lambda^2 + 2\sqrt{3}b\pi\Lambda\nu + \pi^2\nu^2} \tag{2.12}$$

Based on [26] the Young's modulus of graphite, Y, is equal to 1.029 TPa. The result from Equation 2.12 is comparable with other work [25] where:

$$E_n = \frac{A}{R_n} + B \tag{2.13}$$

In Equation 2.13, A and B equal 429.6 GPa-nm and 8.42 GPa respectively. Figure 2.19 shows the variation of the Young's modulus as a function of different SWNT's diameters.

The relation for the Young's modulus of multi-walled carbon nanotubes is derived by adding the contribution of each layer as follows:

$$E_M = \frac{\sum_{i=1}^{N} Y(R_{ni} + \mu/2)^2 - (R_{ni} - \mu/2)^2}{R_{me}^2} \tag{2.14}$$

In this relation, R_{me} and R_{ni} are the outermost radius of the MWNT and the effective radius of each layer, while μ is the inter-layer thickness (Figure 2.20). Figure 2.21 shows the variation of MWNT's Young's modulus as a function of the tube diameter; meanwhile, Table 2.5 shows the Young's moduli for different carbon nanotubes.

Several methods were used to measure the Young's modulus of both SWNT and MWNT. Lourie *et al.* [27] used Raman Spectroscopy to measure the Young's modulus of nanotubes embedded in an epoxy matrix. They measured 1.7-2.4 TPa for MWNT and 2.8-3.6 TPa for SWNT. From tensile test of carbon nanotube bundles, Yu [28,29] obtained a Young's modulus ranging from 0.32 to 1.47 TPa for SWNT (mean: 1 TPa) and from 0.27 to 0.95 TPa for MWNT. These results are higher than those presented in Table 2.5, but when an effective cross section is defined for these tubes, as can be seen in Figures 2.18 and 2.20, these results become more comparable.

Several researchers used molecular dynamics (MD) to calculate the Young's modulus of carbon nanotubes. Robertson [30] used both molecular dynamics and a continuum shell model to determine a Young's modulus equal to 5.5 TPa for SWNT. Lu [31] used MD to calculate all five elastic constants necessary to illustrate the elastic behavior of both single-walled and multi-walled carbon nanotubes. A Young's modulus of about 1 TPa and a shear modulus of 0.5 TPa were calculated. He concluded that chirality, radius and number of walls have a little effect on the stiffness constants. As explained previously, this conclusion is based on the wall properties. Figures 2.19 and 2.21 show the predicted Young's modulus using the nanotube effective area. Yao [65] investigated the effects of both radius and helicity on the Young's modulus of single-walled carbon nanotubes using molecular dynamics (see Figure 2.22).

It is worth noting that a single value of Young's modulus cannot be uniquely used to describe both tension/compression and bending behavior of carbon nanotube, because tension/compression of carbon nanotubes is governed by in-plane σ-bond, while bending behavior is affected by out-of-plane π-bound [32]. Another method to calculate carbon nanotube Young's modulus is by using beam theory. Although carbon nanotubes have diameters only several times larger than their band length, they follow continuum relations very well [33]. For small deflections, the equation of motion based on Euler-Bernoulli beam [32] is still valid for carbon nanotubes:

$$\rho A \frac{\partial^2 u}{\partial t^2} + EI \frac{\partial^4 u}{\partial x^4} = q(x) \tag{2.15}$$

where u is displacement, ρ the density, A the cross section area, E Young's modulus, I moment of inertia and $q(x)$ a distributed applied load. The natural frequency of the i^{th} mode can be calculated by [32]:

$$\omega_i = \frac{\beta_i^2}{L^2}\sqrt{\frac{EI}{\rho A}} \tag{2.16}$$

For a clamped beam β_i can be given by:

$$\cos\beta_i \cosh\beta_i + 1 = 0 \tag{2.17}$$

This equation has roots: $\beta_1 \approx 1.875$, $\beta_2 \approx 4.694$, and $\beta_3 \approx 7.855$. Thus, one possible way to calculate Young's modulus of carbon nanotube is by using a vibrating beam theory model. Treacy [34] used this method to calculate Young's modulus for MWNT (1.8 TPa). Poncharal [35] used electromechanical excitation to get resonance of MWNT. He found a value in a range of 1 TPa for small diameter up to 12 nm, but for the larger diameter this value reduced to 0.1 TPa. This difference can be the result of differences between bending and compressive/tensile moduli as mentioned previously. Figure 2.23 shows scanning electron microscopy (SEM) image of a MWNT in its first two resonance frequencies [36].

Radial modulus: Shen [37] obtained deformability up to 46% by a *radial* indentation test of a 10 nm diameter MWNT with scanning probe microscopy. He also found the radial compressive elastic modulus of carbon nanotubes ranging from 9.0 to 80.0 GPa. Therefore, we can conclude that carbon nanotubes display a more compliant behavior in the radial direction than in the axial direction. In another investigation, Chesnokov [38] employed a quasi-hydrostatic pressure up to 3 GPa to calculate volume compressibility of SWNT and obtained a value of 0.0277 GPa that suggests the possibility of using nanotubes as an energy absorbing material.

Strength and ultimate strain: The distribution of defects and geometric factors can both influence the strength of carbon nanotubes. Buckling as a case for geometric failure has been examined by different researchers [39,40]. In theory, because of the small size of the carbon nanotubes, the defect density in carbon nanotubes is lower than in bulk materials [32]. Simple tensile tests have been performed to obtain the tensile strength of carbon nanotubes. Yu *et al.* [42] found strengths ranging from 13 to 52 GPa for 15 different SWNT ropes. Moreover, he obtained a maximum of 5.3% for the tensile strain at failure. In another investigation, Yu [42] performed tensile tests on individual MWNT (Figure 2.24). The failure mechanism was called the "sword-in-sheath" mechanism in which the inner layers were pulled out of the MWNT rope. A strain to failure of 12% and tensile strengths varying from 11 to 63 GPa were observed. This mechanism of fracture limits the application of the multi-walled carbon nanotubes for structural applications because only the outermost layer carries the load. This is explained by the difference between strong σ-bonds of graphene and weak Van der Waals bonds between shells. Wagner *et al.* [43] applied a tensile load on carbon nanotubes by embedding them in a polymer matrix. They reported a tensile strength of 55 GPa. Lourie *et al.* [44] performed compressive tests on carbon nanotubes and obtained a range between 100 and 150 GPa for compressive strength and a compressive strain at failure of slightly less than 5%. Yakobson *et al.* performed a set of molecular dynamics simulations to predict the tensile strength of carbon nanotubes [33, 35-47]. They reported strain to failure of 30% and strength of 150 GPa. In these simulations, even for very high strain rate, nanotubes did not break completely in half; instead two separated parts were still connected together

by a chain of atoms. Yu *et al* [48] obtained shear strength between the outermost layer and the neighboring inner layer for two different multi-walled carbon nanotubes varying from 0.08 to 0.3 MPa. These low values closely correspond to the strength of graphene.

2.4.2 Physical Properties

Density: The density of the SWNT is defined as the total mass of carbon atoms in the enclosed volume defined by R_{ne} in Equation 2.6. Here, we defined N as the number of carbon atoms per unit length:

$$N = \frac{4\Lambda}{3b} \tag{2.18}$$

Parameter Λ is defined in Equation 2.5 and b is carbon-carbon bond length. Therefore, the density of carbon nanotubes can be defined by [23]:

$$\rho_n = \frac{NM_w}{\pi N_a R_{ne}^2} = \frac{16\pi M_w \Lambda}{3N_a b(3b^2\Lambda^2 + 2\sqrt{3}b\pi v\Lambda + \pi^2 v^2)} \tag{2.19}$$

where N_a is Avogadro's number, v is the equilibrium standoff distance between the SWNT and the adjacent medium, and M_w is the atomic weight of carbon. Figure 2.25 shows the variation of the SWNT density as a function of the diameter.

A similar approach can be utilized to calculate the density of a MWNT (ρ_m).

$$\rho_m = \frac{\sum_{i=1}^{N} N_i k}{\pi R_{me}^2} \tag{2.20}$$

Here i refers to the i^{th} layer of the MWNT, and the number of atoms per layer N_i is defined as:

$$N_i = \frac{4\Lambda_i}{3b} \tag{2.21}$$

R_{me} can be obtained with Equation 2.7. The constant $k=0.01995$ is used to convert the density in g/cm^3 for ρ_m based on Avogadro's number and the atomic mass of carbon.

Weight fraction and volume fraction: In many situations, carbon nanotubes are mixed with polymers to form composites. In this case, the relation between the nanotube volume and weight fraction is useful. If we consider the density of the mixture ρ_m, the carbon nanotube density ρ_n, and the polymer density ρ_p, the carbon nanotube volume fraction (V_n) is defined as [25]:

$$V_n = \frac{\rho_m - \rho_p}{\rho_n - \rho_p} \tag{2.22}$$

By defining W_n as weight fraction, the relation between W_n and V_n becomes:

$$V_n = \frac{\rho_m}{\rho_n} W_n = \frac{W_n \rho_p}{W_n \rho_p + (1 - W_n)\rho_n} \tag{2.23}$$

Figure 2.26 shows the SWNT volume fraction versus the weight fraction for a polymer with $\rho_p=1\ g/cm^3$. As can be seen in this figure, the density of the *(18,18)* SWNT is closer to the density of the polymer ($1\ g/cm^3$) compared to the *(6,6)* SWNT.

2.5 Carbon nanotubes production

Several methods for making carbon nanotubes are reported in the literature [50-60]. The concept behind all the methods is similar. In general, an appropriate supply of energy, such as laser or electric arc, is used to locally evaporate carbon. In a proper environment containing a catalyst or an inert gas, carbon vapors can form carbon nanotubes. The most widely used methods are: arc-evaporation technique, laser ablation and chemical vapor deposition. These methods are explained in detail in the following sections. Others methods not described here such as the pyrolytic method [52,53] and the vapor condensation [54] are not as common as the previous ones.

2.5.1 Arc-evaporation Technique

A variety of different arc-evaporation reactors have been used for nanotube synthesis, but a stainless steel vacuum chamber with a viewing port is probably the most common [50]. A typical example is illustrated in Figure 2.27. The chamber is connected both to a vacuum line with a diffusion pump and to a helium supply. A continuous flow of helium at a given pressure is usually preferred over a static atmosphere of the gas. The electrodes are two graphite rods, usually of high purity, although there is no evidence that exceptionally pure graphite is necessary. Typically, the anode is a long rod approximately 6 mm in diameter and the cathode a much shorter rod of 9 mm in diameter. Efficient water-cooling of the cathode has been shown to be essential to produce good quality nanotubes. Furthermore, the anode has to be frequently cooled. The position of the anode should be adjustable from outside the chamber, so that a constant gap can be maintained during arc-evaporation. A voltage-stabilized DC power supply is normally used, and the discharge is typically carried out at a voltage of 20 V. The required current depends on the diameter of the rods, their separation, the gas pressure, but is usually in the range of 50-100 A. When the pressure is stabilized, the voltage is turned on. At the beginning of the experiment, the electrodes are not touching and no current will initially flow. The movable anode is then gradually moved closer to the cathode until arcing occurs. When a stable arc is achieved, the gap between the rods is maintained at approximately 1 mm or less; the rod is normally consumed at a rate of a few millimeters per minute. When the rod is consumed, the power is turned off and the chamber is cooled before opening. A number of factors have been shown to be important to produce a good yield of high quality nanotubes. Perhaps the most important is the pressure of helium in the evaporation chamber. Experiments show that a pressure of 500 Torr appears to be the optimum helium pressure for nanotube production. Another important factor is the current; too high a current will result in a hard, sintered material with few free nanotubes. Therefore, the current should be kept as low as possible, consistent with maintaining stable plasma. Efficient cooling of the electrodes and chamber has also been shown to be essential in producing good quality nanotube samples and avoiding excessive sintering.

2.5.2 Laser-vaporization method

In this method, a laser is used to vaporize a graphite target held in a controlled-environment oven as shown in Figure 2.28. The carrier gas used is helium or argon and the oven temperature is approximately 1200°C [51]. The condensed material is collected on a cooled target as shown in the diagram and typically contains a significant proportion of high quality nanotubes and nanoparticles. This method can also be used to produce single-walled nanotubes.

2.5.3 Chemical vapor deposition

Several research groups have used chemical vapor deposition to produce both single-walled and multi-walled carbon nanotubes [55-60]. In this method, nanotubes are formed by the decomposition of carbon-containing gases. Nikolaev [55] has described the gas-phase growth of SWNT by using carbon monoxide as a carbon-containing gas. The reaction that yields carbon nanotubes is: $CO+CO \rightarrow CO_2+C$ in the presence of an iron catalyst. Figure 2.29 shows the equipment layout where the flow channel is made of quartz. A range of pressure between 1-10 atm and a range of temperature between 800-1200° are used. Using a cooling system to keep the gases at low temperature before injecting into the furnace causes the production of nanotubes. The highest yield of SWNT was reported at the highest accessible temperature and pressure (1200°C, and 10 atm). This method has a great potential for large scale production of single-walled carbon nanotubes. Another technique for large-scale production of carbon nanotube uses hydrocarbons as carbon sources. Nikolaev pyrolized hydrocarbons on a surface heated to 700°C [55]. In this method because of the relatively low temperature necessary to make carbon nanotubes, it is possible to use different substrates such as glass or metal. In another experiment, Ren [60] used a silicon substrate coated with nickel to grow carbon nanotubes via plasma enhanced chemical vapor deposition. Here, acetylene (C_2H_2) gas is the carbon source and ammonia (NH_3) is the catalyst (Figure 2.30).

2.5.4 Comparison

Table 2.6 [90] compares four companies now producing carbon nanotube and gives the production rate, price, method and type of their production. As can be seen, the production rate of chemical vapor deposition is generally much higher than the arc discharge method. Moreover, the range of the price for both methods is comparable and depends mostly on the quality of the product. It is worth mentioning that production rate of the laser evaporation method is not comparable with the other two methods, but this method is very promising to produce high quality SWNT and MWNT [51].

2.6 Carbon nanotube bundles

Because of the weak Van der Waals forces between manufactured carbon nanotubes, they usually appear in the form of bundles or arrays rather than individual carbon nanotubes [32,61]. Figure 2.31 shows an image of nanotube bundle or array that appeared in a paper by Iijima [14]. An image analysis of the array done by Pipes and Hubert [61] reveals a volume fraction of 79% for hexagonal packing of the tubes (Figure 2.32). However, the theoretical maximum volume fraction for a hexagonal array is 0.906 [23]:

$$V_a = \frac{\pi}{2\sqrt{3}} = 0.906 \tag{2.24}$$

2.6.1 Carbon nanotube array properties

Figure 2.33 shows carbon a nanotube array (a) and an effective reinforcement array (b) in which each tube is replaced by solid one based on Figure 2.18. It is worth mentioning that effective radius R_{na} in Figure 2.33 is slightly different to that of a single-walled carbon nanotube, R_{ne} defined in Equation 2.6:

$$R_{na} = \frac{b}{2\pi}\sqrt{3}\Lambda + \frac{\lambda}{2} \tag{2.25}$$

The difference between two Equations 2.6 and 2.25 is that the separation distance for individual SWNT (v = *0.342 nm*) is replaced by the separation distance for arrays of

SWNT, λ. The separation distance λ is generally a function of the tube diameter and can vary from 0.316 to 0.319 nm [23]. Based on the definition for the effective radius R_{na} and the volume fraction V_a, it is possible to define the density (ρ_a) and the Young's modulus (E_a) of an array of single-walled carbon nanotubes:

$$\rho_n = V_a \rho_{na} = V_a \frac{NM_w}{\pi N_a R_{na}^2} = V_a \frac{16\pi M_w \Lambda}{3N_a b(3b^2\Lambda^2 + 2\sqrt{3}b\pi\lambda\Lambda + \pi^2\lambda^2)} \tag{2.26}$$

$$E_a = V_a \frac{4\sqrt{3}\pi Y\Lambda}{3b^2\Lambda^2 + 2\sqrt{3}b\pi\Lambda\lambda + \pi^2\lambda^2} \tag{2.27}$$

Equations 2.26 and 2.27 are similar to 2.19 and 2.12 respectively, except for an extra term: V_a multiplies the final product and ν is replaced by λ. Figure 2.34 shows difference between the Young's modulus of SWNT and SWNT's array. Similarly, the Young's modulus and the density relations of the MWNT's array only have an extra factor of V_a compared to the individual MWNT relations (Equations 2.14 and 2.20).

2.6.2 Measurement of elastic and shear moduli

The first measurement of the carbon nanotube array elastic properties was conducted by Salvetat *et al.* [75]. Crystalline ropes of SWNTs were produced by the arc-discharge method and purified by acid treatment and filtration. For direct measurements of the elastic properties of SWNT ropes, the rope was dispersed in ethanol and a droplet was deposited on a polished alumina membrane. Nanotubes occasionally lie over pores with most of the tube in contact with the membrane surface, producing a suspended beam configuration at the nanoscale. Figure 2.35-a) shows a SWNT rope of 20 nm diameter suspended over a 200 nm pore. An AFM tip operating in air was used to apply a load to the nano-array and to measure the corresponding deflection (Figure 2.35-b). Based on Timoshenko's beam theory [77], the total deflection of the beam (δ) can be expressed by:

$$\delta = \delta_B + \delta_S = \frac{FL^3}{192EI} + \frac{f_s FL}{4GA} \tag{2.28}$$

where L is the suspended length, E is the elastic modulus, f_s is the shape factor (equal to 10/9 for a cylindrical beam), G is the shear modulus, I is the second moment of area of the beam, and A is the cross-sectional area. Moreover, the deflection due to shearing (δ_S) has important contribution comparing to the deflection due to bending (δ_B) when [77]:

$$L/R \leq 4\sqrt{E/G} \tag{2.29}$$

Reduced modulus, E_r, equal to the elastic modulus when shearing is negligible, is presented for 10 ropes with different diameters in Table 2.7. By using an expression similar to Equation 2.12 and obtaining $E_{rope} \approx 600$ GPa, they were able to obtain the shear modulus of the ropes based on Equation 2.28 (Table 2.7).

In a recent work [76], Salvetat *et al.* have introduced stable links between neighboring carbon nanotubes within bundles by using a moderate electron-beam irradiation inside a transmission electron microscope. Their measurements of the mechanical properties using an atomic force microscope show a 30-fold increase of the bending modulus, due to the formation of stable crosslinks that effectively eliminate sliding between the nanotubes.

2.6.3 Lattice dynamics methods

Lattice dynamics methods have been developed to simulate material behavior at the molecular scale. While molecular dynamic methods were developed in the 1950's, they became popular in mid 1970's when digital computers became powerful [62]. These methods are essentially particle methods and their essence is to numerically solve the N-body problem of classical mechanics by using Newton's second law [32]:

$$m_i \frac{d^2\vec{r}}{dt^2} = -\nabla V \tag{2.30}$$

where m_i and r_i are the mass and spatial coordinates to the i^{th} atom respectively, V is the empirical potential for the system, and ∇ is the spatial gradient operator. In this method, an isolated system containing a certain number of molecules N in a fixed volume V is

considered. Because the system is isolated, the total energy E is also constant. These three constants N, V, and E determine the thermodynamic state of the problem.

Since hexagonal arrays are orthotropic with transverse isotropy (see Figure 2.31), five independent constants are necessary to completely model the elastic behavior of the carbon nanotube arrays. Popov [24] used force-constant molecular dynamics to calculate both Young's moduli and Poisson's ratios of crystals of carbon nanotubes (Figure 2.36). Table 2.8 illustrates how we can calculate Young's moduli and Poisson's ratios based on elastic constants. In these relations, direction *3* refers to the direction along the carbon nanotubes while directions *1* and *2* are transverse directions. As can be seen from Figure 2.36, these arrays show very anisotropic behavior. It is worth mentioning that the remaining constant G_{12} or G_{13} (G_{12}=G_{13}) and its correspondence C_{55} or C_{66} is not calculated with Popov's model.

2.7 Experiments on CNT fibers and composites

Several researches have tried to make composites with carbon nanotubes. While most of them have made composites with low concentration of carbon nanotubes (usually less than 10% by weight), a few groups have prepared composites containing highly-concentrated carbon nanotubes (up to 60% by weight).

2.7.1 High concentration fibers

Several researchers have produced polymeric fibers with high carbon nanotube volume fraction (about 60% by weight) and high degrees of the alignment. Gommans *et al.* [78] made well-aligned carbon nanotube fibers by dispersing nanotubes in a solvent called *N*,*N*-dimethylformamide. Then, a commercially available carbon fiber is attached to a conducting wire coupled to a motor-driven translation stage. The carbon fiber is immersed in the nanotube suspension to a depth of a few millimeters. The set-up is designed so that a voltage can be applied between the carbon fiber and the suspension. When a voltage is applied with the carbon fiber as the positive electrode, the nanotubes are attracted and form a cloud around the carbon fiber. Then, the carbon fiber is slowly withdrawn from the suspension. As it pulls out of the liquid, a nanotube fiber is formed

spontaneously from the nanotube cloud. With this method they were able to produce long fibers of several centimeters with diameters ranging from 2 to 10 μm. Vigolo *et al.* [3-5] used a simple spinning technique to produce aligned fibers. In this novel approach shown in Figure 2.37, a carbon nanotube dispersion is injected in a rotating container containing a solution of poly vinyl alcohol (PVA) polymer. The needle is oriented so that the SWNTs injection is tangential to the circular trajectory of the polymer solution. By using this method, they were able to produce CNT's fibers with a diameter of 35 μm, volume fraction of 50%, average twist angle of 15°, and Young's modulus of 40 GPa. Zhu [6] has grown well-aligned single-walled carbon nanotube fibers directly by catalytic pyrolysis method. In this method, n-hexane solution is catalytically pyrolyzed in a reactor at a temperature of 1423°K to produce a few centimeters long SWNT fibers with a diameter around 3 μm. Fibers produced by this method have a Young's modulus between 49 and 77 GPa (Figure 2.38). In another work, Baughman *et al.* [7] have produced SWNT fibers with a diameter of 50 μm and a weight fraction of 60%. Inspired by the work done by Vigolo [3], they used a type of coagulation-based carbon nanotube spinning method to prepare these fibers and they reported a Young's modulus of 80 GPa.

2.7.2 Low Concentration polymer composites

Several groups have tried to make fibers or film with low fractions of carbon nanotubes (usually less than 10% by weight). Perhaps, the most common challenging aspect was the carbon nanotube dispersion in the polymer matrix since carbon nanotubes tend to agglomerate because of Van der Waals forces. Different methods of dispersion were examined to improve the dispersion of the tubes into the matrix such as: shear mixing [8], twin-screw extruding [9], using solvent [10], and intercalation of polymeric adhesives [11]. Figure 2.39 shows the effect of carbon nanotube volume fraction on Young's modulus of CNT/PEEK (poly-ether-ether-ketone) composites. The results showed a linear increase of the Young's modulus with the volume fraction of carbon nanotubes. In this experiment, the Young's modulus of PEEK increased by 40% when 15% wt of carbon nanotubes (about 11% by volume) were added to the polymer.

The degree of the alignment in CNT/polymer composite has an important effect on the Young's modulus of the composite. Random dispersion of the carbon nanotubes into the polymer causes a slight increase in Young's modulus along any arbitrary direction. In other words, random dispersion produces composite films with isotropic behavior. On the other hand, the alignment of nanotubes in a chosen direction can significantly increase the stiffness in that direction. Thostenson and Chou [66] used a micro-scale twin-screw extruder to achieve dispersion of multi-walled carbon nanotubes in a polystyrene matrix. Highly aligned nanocomposite films were produced by extruding the polymer melt through a rectangular die and drawing the film prior to cooling, while random films were produced by using a hydraulic press. Figure 2.40 shows the importance of the alignment on Young's modulus of the nanocomposite film where the modulus increase of the aligned case is six times as high as that of the random case.

2.8 Carbon nanotube/polymer composite modeling

In order to gain a better understanding of the interaction between carbon nanotubes and polymers, the modeling of carbon nanotube composites has been the objective of several research efforts reviewed in this section.

2.8.1 Helical carbon nanotube arrays

Current SWNT synthesis methods primarily produce bundles of hexagonal-packed SWNT as can be seen in Figure 2.31. The stiffness and strength of these bundles are directly related to the load transfer between individual nanotubes. It is estimated that to achieve load transfer so that the entire cross-section of the bundle becomes effective, the SWNT contact length must be on the order of 10 to 120 μm [32]. However, the typical length of carbon nanotubes is only several hundred nanometers [64]. A theoretical study done by Qian [67] shows that twisting can significantly decrease the required contact length for complete load transfer. Based on textile mechanics, applying a twist to the tubes and hence producing radial force between adjacent tubes can result in better load transfer and, consequently, better mechanical properties for the resulting carbon nanotube rope. Moreover, when a tube in a twisted rope breaks, it still can bear load transferred

from the other tubes because of strong radial friction forces. Therefore, considering discontinuous, twisted carbon nanotube fibers as tubes with infinitive length seems like a possible solution to the nanotube "short length" problem.

The degree of helicity of a fiber containing twisted nanotubes can be characterized by the number of turns per unit length t [68]. Moreover, these fibers are assumed to follow helical path along the length of the rope while the tangent of the helical angle of the fiber is linear function of its radial position and varies from 0 at the rope axis to α at the rope outer surface:

$$\tan\alpha = 2\pi Rt \tag{2.31}$$

where R is the outer radius of the rope.

Pipes and Hubert [61] employed textile mechanics and anisotropic elasticity theory to model the elastic behavior of fibers made of collimated carbon nanotubes. The fiber was modeled as a layered cylinder shown in Figure 2.41 in which every layer consists of discontinuous carbon nanotubes embedded in a polymeric matrix. The determination of the effective axial Young's modulus and Poisson's ratio may be accomplished by applying an extensional strain, w_0 to the model (Figure 2.41) and determining the resultant axial force, F while enforcing the resultant torque T vanishes at extremity. A similar method can be used to determine the axial shearing modulus. Here, a shearing strain v_0 is applied to the model and the resultant torque T is determined while enforcing the condition of zero axial force, F. This method, called relaxation, can be effective to calculate three constants out of the five necessary constants required to model elastic behavior of orthogonal transversely isotropic cylinder shown in Figure 2.41.

Four coefficients A, B, C, and D are necessary to relate T and F to v_0, w_0.

$$\begin{bmatrix} A & B \\ C & D \end{bmatrix} \begin{bmatrix} v_0 \\ w_0 \end{bmatrix} = \begin{bmatrix} T \\ F \end{bmatrix} \tag{2.32}$$

These four coefficients can be determined as follows:

$A=T$ when $v_0=1$ and $w_0=0$.

$C=F$ when $v_0=1$ and $w_0=0$.

$B=T$ when $v_0=0$ and $w_0=1$.

$D=F$ when $v_0=0$ and $w_0=1$.

Now, to determine axial Young's modulus and Poisson's ratio, the proper boundary conditions are:

$$v_0 / w_0 = -B/A,\ T = 0 \tag{2.33}$$

Therefore, the axial Young's modulus and the Poisson's ratio can be expressed by:

$$E_z = \frac{F}{\pi R^2 w_0} \tag{2.34}$$

$$v_{z\vartheta} = -\frac{u_{r=R}}{R w_0} \tag{2.35}$$

Similarly, the boundary conditions defined in Equations 2.36 and 2.37 can be used to determine axial shearing modulus:

$$v_0 / w_0 = -C/D,\ F = 0 \tag{2.36}$$

$$G_{z\vartheta} = \frac{2T}{\pi R^4 v_0} \tag{2.37}$$

Figure 2.42 shows the Young's modulus of the rope as a function of helical angle. In this figure, two other cases with no shear strain ($v_0=0$) and also with alternate helical angles $\pm 20^\circ$ for the rope layers are shown. Figure 2.43 shows the axial shearing modulus and the Poisson's ratio for a layered cylinder. As can be seen from Figures 2.42 and 2.43, the helical angle has an important effect on the fiber properties.

2.8.2 Constitutive modeling of nanotube/polymer

Interaction of carbon nanotubes and polymer is a primary challenge to model the behavior of their composite, since at small scales traditional micromechanical approaches are no longer valid. Odegard *et al* [69] used an equivalent-continuum modeling method to model the nanotube, the local polymer near the nanotube and polymer/nanotube interaction. As can be seen in Figure 2.44, a suitable representative volume element (RVE) is chosen for the model. Molecular dynamics (MD) was used to simulate the interaction between the polymer (LaRC-SI) and a (6,6) single-walled carbon nanotube. In summary, the atomic lattice has been viewed as an assemblage of discrete masses that are held in place with atomic forces that resemble elastic springs. The mechanical analogy of this model is a pin-jointed truss model in which each truss represents either a bonded or non-bonded atomic interaction. Next, the total strain energy of both truss model (middle of Figure 2.44) and the continuum model (right of Figure 2.44) is equal under identical loading conditions. By applying proper loading conditions, it is possible to calculate all elastic constants (five sets of boundary conditions to determine five stiffness constants). Finally, traditional micromechanics was utilized to determine the elastic properties of a polymer film reinforced by these fibers. Figure 2.45 shows the effect of carbon nanotube alignment and length on both shearing modulus and Young's modulus for a CNT/Polymer composite with a nanotube volume fraction of 1%. Constant k in Figure 2.45 describes the relative amount of alignment of the fibers with respect to the major axis of the composite film ($k= 0$ for completely random case, $k\rightarrow\infty$ for perfectly aligned case). Moreover, Figure 2.46 shows the effect of the SWNT volume fraction on composite properties.

2.8.3 Micromechanics modeling of the MWNT/polymer composite

Thostenson and Chou [70] utilized traditional micromechanics to model the elastic behavior of unidirectional composites made of multi-walled carbon nanotubes. Because of the weak layer-to-layer interaction in multi-walled carbon nanotubes, they considered that only the outermost layer will carry the load at the polymer/matrix interface. Based on this consideration they defined effective properties of MWNT as a fiber similar to

Figure 2.19, except that here the effect of internal layers of graphene was ignored (Figure 2.47). By considering iso-strain conditions:

$$\varepsilon_{NT} = \varepsilon_{dff} \tag{2.38}$$

where the subscripts (*NT*) and (*eff*) refer to the nanotube and effective fiber, respectively. By using Hooke's law, we have:

$$E_{dff} = \frac{A_{NT}}{A_{eff}} E_{NT} \tag{2.39}$$

where A is the area. By considering the nanotube outer layer thickness ($t_c = 0.34\ nm$) and the nanotube diameter D when ($t_c/D < 0.25$):

$$E_{dff} = \frac{4t_c}{D} E_{NT} \tag{2.40}$$

In order to model MWNT/polymer composite, tradition micromechanics of Halpin and Tsai [71] was used in which the Young's modulus of the composite (E_c) is given by:

$$E_c = E_m \left(\frac{1 + \zeta \eta V_f}{1 - \eta V_f} \right) \tag{2.41}$$

$$\eta = \frac{(E_f / E_m) - 1}{(E_f / E_m) - \varsigma} \tag{2.42}$$

where V_f is volume fraction of carbon nanotube, and E_f and E_m are Young's moduli of fiber and matrix respectively. The parameter ζ is dependent on the geometry and the boundary conditions of the reinforcing phase. For the case of aligned short-fiber composites, ζ can be expressed by:

$$\varsigma = 2\frac{l}{D} + 40V_f \tag{2.43}$$

For a low volume fraction (V_f) the second term is negligible compared to the first term. Equations 2.39 to 2.43 can express the elastic behavior of the composite as a function of the nanotube diameter. Since carbon nanotubes produced by different methods have different ranges of diameters, the distribution of nanotube diameter has to be determined by considering statically large sample of nanotubes. By considering the probability distribution of nanotubes, $\xi(D)$, volume distribution of nanotubes per unit length, $\psi(D)$, can be determined by:

$$\psi(D) = \frac{D^2 \xi(D)}{\int_0^\infty D^2 \xi(D) d(D)} \tag{2.44}$$

This volume distribution can be used when calculating the overall nanocomposite properties. In their model, they used the concept of parallel composites as can be seen in Figure 2.48 where the entire volume of the composite is divided into N individual composites containing a specific nanotube diameter. Then, the composite Young's modulus can be defined by:

$$E_c = \sum_{n=1}^{N} v_n E_n|_{D_n} \tag{2.45}$$

where $E_n|_{D_n}$ is the elastic modulus of composite calculated by Equation 2.41, and v_n is partial volume of the n^{th} composite. Figure 2.49 shows the results for different tube length, diameter and two volume fractions (2.5% and 5.0%). This model shows that the diameter has a significant effect on the composite elastic modulus.

2.9 Research objectives

In Section 2.4, it was shown that carbon nanotubes have exceptional elastic properties. However, the nanotube dimensions of the order of a few nanometers in diameter and a few hundreds of microns in length have put huge unsolved challenges before researchers. Perhaps, the most common challenging aspect is the carbon nanotube dispersion in the polymer matrix since carbon nanotubes tend to agglomerate because of Van der Waals forces (Section 2.7.2). Most practical experiments on carbon nanotube/polymer

composite reviewed in Section 2.7 showed the existence of carbon nanotube arrays instead of individual tubes because of Van der Waals interactions. It was estimated that to achieve load transfer so that the entire cross-section of the bundle becomes effective, SWNT contact length must be on the order of 10 to 120 μm [32]. Since the typical length of the carbon nanotubes are significantly less than this range, one possible way to increase the load transfer between tubes is by applying a twist to them similar to what is done in textile fibers. A theoretical study done by Qian [67] showed that twisting could significantly decrease the required contact length for complete load transfer. In a recent work done by Windle *et al.* [89], a direct spinning method was used to make twisted nanotube fibers from chemical vapor deposition. In this method, continuous carbon nanotubes formed in the furnace and by using a rotating rod aligned at 25° to the furnace axis (Figure 2.50-a), they were able to form twisted carbon nanotube fibers. By using this method, they were also able to make carbon nanotube fibers with a twist angle of zero (Figure 2.50-b).

In light of the issues described above, our research objectives are divided into three topics:

Helical carbon nanotube fiber properties

In Section 2.8, Pipes and Hubert employed textile mechanics and anisotropic elasticity theory to model the elastic behavior of fibers made of collimated carbon nanotubes. By using this method, they were able to obtain three out of five constants necessary to describe the elastic behavior of the fiber. In Chapter 3, a finite element model of a layered cylinder of helical carbon nanotube fibers is developed and a strain energy method is proposed to obtain all five fiber elastic constants as a function of the twist angle.

Nanotube properties from the nanoscale to the microscale

As reviewed in Section 2.4, carbon nanotubes have extraordinary high Young's modulus at the nanoscale. The question whether the nanotube moduli change from the nanoscale to the microscale, where conventional continuum mechanics is valid, has to be answered.

Therefore, in Chapter 4 the idea of *self-similar* analysis is used to relate the elastic properties of carbon nanotubes at the nanoscale to those of carbon nanotube/polymer fibers at the microscale. In this approach, the elastic properties of carbon nanotube crystals from Section 2.6.3 are considered as inputs to the model. Then, energy methods and conventional micromechanics are used to determine the elastic properties of carbon nanotube/polymer fibers at different scales. Moreover, these results are compared to the experimental data presented in Section 2.7.1.

Nanotube array polymer composite properties

Finally, in Chapter 5 the elastic properties of the polymer composites reinforced by a twisted carbon nanotube fiber are determined by using traditional micromechanics, and the effects of different parameters such as the degree of the alignment, the twist angle and the volume fraction of the SWNT on the polymer composite are examined and this model is compared to the constitutive mode of nanotube- polymer composite reinforced with individual SWNT (Section 2.8.2).

Table 2.1

Characteristics of graphite crystals

Space Group	$C_{6/mmc}$ C-centered hexagonal
Lattice Parameters*	a = 2.4612 A, c = 6.708 Å
Atoms/Unit Cell	4
Cell Volume	35.189×10^{-24} cm^3
Density	2.2670 g/cm^3

*Lattice parameters a and c for graphite are shown in Figure 2.5.

Table 2.2

Characteristics of diamond crystals

Space Group	F_{d3m} face-centered cubic
Lattice Parameters*	a = 3.5670 Å
Atoms/Unit Cell	8
Cell Volume	45.385×10^{-24} cm^3
Density	3.5155 g/cm^3

*Lattice parameter for a diamond crystal is shown in Figure 2.6.

Table 2.3

Characteristics of buckminsterfullerene

Space Group	F_{m3m} body-centered cubic
Lattice Parameters*	a = 14.2 Å
Atoms/Unit Cell	240 (4 molecules)
Cell Volume	2.827×10^{-21} cm^3
Density	1.693 g/cm^3

*Lattice parameter, a, has been shown in Figure 2.7

Table 2.4

Diameters for several specific carbon nanotubes*

Chirality	Diameter (nm)	Chirality	Diameter (nm)	Chirality	Diameter (nm)
(5,5)	0.678	(10,10)	1.36	$(10,10)_2$	2.03
$(5,5)_2$	1.36	(9,11)	1.36	$(10,10)_{10}$	7.46
$(5,5)_5$	3.39	(17,3)	1.49	$(30,30)_{30}$	23.7
$(5,5)_{10}$	5.78	(0,20)	1.63	$(100,0)_{100}$	75.0
$(5,5)_{30}$	20.3	(20,20)	2.71	$(100,100)_{100}$	80.7

*Numbers under right hand of parenthesis show layers of MWCN

Table 2.5

Young's modulus for several specific carbon nanotubes*

Chirality	Modulus (GPa)	Chirality	Modulus (GPa)	Chirality	Modulus (GPa)
(5,5)	916	(10,10)	660	$(10,10)_2$	842
$(5,5)_2$	990	(9,11)	660	$(10,10)_{10}$	1014
$(5,5)_5$	1023	(17,3)	922	$(30,30)_{30}$	1007
$(5,5)_{10}$	1029	(0,20)	588	$(100,0)_{100}$	1022
$(5,5)_{30}$	1032	(20,20)	408	$(100,100)_{100}$	1005

*Numbers under right hand of parenthesis show layers of MWCN

Table 2.6

Typical production rate and cost of carbon nanotube production [90]

Company	Method	Production (g/Day)	Price ($/gram)	Type
Hyperon	CVD	5000	30-60	MWNT
Nanoamor	CVD	30000-50000	3-225	SWNT, MWNT
NanoLedge	Arc Discharge	120	64-85	SWNT
Nanocarblab	Arc Discharge	3	--	SWNT

Table 2.7

Reduced modulus (E_r) and shear modulus (G) for different rope diameters [75].

D (nm) ±0.5 nm	L (nm) ±10%	$\Delta\delta/\Delta F$ (m/N)	E_r (GPa) ±50%	G (GPa) ±50%
3.0	100	1.0	1310	···
3.0	140	4.0	899	···
4.5	285	9.3	642	···
4.5	180	3.0	503	6.5
6.0	200	1.8	369	2.9
6.0	230	3.0	332	1.7
9.0	180	0.5	189	2.3
13.5	360	0.5	298	2.8
13.5	360	1.0	149	0.9
20.0	370	0.5	67	0.7

Table 2.8

Relation between elastic constants [24]

Constants	**General Case**	**Case c_{11},c_{12},c_{13}<<c_{33}**
E_3	$c_{33}-\frac{2c_{13}^2}{c_{11}+c_{12}}$	c_{33}
ν_{13}=ν_{23}	$\frac{c_{13}}{c_{11}+c_{12}}$	$\frac{c_{13}}{c_{11}+c_{12}}$
E_1=E_2	$(c_{11}-c_{12})\cdot\frac{(c_{11}+c_{12})c_{33}-2c_{13}^2}{c_{11}c_{33}-c_{13}^2}$	$\frac{(c_{11}+c_{12})(c_{11}-c_{12})}{c_{11}}$
ν_{12}	$\frac{(c_{12}c_{33}-c_{13}^2)}{c_{11}c_{33}-c_{13}^2}$	$\frac{c_{12}}{c_{11}}$
K	$\frac{(c_{11}+c_{12})c_{33}-2c_{13}^2}{c_{11}+c_{12}+2c_{33}-4c_{13}}$	$\frac{c_{12}+c_{11}}{2}$

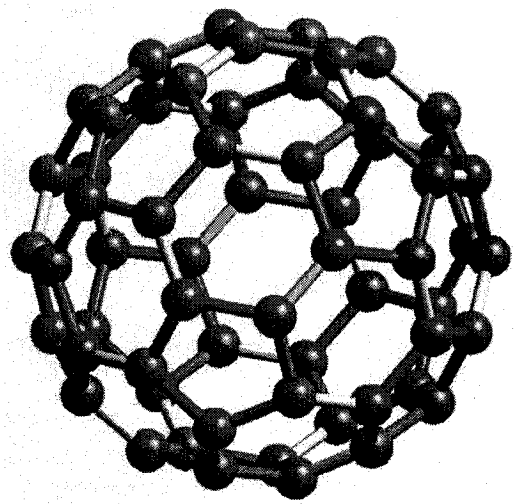

Figure 2.1 C_{60}: buckminsterfullerene structure, the "Bucky Ball" [74].

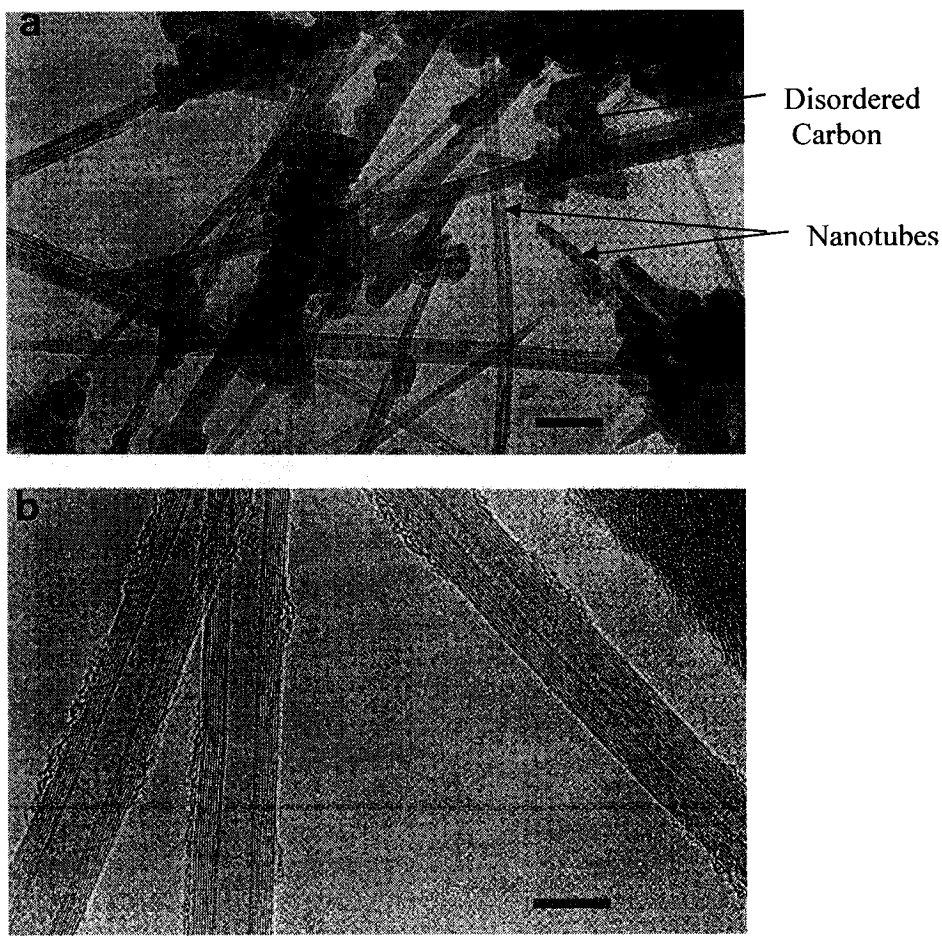

Figure 2.2 a) TEM image of soot containing carbon nanotube. Scale bar 100 nm. b) An image of individual tubes. Scale bar 10 nm. [17]

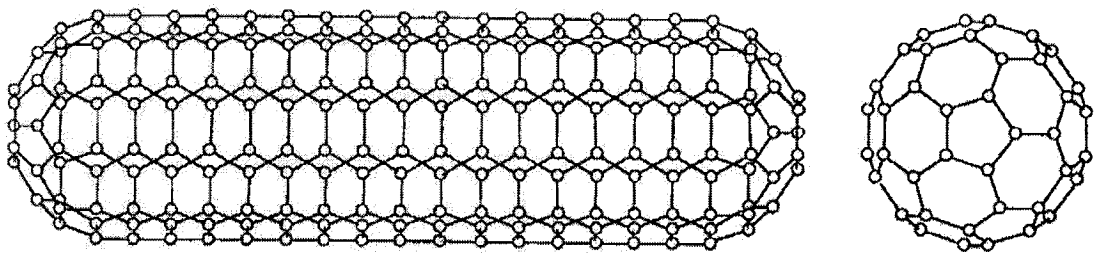

Figure 2.3 Drawing of a carbon nanotube capped by one half of a C_{60} [17].

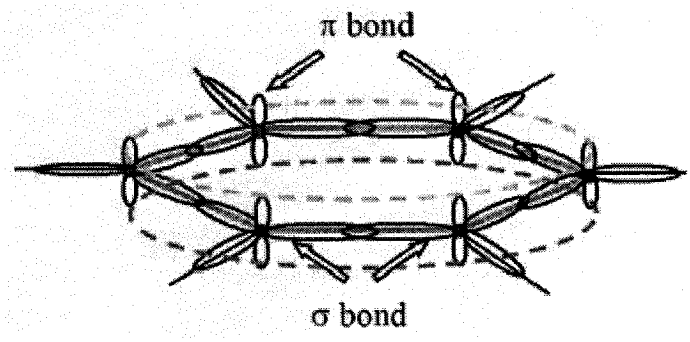

Figure 2.4 Graphite bonding [32].

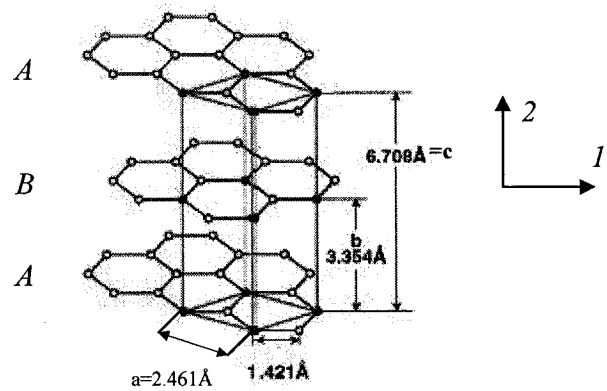

Figure 2.5 Characteristics of graphite layers. As can be seen, each *A*-layer is followed by a *B*-layer and vice versa. A unit cell for graphite structure can be seen here [74].

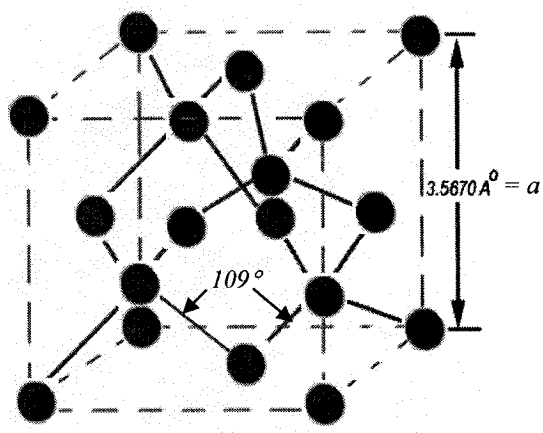

Figure 2.6 Structure of diamond unit cell (a = *3.5670 Å*) [74].

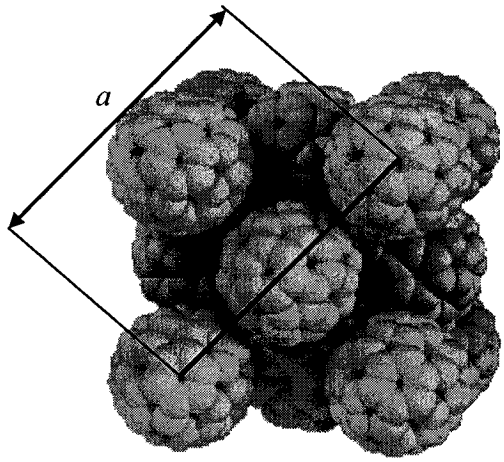

Figure 2.7 Buckminsterfullerene cluster (*a=14.2 Å*) [74].

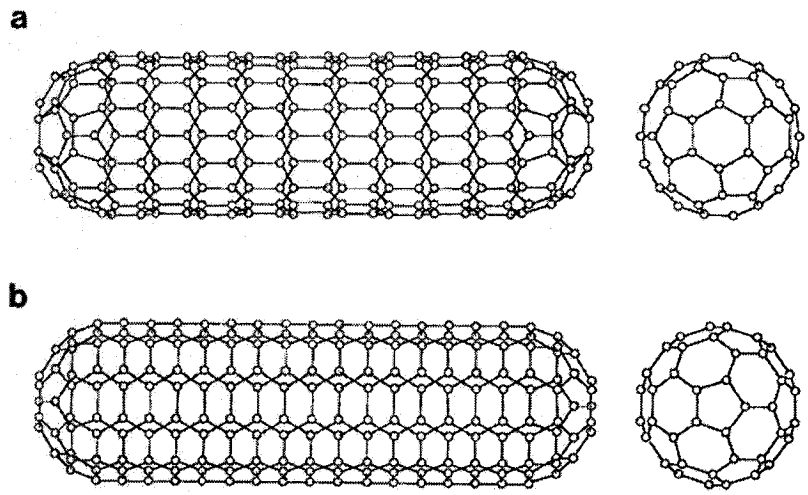

Figure 2.8 Drawing of the two types of nanotube capped by one half of a C_{60}. (a) Zigzag *(9,0)* structure (b) armchair *(5,5)* structure [17].

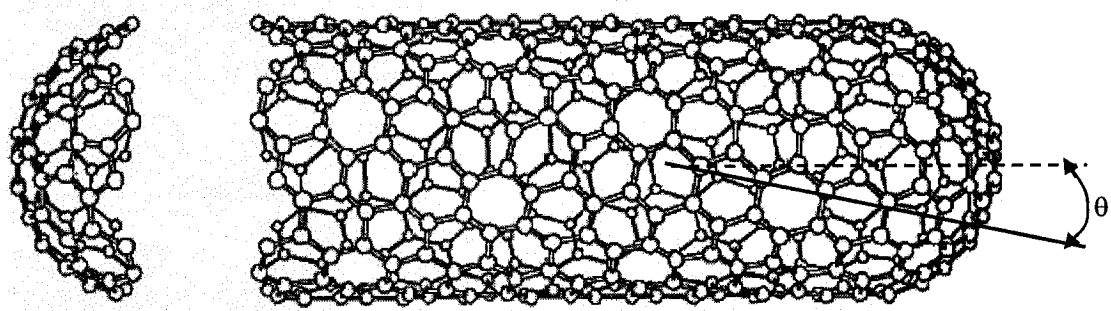

Figure 2.9 A chiral nanotube with hemispherical caps at both ends based on an icosahedral C_{140} fullerene. The corresponding chiral vector is *(10,5), diameter = 10.36 Å*, and $\theta = -19.11°$ [19].

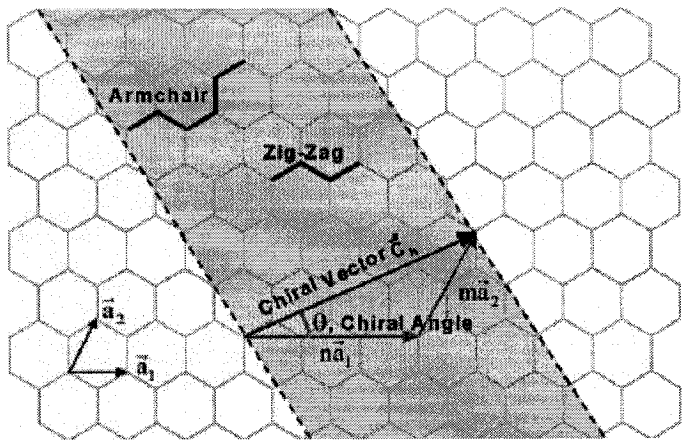

Figure 2.10 Definition of chiral vector with one pair of integers *(m,n)* [20].

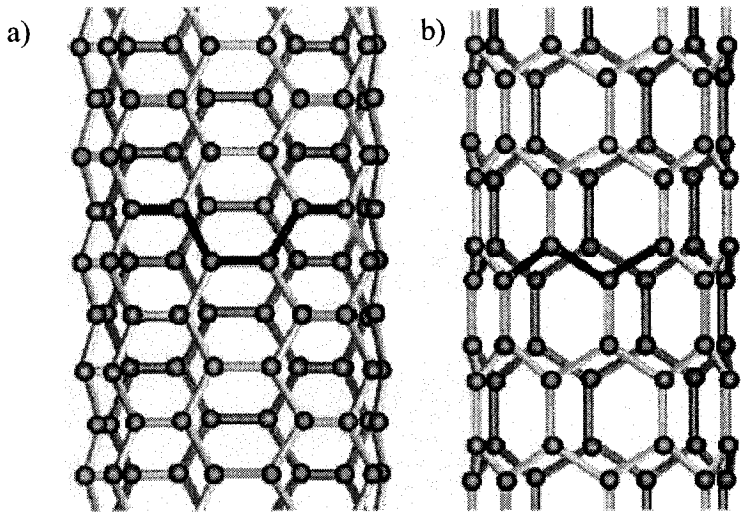

Figure 2.11 Atomic structure of (a) an armchair and (b) a ziz-zag nanotube [20].

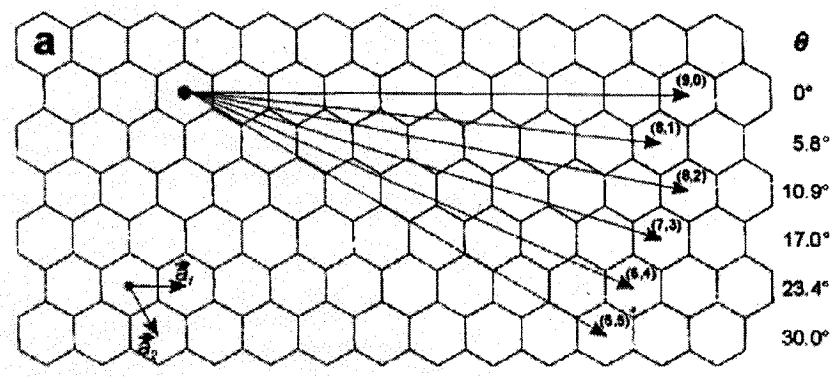

Figure 2.12 Chiral vector for different carbon nanotubes [21].

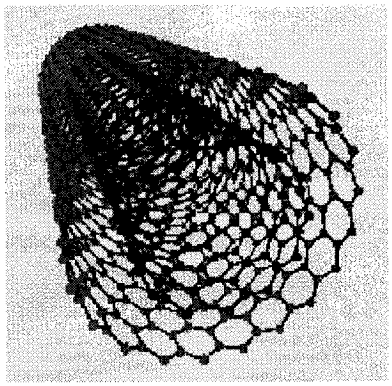

Figure 2.13 Schematic of a double walled carbon nanotube [74].

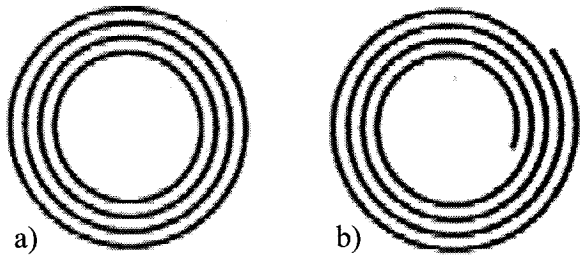

Figure 2.14 Two possible models for multi-walled carbon nanotubes: a) nested b) scroll-like [21].

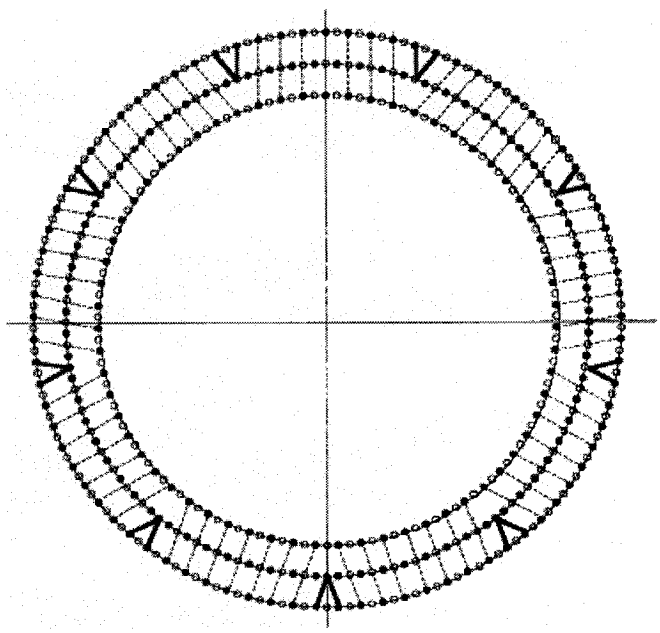

Figure 2.15 A 3-layer zigzag carbon nanotube forming a MWNT. Block dots are atoms in the plane of paper; white dots are atoms out of plane of paper [22].

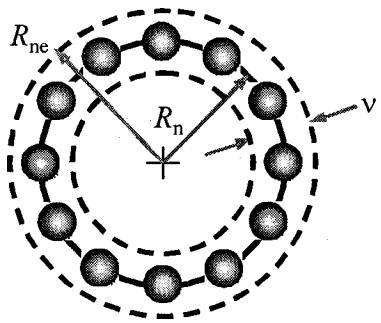

Figure 2.16 Schematic of SWNT cross-section [23]

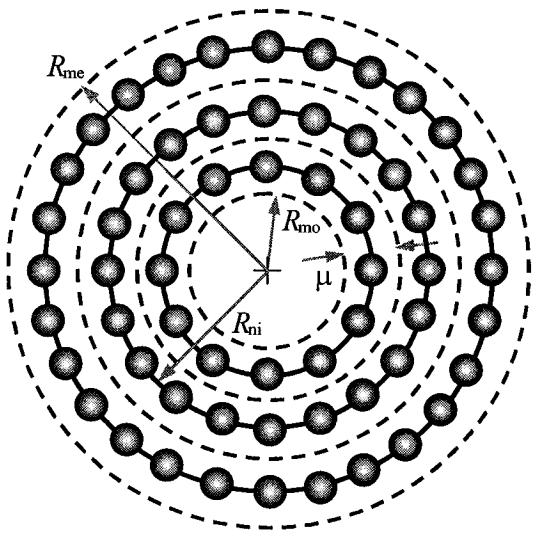

Figure 2.17 Schematic of MWNT cross-section [25]

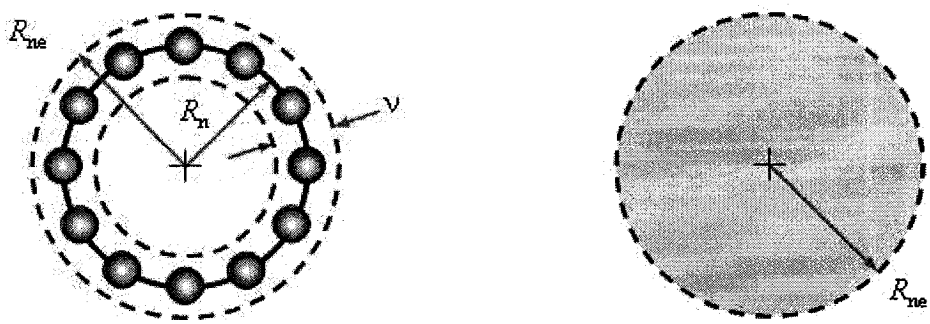

Figure 2.18 Effective area definition for a single-walled carbon nanotube [23]

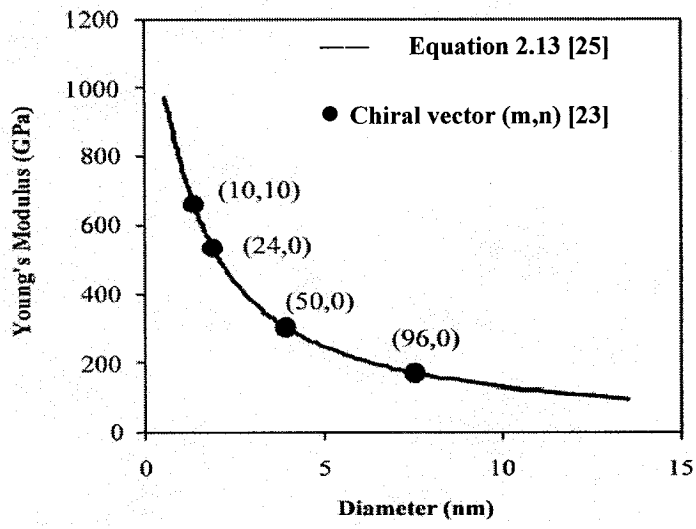

Figure 2.19 Young's modulus of SWNT as function of diameter [23].

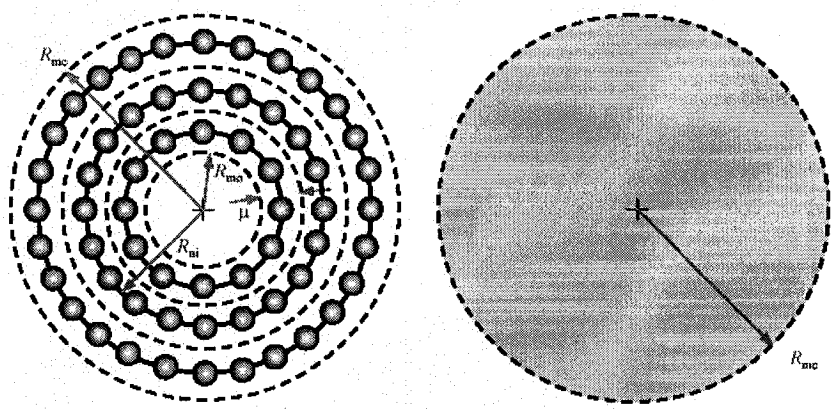

Figure 2.20 Effective area definition for a multi-walled carbon nanotube [41]

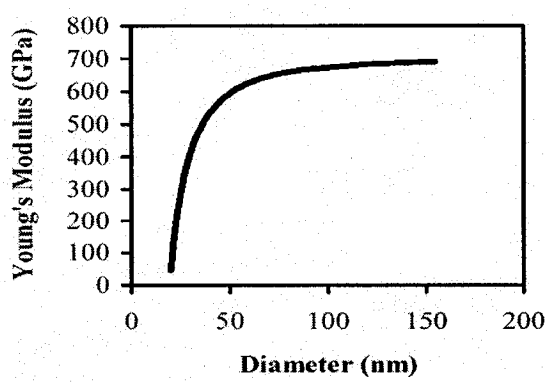

Figure 2.21 Young's modulus of MWNT as a function of diameter [41].

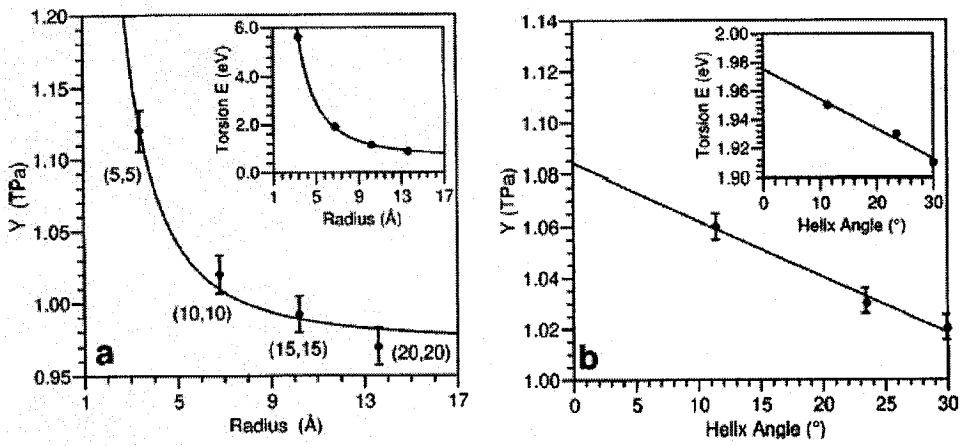

Figure 2.22 Young's modulus of single-walled carbon nanotubes as a function of both diameter and helix angle [65].

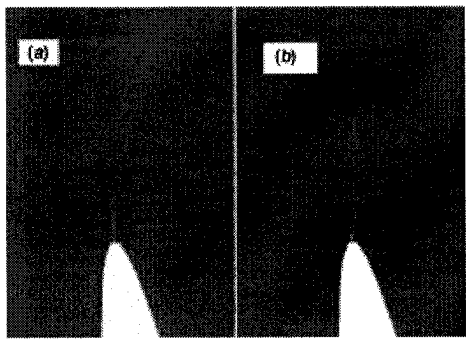

Figure 2.23 a) First resonance frequency b) Second resonance frequency of MWNT [36].

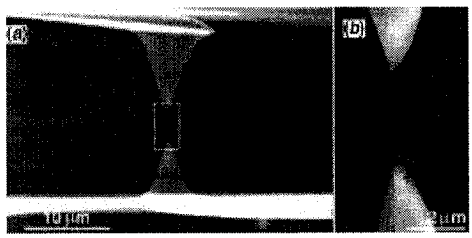

Figure 2.24 Tensile testing of individual multi-walled carbon nanotube [42]

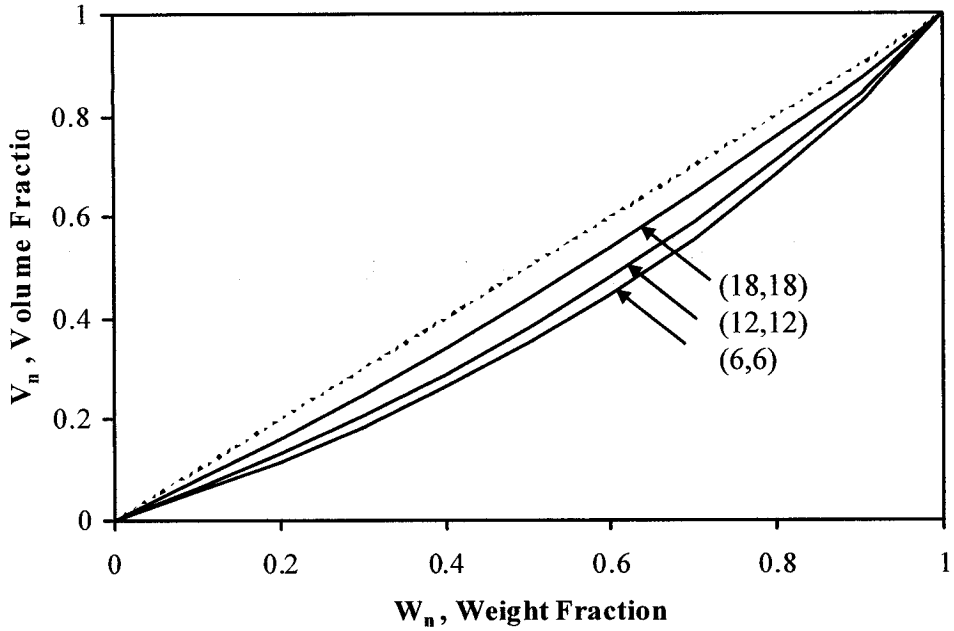

Figure 2.25 SWNT density versus diameter [23].

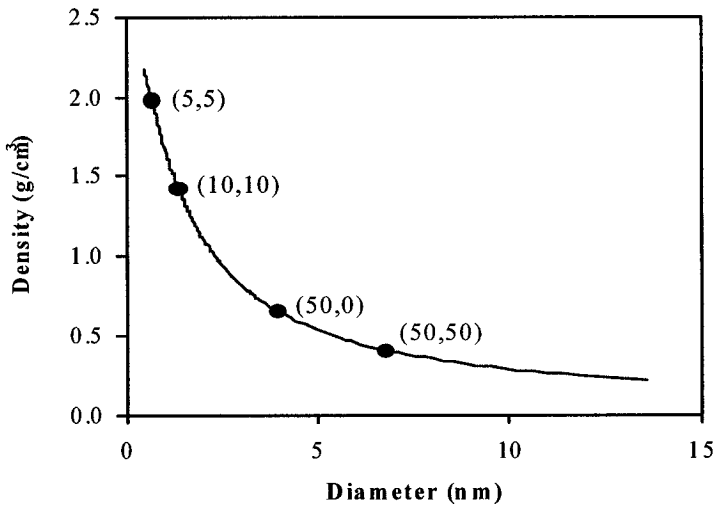

Figure 2.26 SWNT volume fraction versus weight fraction [23].

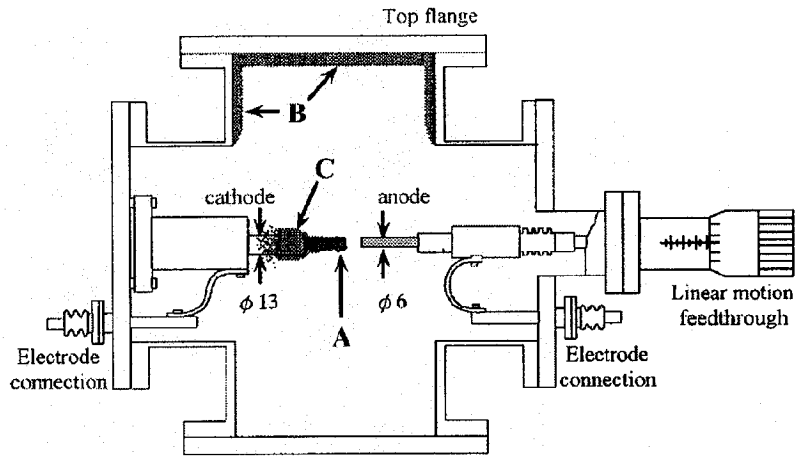

Figure 2.27 Apparatus used for arc evaporation of carbon nanotubes [50].

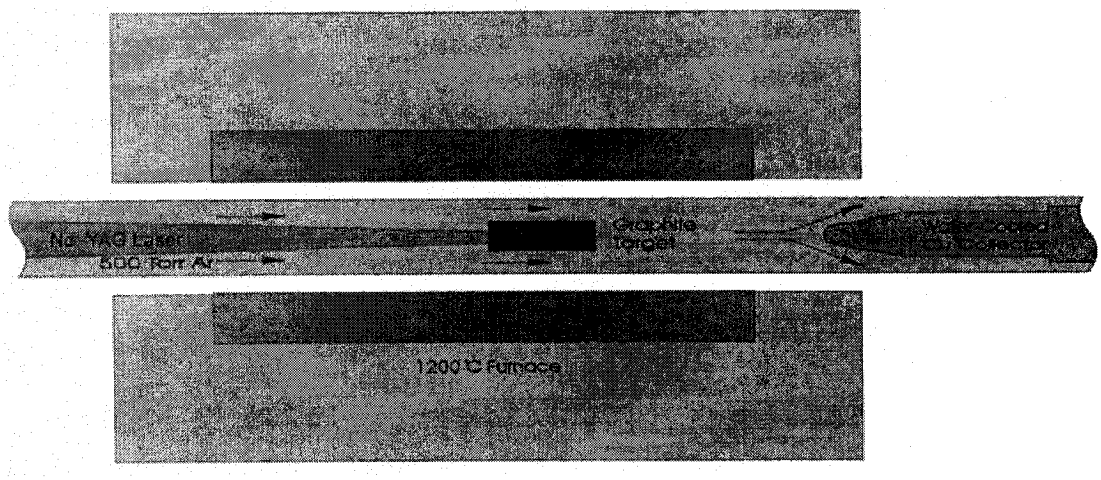

Figure 2.28 Schematic of the laser ablation method for producing carbon nanotubes [51]

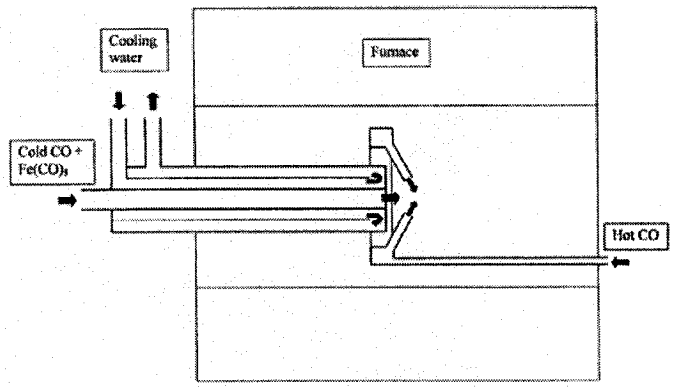

Figure 2.29 Layout of a CO flow-tube reactor, showing water-cooled injector and 'showerhead' mixer [55].

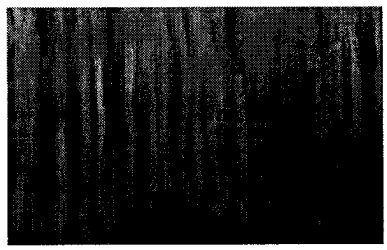

Figure 2.30 Single-standing MWNT produced by PECVD (plasma enhanced chemical vapor deposition) [60].

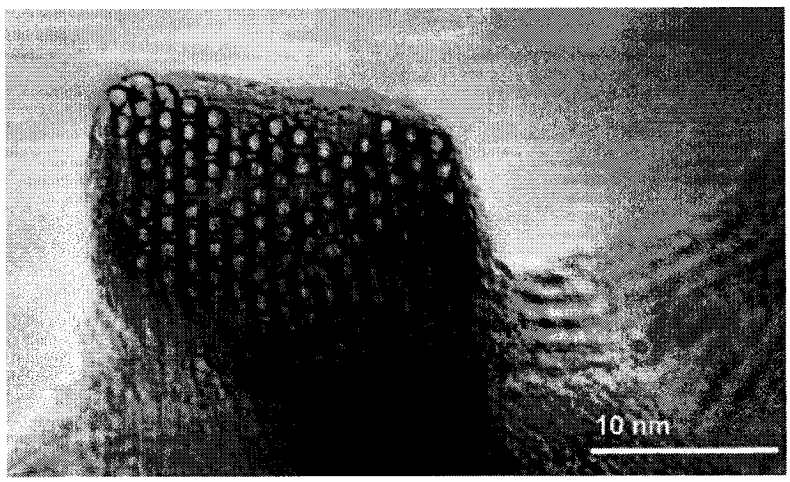

Figure 2.31 A hexagonal array of carbon nanotubes [14].

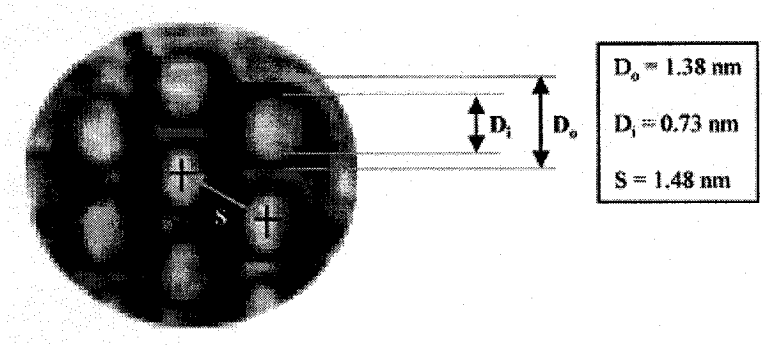

Figure 2.32 Image analysis of an array of tubes [61].

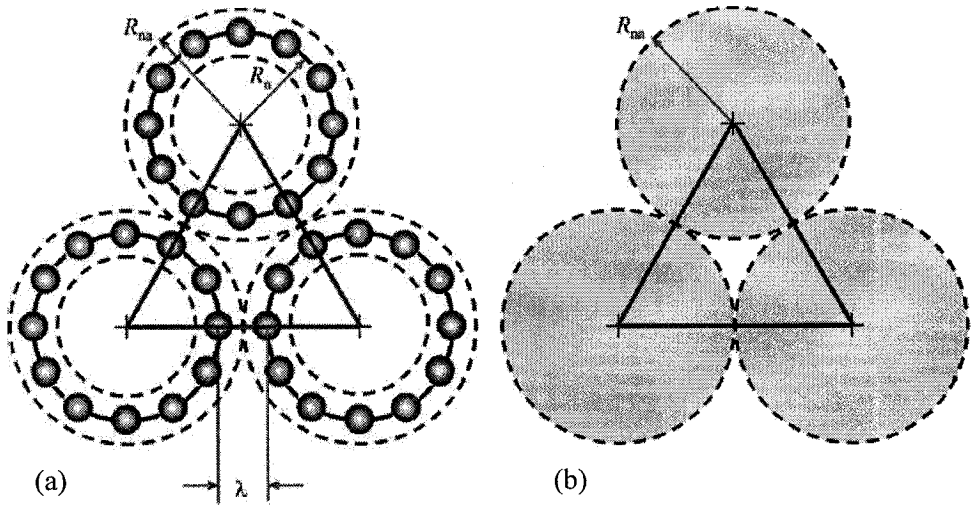

Figure 2.33 (a) Carbon nanotube array and (b) its effective reinforcement array [25].

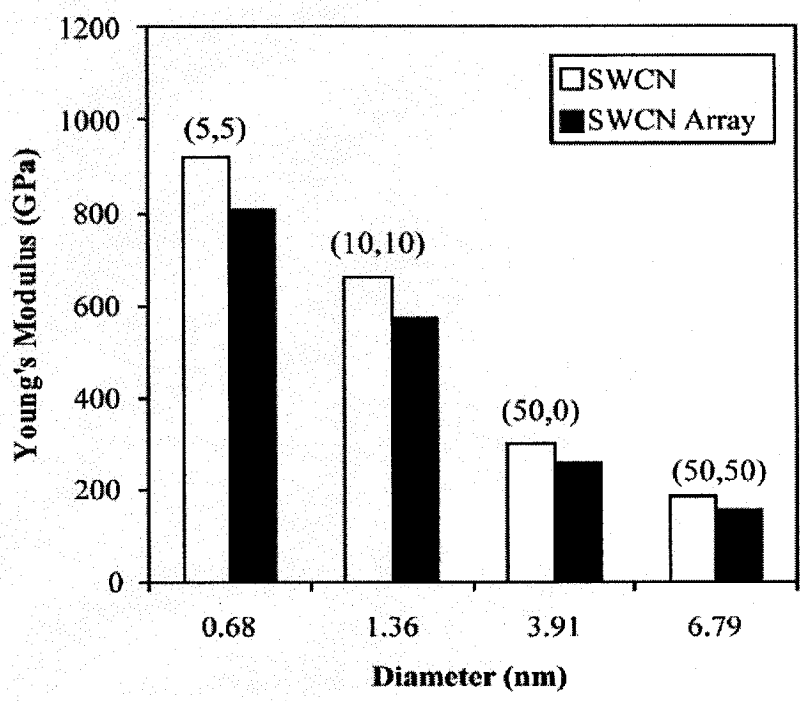

Figure 2.34 Young's modulus comparison between individual SWNT and their arrays [25].

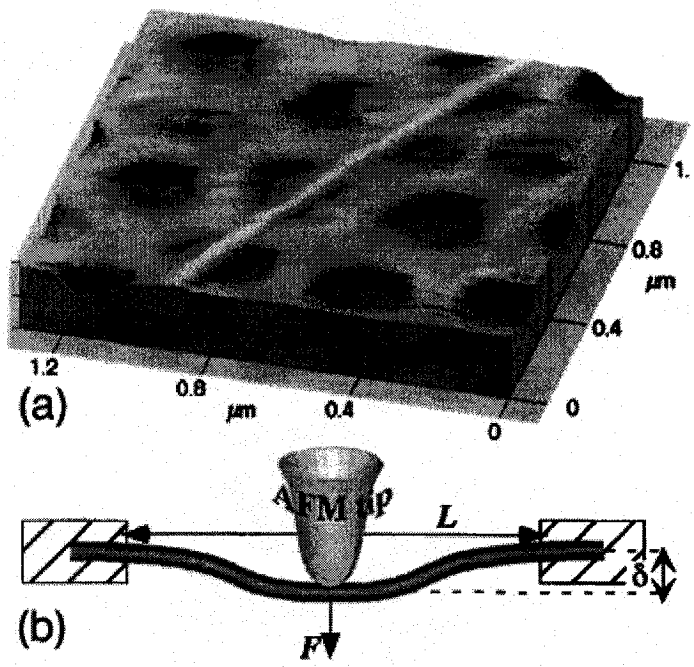

Figure 2.35 a) AFM image of a SWNT rope bridging a pore of the alumina membrane. b) Schematic of the measurement.

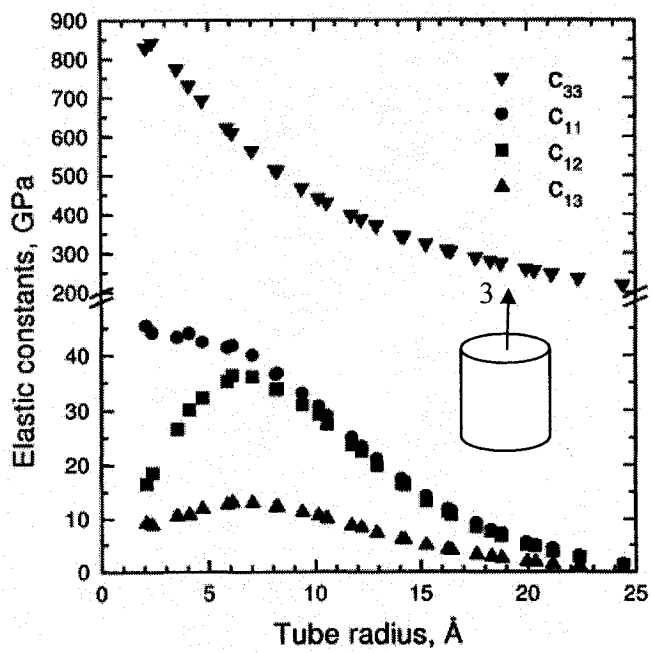

Figure 2.36 Elastic constants of single-walled carbon nanotubes array [24]. Note that coordinates *1* and *2* are perpendicular to *3* with arbitrary directions.

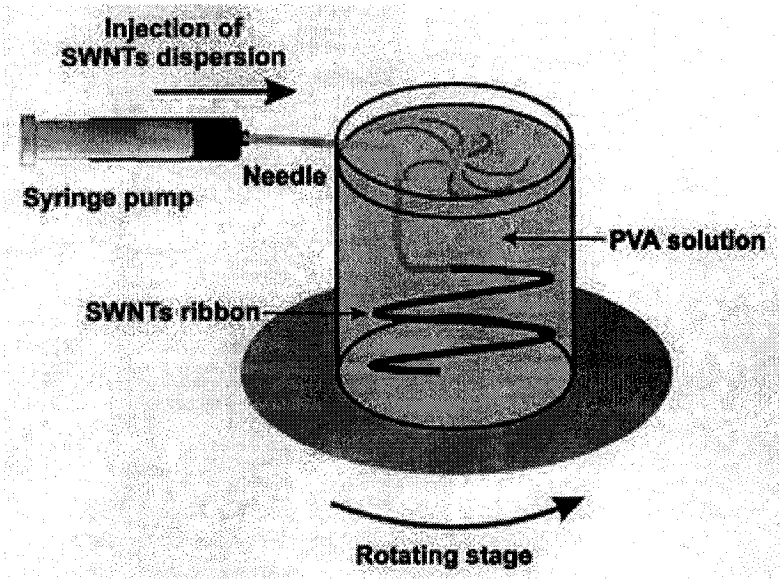

Figure 2.37 Spinning method to make high concentrated carbon nanotube fibers. [3].

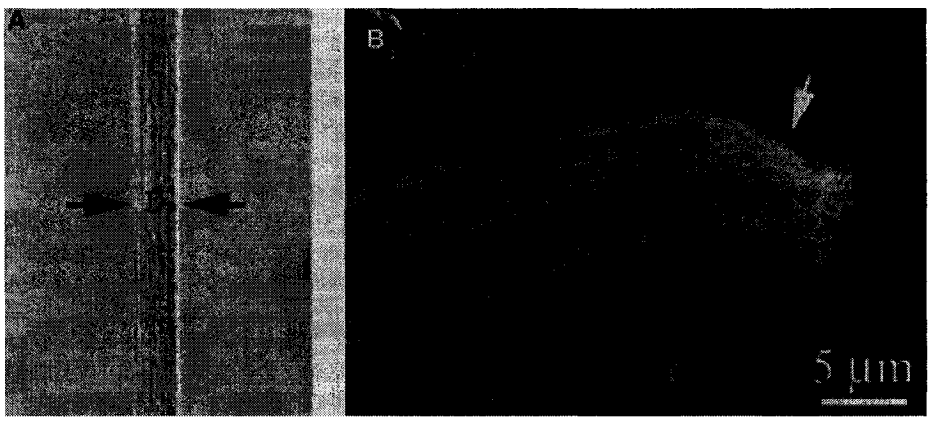

Figure 2.38 Well-aligned carbon nanotube produced by [6]. a) The distance between black arrows is 10μm. b) SEM image of broken carbon nanotube strand after a tensile test.

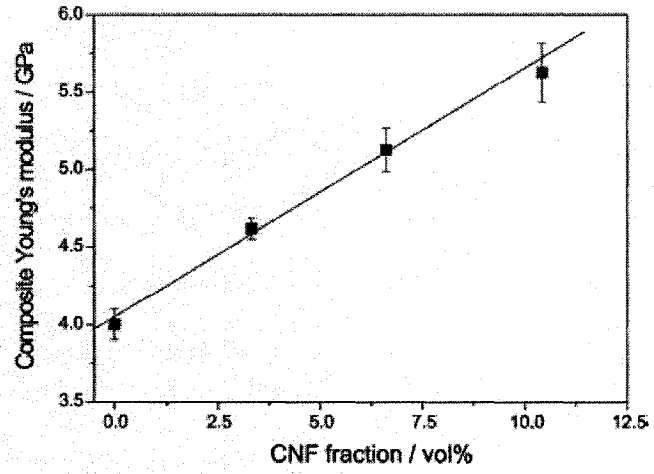

Figure 2.39 Young's modulus versus carbon nanotube fraction for a PEEK/CNT composite [9].

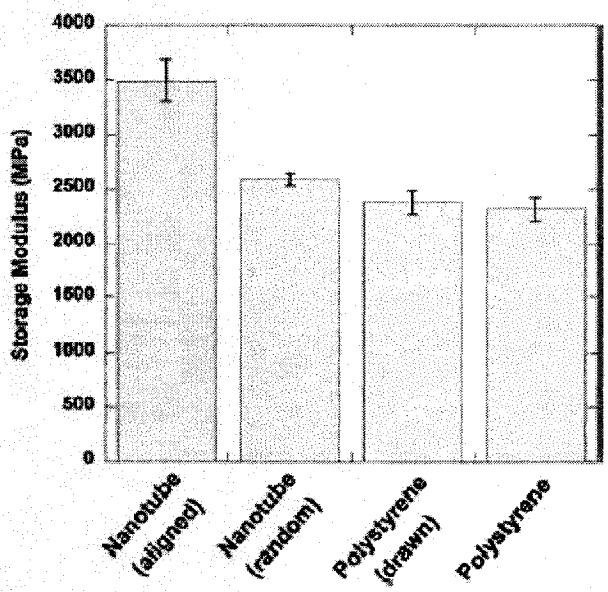

Figure 2.40 Effect of alignment on modulus of a polystyrene/CNT composite [66].

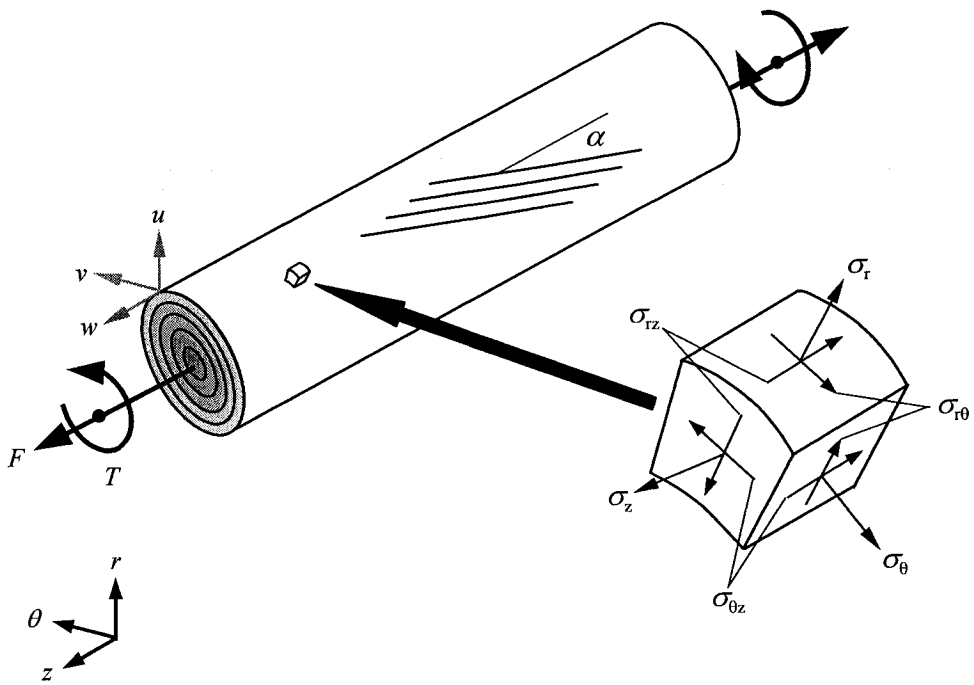

Figure 2.41 Layered cylinder and corresponding stresses in an element [61].

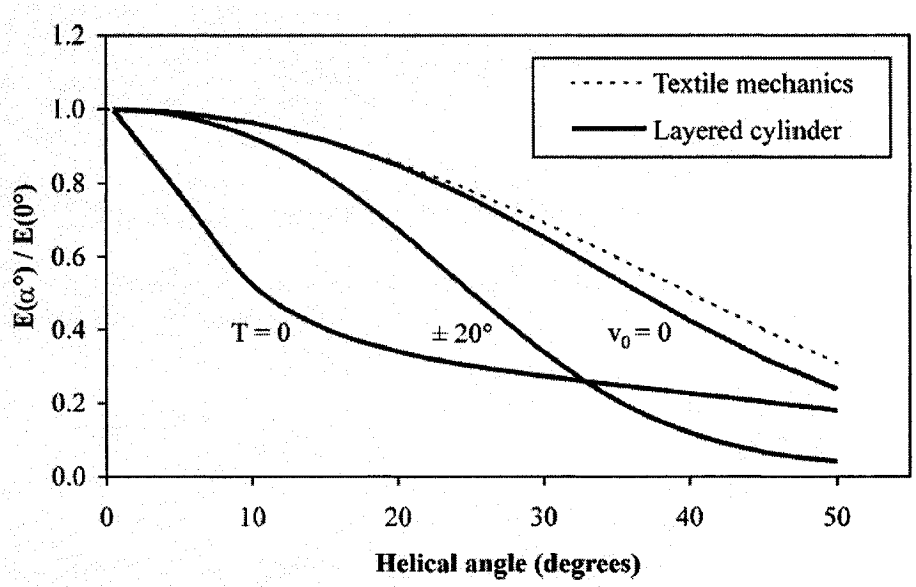

Figure 2.42 Young's modulus of the layered cylinder of polymer/CNT [61].

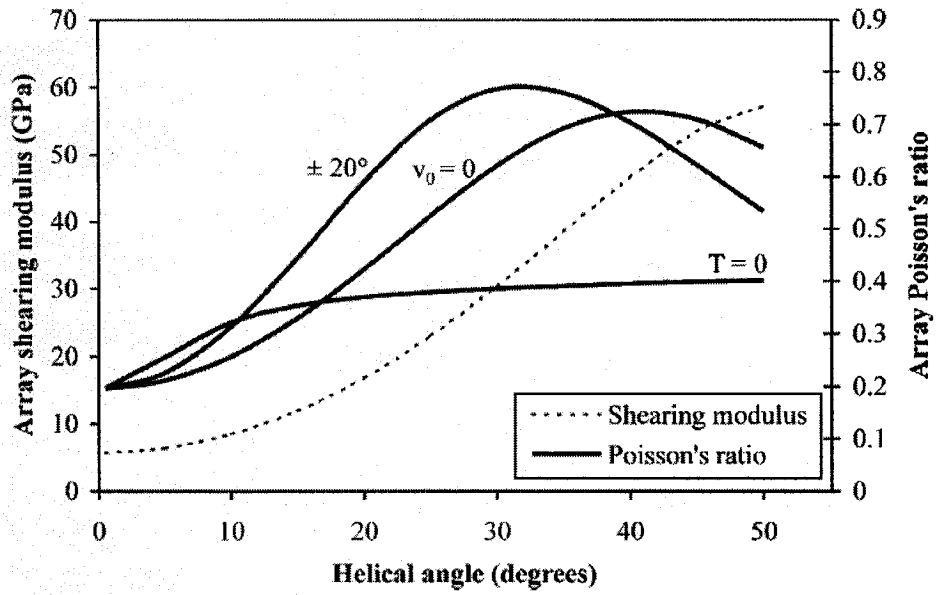

Figure 2.43 Axial shearing modulus and Poisson's ratio for layered cylinder [61].

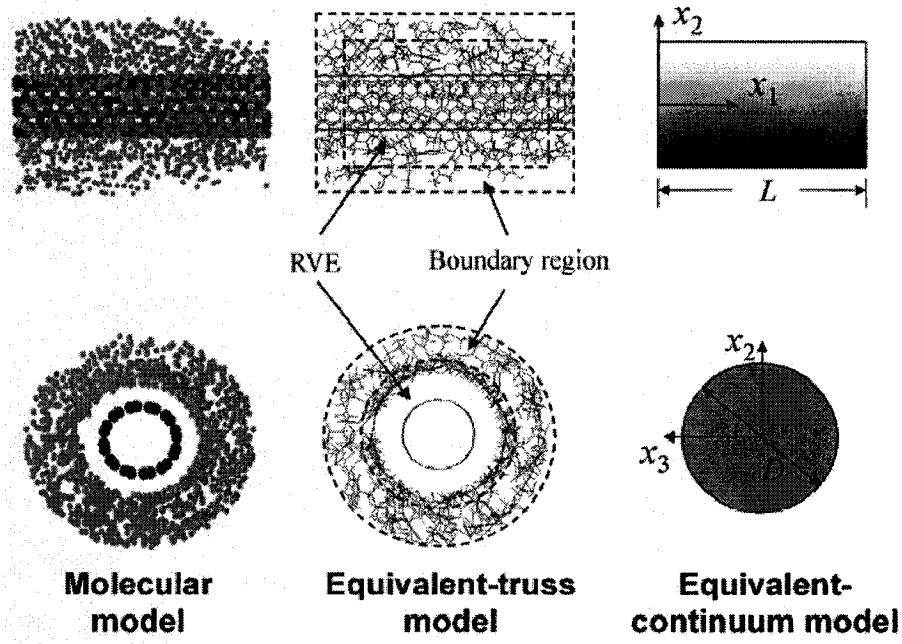

Figure 2.44 Equivalent-continuum modeling of SWNT effective fiber [69].

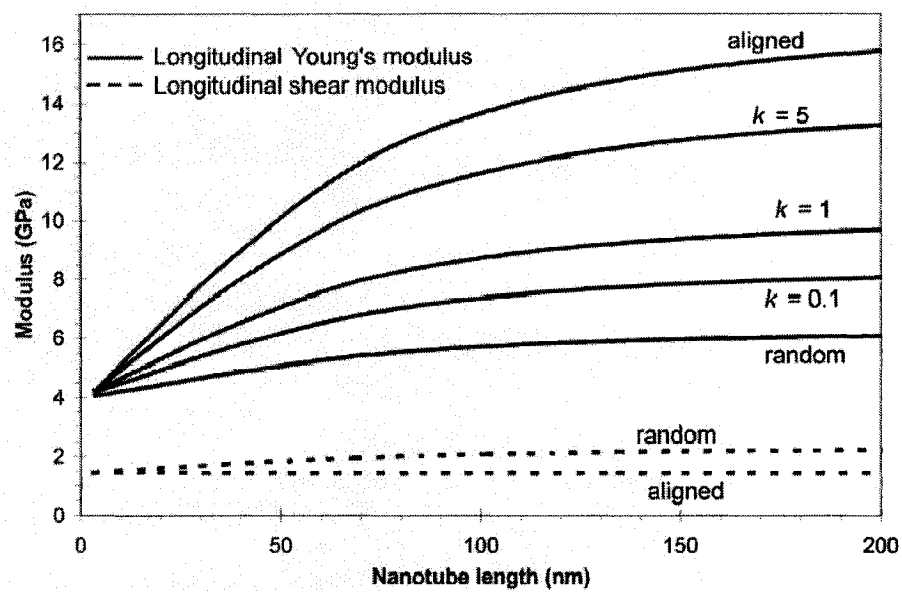

Figure 2.45 Predicted SWNT/LaRC-SI composite properties versus nanotube length and alignment [69].

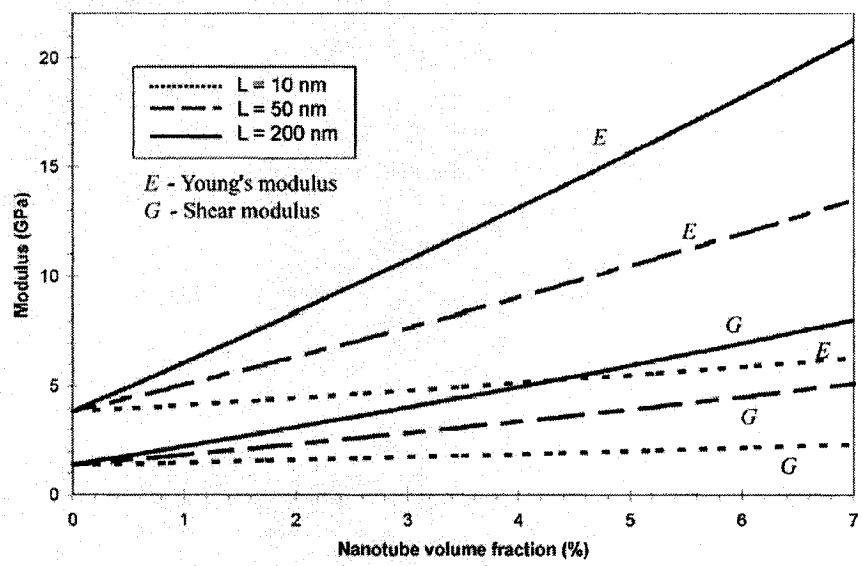

Figure 2.46 Predicted SWNT/LaRC-SI composite properties versus nanotube volume fraction [69].

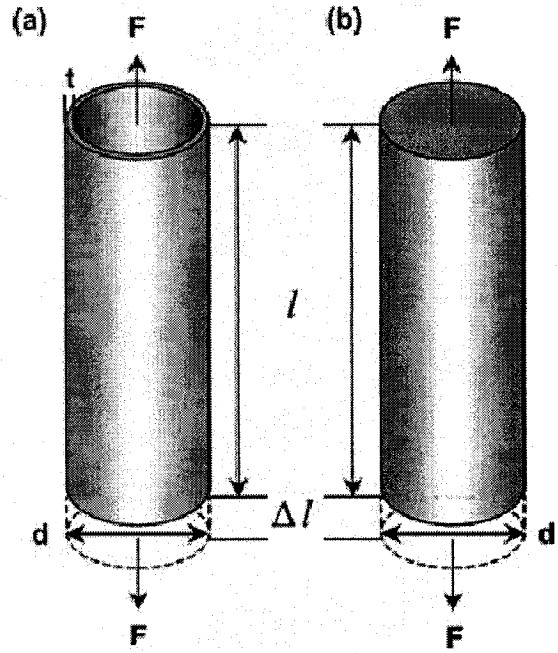

Figure 2.47 Schematic of (a) nanotube and (b) effective fiber [70].

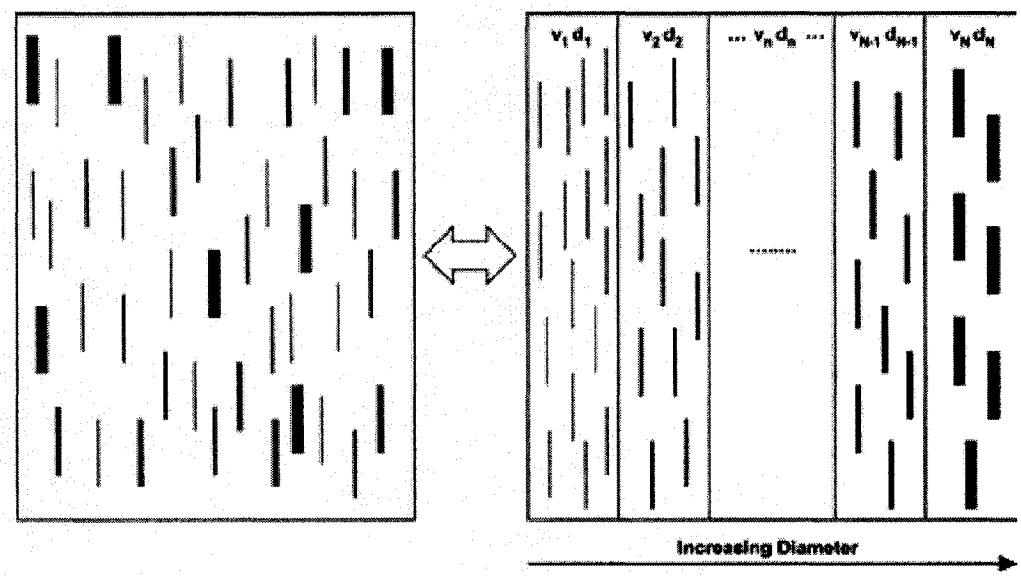

Figure 2.48 Parallel composite with specific nanotube diameter and its partial volume [70].

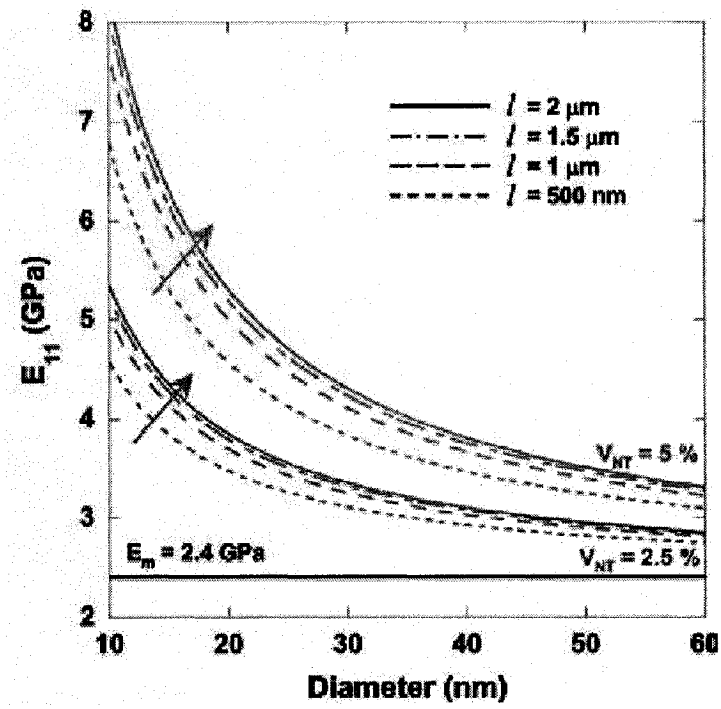

Figure 2.49 Effects of nanotube diameter, length and volume fraction on elastic modulus of nanocomposite [70].

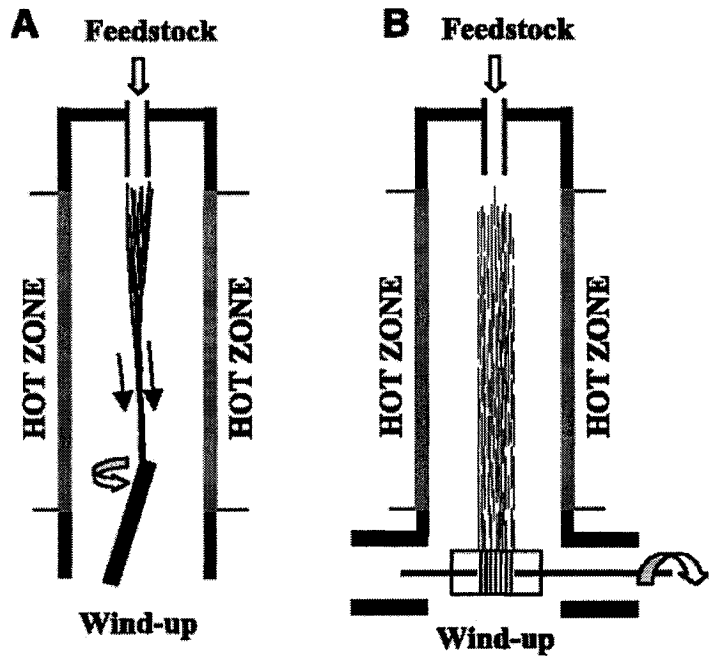

Figure 2.50 Schematic of the direct spinning process [89].

Chapter 3

Helical Carbon Nanotube Fiber Modeling

In this chapter, a finite element model of a helical carbon nanotube fiber is developed, as presented in Section 2.8.1. Then, the results of the model are compared to the anisotropic elasticity solution of Pipes and Hubert [61]. Next, a strain energy method is proposed to obtain the nanotube fiber elastic constants.

3.1 Finite element modeling

It is estimated that to achieve load transfer so that the entire cross-section of the bundle becomes effective, the SWNT contact length must be on the order of 10 to 120 μm [32]. However, typical length of carbon nanotubes is several hundred nanometers [64]. Pipes and Hubert [61] introduced the concept of helical nanotube fibers as an effective method to produce a high nanotube volume fraction fiber from discontinuous collimated nanotubes. A theoretical study done by Qian [67] showed that nanotube twisting can significantly decrease the required contact length for complete load transfer between the nanotubes. The carbon nanotube fiber model used in the work consists of layered concentric cylinders in which carbon nanotubes are oriented following a helical path (Figure 3.1). The degree of helicity of the fiber can be characterized by the number of turns per unit length, t. Moreover, the nanotubes are assumed to follow a helical path along the length of the fiber. The tangent of the helical angle is a linear function of the radial position and varies from 0 at the fiber axis to a maximum of α_{max} at the fiber outer surface:

$$\tan \alpha_{\max} = 2\pi Rt \tag{3.1}$$

where R is the fiber outer radius. It is worth mentioning that t will be considered constant for all layers of the fiber. Figure 3.2 shows the variation of the helical angle with the fiber radius of a fiber with a radius and length of *500 nm* and *500,000 nm*, respectively. For small angles of the twist ($\alpha < 10°$) we have $\tan \alpha \approx \alpha$; therefore, the helicity varies linearly respect to the position.

In this work, the nanotube fiber is modeled by using the finite element method. Since the twist angle is variable through the fiber thickness (zero at the center, maximum at the surface), the fiber cross section is divided into m layers as shown in Figure 3.3. Each layer has a constant twist angle as shown in Figure 3.3 (which shows 6 layers). The angle of twist for each layer is determined by using:

$$\theta_i = \tan^{-1}(2\pi \cdot t \cdot l(i-1)) \tag{3.2}$$

where l is layer thickness ($l=R/m$), and i is layer number ($i = 1$ for central circle and $i = m$ for outermost layer). The finite element software, ANSYS 7.1 [72], was used for the analyses and the solid 20-node element was selected to mesh the model (Figure 3.4). This element defined by 20 nodes has three degrees of freedom per node: translations in the nodal x, y, and z directions. The element can be chosen to have any spatial orientation. In this work, a carbon nanotube fiber with an outer diameter of 8.97 nm and a length of 100 nm was modeled. Figure 3.5 shows a cross section of the mesh, while Figure 3.6 shows an isometric view of the mesh. As can be seen from Figure 3.5 each ring contains 32 elements while the central circle has 48 elements. Therefore, 208 elements are used to mesh the fiber cross section. The length of the model is divided in 33 sections in order to have elements with appropriate shape factors. Therefore, 6864 elements are utilized to mesh the fiber section.

Properties of the carbon nanotubes are obtained from Pipes and Hubert [61] (Table 3.1). By doing this, it becomes possible to compare results from the finite element analysis with the anisotropic elasticity solution used in [61]. In this table, axis *1* is along the carbon nanotube length while axes *2* and *3* are perpendicular to *1*. Figure 3.7 shows the reference coordinate system of our model. Since the carbon nanotube crystals are orthotropic with transverse isotropy, properties along axes 2 and 3 are equal, i.e. $E_2=E_3$, $G_2=G_3$ and $\nu_{12}=\nu_{13}$. Properties of the carbon nanotubes (Table 3.1) are used in a proper element coordinate system as shown in Figure 3.4 (*1* direction along x, while *2* and 3 along y and z respectively). In order to model the helicity of the fiber for each layer, the element coordinate system is rotated based on the layer twist angle.

The properties of the fiber are constant along the fiber length. Therefore, in order to maximize both speed of the finite element calculation and accuracy of the result, a preliminary analysis is performed to measure the proper aspect ratio (ratio of the length to diameter) to be used. Fibers with different length are subjected to an extensional strain. Figure 3.8 shows the axial Young's modulus (E_{11}) of fibers as a function of aspect ratio for a twist angle of 20°. For a very short fiber (small aspect ratio), Poisson's effect causes a significant error in the modulus while a very long fiber needs longer processing time without any significant gain in accuracy of the results. As can be seen from Figure 3.8, an aspect ratio of 10 is accurate enough since by further increasing the length, no significant change in modulus is observed. Based on the radius and length mentioned before (8.97 nm and 100 nm respectively), a model aspect ratio (l/R) of about 11 seems appropriate.

3.2 Comparison between elasticity and FEA

As can be seen in Figure 2.42 of Section 2.8.1, two different cases were examined. For the first case (Case 1), a uniform extensional strain (ω_0) equal to 0.01 was applied to one end of the model in the *1* direction (or *Z* in cylindrical coordinate system) while points on the other end were fixed along *Z*. This case is analogous to a simple uniaxial tensile test where the fiber is free to rotate, so the torque (T) is zero. For the second case (Case 2), all points in the model are fixed against any rotation ($v_0=0$ based on Figure 2.41) while the other boundary conditions are similar to Case 1 and $T\neq 0$. In summary, the boundary conditions applied to the model are:

Case 1 ($T=0$): $u_z = 0$ @ Z=0, $u_z = \omega_0 \times 100$ @ Z=100 nm (3.3-a)

Case 2 ($v_0=0$): $u_z = 0$ @ Z=0, $u_z = \omega_0 \times 100$ @ Z=100 nm, $u_\vartheta = 0$ @ *all points* (3.3-b)

The resultant reaction force, F is calculated from the finite element nodal forces. The relaxation method explained in Section 2.8.1 is used, and the fiber Young's modulus is computed as follows:

$$E_{11} = \frac{F}{\pi \cdot R^2 \omega_0} \tag{3.4}$$

Figures 3.9 and 3.11 show the results from the finite element analysis compared to results from the elasticity solution [61]. Good agreement was obtained between the finite element analysis and elasticity solution. As can be seen in Figure 3.9, a maximum error of less than 8 percent can be seen for a twist angle of 40°. Moreover, we observe a major reduction of the Young's modulus by increasing the twist angle from 0° (514 GPa) to 20° (167 GPa), while further increase in twist angle results in a moderate reduction to 82 GPa for a twist angle of 50°. The effect of helicity can be seen in Figure 3.10 where the extensional strain applied to the fiber produces a rotation in the fiber, because twisted fibers tend to become more straight as a result of extensional strain. Figure 3.11 shows the variation of the fiber Young's modulus for Case 2. Here, the Young's modulus reduction is not as significant compared to Case 1. Table 3.2 shows the values of the torque at the middle of the fiber as a result of preventing the fiber from rotation ($u_\theta=0$). The maximum torque is observed for a twist angle of 25°. The error percentages between elasticity and finite element for the torque and Young's modulus are also presented in Table 3.2.

The axial Poisson's ratio for both cases is obtained from the following equation:

$$\nu_{z\vartheta} = -\frac{u_{r=R}}{Rw_0} \tag{3.5}$$

where $u_{r=R}$ is the radial nodal displacement at $r=R$. In order to determine $u_{r=R}$, we calculate the average nodal displacement at the outermost layer of the model ($R=8.97$ *nm*). Figure 3.12 shows the cross section of the fiber with a twist angle of 20° for the case 1. As expected, the longitudinal extension of the fiber causes a radial contraction. Figure 3.13 shows the variation of $u_{r=R}$ on the fiber surface where the average radial nodal displacement of -3.43×10^{-3} *nm* was calculated. With an extensional strain of *0.01* and using Equation 3.5, an axial Poisson's ratio of *0.37* was calculated (Note that $\upsilon_{12}=\upsilon_{z\theta}$). This value is very close to the value of *0.38* calculated by elasticity [61]. The same method is used for different angles for both cases (Figure 3.14). As can be seen in this

figure, for Case 2, elasticity and FEA are in good agreement while for Case 1, a maximum error of *14 %* occurs for large angles of twist (*>20°*), but for lower twist angles (*<20°*) this error is less than *2 %*.

In another investigation, the stress distribution for both elasticity and finite element methods are examined. Figure 3.15 shows the stress distribution for the component σ_R through the thickness of the fiber. This component has an important effect on the friction between carbon nanotubes. The negative stress proves that all the tubes are in compression which is required to transfer load between them. The result from elasticity solution is a little different from the finite element solution. While the finite element fiber is a solid cylinder producing the maximum stress at the center of the fiber, the anisotropic elasticity solution was done for a hollow cylinder which results $\sigma_r=0$ at the center of the fiber. Moreover, in anisotropic elasticity in spite of finite element analysis, the radial stress at the outermost layer is positive (Figure 3.15). This could be explained by an approximation in anisotropic elasticity where it is supposed that $\sigma_{r\theta} = 0$. This assumption especially for the outermost layer can generate significant error because the maximum $\sigma_{r\theta}$ occurs there.

3.3 Elastic constant calculation

Energy methods have been used to calculate composite material elastic constants since the 1960's. Hashin and Rosen [73] used this method to calculate elastic moduli of fiber-reinforced composites. The same method was used by Odegard *et al.* [69] to estimate the values of elastic constants of carbon nanotube reinforced composites (Section 2.8.2). In this method, displacement boundary conditions are applied to the model:

$$u_i^0(S) = \varepsilon_{ij}^0 x_j \tag{3.6}$$

where S is the bounding surface, x_j is the surface coordinate, u_i^0 is the displacement and ε_{ij}^0 is the strain tensor, while i and j are indicial notations. Then, a representative volume element (RVE) of the model is defined where strain and stress are averaged over the element. The effective Hooke's law for an anisotropic is defined as:

$$\sigma_{ij}^{0} = C_{ijkl}\varepsilon_{kl}^{0} \tag{3.7}$$

where σ_{ij}^{0} and ε_{kl}^{0} are averaged stress and strain respectively and C_{ijkl} is the effective elastic modulus. By applying an averaged strain and computing the resultant averaged stress, it is possible to determine C_{ijkl} from Equation 3.7. In order to find the averages, a field solution has to be found first. This is, in general, a very complex task. On the other hand, energy methods are more appropriate to obtain elastic constants. Strain energy (W) is defined by:

$$W = \frac{1}{2}V\sigma_{ij}^{0}\varepsilon_{kl}^{0} \tag{3.8}$$

where V is the volume occupied by the model. Replacing σ_{ij}^{0} with Equation 3.7, we obtain:

$$W = \frac{1}{2}VC_{ijkl}\varepsilon_{ij}^{0}\varepsilon_{kl}^{0} \tag{3.9}$$

For the nanotube fiber studied in this work, we assume transverse isotropy. By considering the contraction notation of $ij \rightarrow m$ and $kl \rightarrow n$, Hooke's law becomes:

$$\begin{pmatrix} \sigma_{11}^{0} \\ \sigma_{22}^{0} \\ \sigma_{33}^{0} \\ \sigma_{12}^{0} \\ \sigma_{13}^{0} \\ \sigma_{23}^{0} \end{pmatrix} = \begin{bmatrix} C_{11} & C_{12} & C_{12} & 0 & 0 & 0 \\ C_{12} & C_{22} & C_{23} & 0 & 0 & 0 \\ C_{12} & C_{23} & C_{22} & 0 & 0 & 0 \\ 0 & 0 & 0 & 2C_{44} & 0 & 0 \\ 0 & 0 & 0 & 0 & 2C_{44} & 0 \\ 0 & 0 & 0 & 0 & 0 & C_{22} - C_{23} \end{bmatrix} \begin{pmatrix} \varepsilon_{11}^{0} \\ \varepsilon_{22}^{0} \\ \varepsilon_{33}^{0} \\ \varepsilon_{12}^{0} \\ \varepsilon_{13}^{0} \\ \varepsilon_{23}^{0} \end{pmatrix} \tag{3.10}$$

or:

$$\sigma_{11}^{0} = C_{11}\varepsilon_{11}^{0} + C_{12}\varepsilon_{22}^{0} + C_{12}\varepsilon_{33}^{0} \tag{3.10-a}$$

$$\sigma_{22}^{0} = C_{12}\varepsilon_{11}^{0} + C_{22}\varepsilon_{22}^{0} + C_{23}\varepsilon_{33}^{0} \tag{3.10-b}$$

$$\sigma_{33}^0 = C_{12}\varepsilon_{11}^0 + C_{23}\varepsilon_{22}^0 + C_{22}\varepsilon_{33}^0 \tag{3.10-c}$$

$$\sigma_{12}^0 = 2C_{44}\varepsilon_{12}^0 \tag{3.10-d}$$

$$\sigma_{13}^0 = 2C_{44}\varepsilon_{12}^0 \tag{3.10-e}$$

$$\sigma_{23}^0 = (C_{22} - C_{23})\varepsilon_{23}^0 \tag{3.10-f}$$

For this class of material, five independent constants (C_{11}, C_{12}, C_{22}, C_{23}, and C_{44}) are necessary to describe the fiber elastic behavior. By selecting five proper independent moduli that are a combination of these constants and by specifying proper boundary conditions to the model, one of these constants appears in the strain-energy function. Therefore, the five constants can be determined from the strain energies for five different sets of boundary conditions.

The five moduli chosen are C_{11}, G_{23}, K_{23}, G_1, E_1, defined by [73]:

$$G_{23} = \frac{1}{2}(C_{22} + C_{23}) \tag{3.11}$$

$$K_{23} = \frac{1}{2}(C_{22} - C_{23}) \tag{3.12}$$

$$G_{12} = G_{13} = G_1 = C_{44} \tag{3.13}$$

$$E_1 = C_{11} - \frac{2C_{22}^2}{C_{22} + C_{33}} \tag{3.14}$$

In these equations K_{23} and G_{23} are the in-plane (x_2x_3 plane) bulk and shearing modulus, respectively, G_1 is axial shear modulus, and E_1 is the longitudinal Young's modulus. From these constants, the other elastic constants can be determined by:

$$\nu_{12} = \nu_{13} = \nu_1 = \frac{1}{2}\left(\frac{C_{11} - E_1}{K_{23}}\right)^{1/2} \tag{3.15}$$

$$E_2 = E_3 = \frac{4G_{23}K_{23}}{K_{23} + \psi G_{23}} \tag{3.16}$$

$$\nu_{23} = \frac{K_{23} - \psi G_{23}}{K_{23} + \psi G_{23}} \tag{3.17}$$

where:

$$\psi = 1 + \frac{4K_{23}\nu_1^2}{E_1} \tag{3.18}$$

where v_1 is the axial Poisson's ratio, v_{23} is then transverse Poisson' ratio, and E_2=E_3 are the transverse Young's moduli. Now, five appropriate boundary conditions are necessary to compute the constants. These five boundary conditions are given in Table 3.3. It is worth mentioning that the first set of boundary conditions in Table 3.3 to obtain C_{11} can be treated by applying a uniform strain in x_1-direction and preventing the lateral deformation in the x_2x_3-plane by a rigid enclosure. Moreover, the second set of the boundary conditions to determine E_1 is similar to a simple unidirectional tensile test.

3.4 Results

The five boundary conditions were applied to the model, resultant strain energies were obtained by using finite element analysis, and all five constants were determined from the last columns of Table 3.3. Table 3.4 shows the calculated value for all constants for different angles of twist. Figures from 3.16 to 3.20 show the predicted elastic constants as a result of twist angles. As can be seen in Figure 3.16, both C_{11} and E_{11} decrease with an increase in twist angle and an important reduction occurs between *0°* and *20°*. In addition, from Figure 3.17, all three constants K_{23}, G_{23} and G_{12} increase with the twist angle while G_{12} exhibit a major increase from *10°* (10 GPa) to *35°* (45 GPa). Moreover, both K_{23} and G_{23} remain almost constant for a relatively wide range of twist angle (from *0°* to *20°*). Figure 3.18 shows that the longitudinal Poisson's ratio (ν_{12}) reaches its maximum at *30°*. On the other hand, the transverse Poisson's ratio, ν_{23} constantly decreases after a twist angle of *20°*. The transverse modulus (E_{22}) remains almost

constant before 20° and increases rapidly from 18 GPa at *20°* to 45 GPa at *50°*. Figure 3.19 shows all normalized elastic moduli versus twist angle. As can be seen in this figure, all transverse properties, C_{55}, C_{23}, C_{22} remain constant from *0°* to *15°*. On the other hand, C_{11} decreases by 100 % from *0°* to *15°* and reaches to 20% of its initial value (aligned case) at twist angle of 50° while C_{12} doubles from *0°* to *20°*. Finally, the axial Poisson's ratio for three cases: anisotropic elasticity, finite element analysis, and strain energy method is compared in Figure 3.20. In general, a maximum difference of 16% occurs at the angle of 35° between energy method and elasticity.

3.5 Discussions

A helical carbon nanotube fiber was modeled by using the finite element method. This model was compared with anisotropic elasticity presented in Section 2.8.1. These two models showed very good agreement. For both cases ($T=0$ and $v_0=0$), the maximum differences between these two models were about 7 %.

It was shown that strain energy is a very powerful method to compute elastic constants of our model. By choosing proper boundary conditions, it was possible to obtain one elastic constants of the model directly from the strain energy method since only one term appears in Equation 3.9 and other terms remain zero. Since the model is transversely isotropic, five sets of boundary conditions are enough to obtain material stiffness moduli (Equation 3.10). Results from strain energy fit very well with the results from elasticity. While errors between elasticity and finite element method are less than 1% for small twist angles (<20°), a maximum error of 16% observed for larger angles. This difference for large angle of twist can be explained by an approximation in anisotropic elasticity where it is supposed that $\sigma_{r\theta} = 0$. While this assumption seems reasonable for small twist angles, it causes considerable error for large twist angles. Since each layer has a different twist angle, the layers tend to slide with respect to each other producing non-zero $\sigma_{r\theta}$ (Figure 2.41). The other source of the error is the approximation in the finite element model since 6 layers was used to model the helicity, and each layer was divided to 32 elements. Decreasing the size of elements can improve the results but it takes more time for the processors to solve the problem.

Finally, from the Figure 3.16, the Young's modulus of carbon nanotube fiber decreased dramatically even for small twist angles (less than *20°*) without any contribution to the transverse properties since transverse properties remain constants between *0°* to *15°* (Figure 3.18). On the other hand, the stiffness carbon nanotube is directly related to the load transfer between individual nanotubes. It is estimated that to achieve load transfer so that entire cross-section of the bundle becomes effective, SWNT contact length must be on the order of 10 to 120 μm [32]. However, typical length of carbon nanotube is several hundred nanometers [64]. A theoretical study [67] shows that twisting can significantly decrease the required contact length for complete load transfer. Based on textile mechanics, applying a twist to the tubes and hence producing radial force between adjacent tubes can result in better load transfer and, consequently, better mechanical properties of the carbon nanotube rope. Moreover, when a tube in a twisted rope breaks, it still can bear load transferred from the other tubes because of strong radial friction forces (Figure 2.15). Therefore, considering discontinuous, twisted carbon nanotube fibers as tubes with infinite length similar to textile fibers seems acceptable.

Table 3.1

Carbon nanotube crystal properties [61]

Elastic constants	**Value**
E_{11}	514 GPa
$E_{22} = E_{22}$	18.2 GPa
ν_{23}	0.720
$\nu_{12} = \nu_{13}$	0.196
G_{23}	5.29 GPa
$G_{12} = G_{13}$	5.71 GPa

Table 3.2

Torque and Young's modulus for finite element (FE) and elasticity (EL) for Case 2

Twist Angle (°)	T_{EI} **(N.m)**	T_{FE} **(N.m)**	E_{EI} **(GPa)**	E_{FE} **(GPa)**	**Error** T **(%)**	**Error** E **(%)**
0	-9.8×10^{-27}	-9.5×10^{-27}	514	513	3.0	0.05
5	-4.9×10^{-25}	-4.7×10^{-25}	509	509	2.8	0.01
10	-9.5×10^{-25}	-9.2×10^{-25}	495	496	2.6	0.11
15	-1.4×10^{-24}	-1.3×10^{-24}	471	472	2.3	0.32
20	-1.7×10^{-24}	-1.6×10^{-24}	435	438	1.7	0.69
25	-1.9×10^{-24}	-1.9×10^{-24}	388	393	0.8	1.20
30	-1.9×10^{-24}	-1.9×10^{-24}	332	339	0.3	2.03
35	-1.8×10^{-24}	-1.8×10^{-24}	270	279	2.1	3.27
40	-1.5×10^{-24}	-1.5×10^{-24}	209	220	4.7	5.04
45	-1.1×10^{-24}	-1.2×10^{-24}	155	167	9.0	7.61
50	-7.0×10^{-25}	-8.2×10^{-25}	111	123	16.5	11.12

Table 3.3

Boundary conditions used to compute the elastic constants

Set	Constant	Boundary conditions	Boundary displacement	Strain Energy
1	C_{11}	$\varepsilon_{11}^0 = \varepsilon^0$	$u_1^0 = \varepsilon^0$ $u_{r=R}^0 = 0$	$W = \frac{1}{2} V C_{11} (\varepsilon^0)^2$
2	E_1	$\varepsilon_{11}^0 = \varepsilon^0$ $\varepsilon_{22}^0 = -\nu_{12}\varepsilon^0$ $\varepsilon_{33}^0 = -\nu_{12}\varepsilon^0$	$u_1^0 = \varepsilon^0 x_1$	$W = \frac{1}{2} V E_1 (\varepsilon^0)^2$
3	G_1	$\varepsilon_{12}^0 = 0.5\varepsilon^0$ $\varepsilon_{21}^0 = 0.5\varepsilon^0$	$u_1^0 = 0$ $u_2^0 = \varepsilon^0 x_1$ $u_3^0 = 0$	$W = \frac{1}{2} V G_1 (\varepsilon^0)^2$
4	G_{23}	$\varepsilon_{23}^0 = 0.5\varepsilon^0$ $\varepsilon_{32}^0 = 0.5\varepsilon^0$	$u_1^0 = 0$ $u_2^0 = 0.5\varepsilon^0 x_3$ $u_3^0 = 0.5\varepsilon^0 x_2$	$W = \frac{1}{2} V G_{23} (\varepsilon^0)^2$
5	K_{23}	$\varepsilon_{22}^0 = \varepsilon^0$ $\varepsilon_{33}^0 = \varepsilon^0$	$u_1^0 = 0$ $u_2^0 = \varepsilon^0 x_2$ $u_3^0 = \varepsilon^0 x_3$	$W = 2 V K_{23} (\varepsilon^0)^2$

Table 3.4

Variation of elastic constants with the angle of twist*

Angle(°)	G_{23} (GPa)	G_{12} (GPa)	K_{23} (GPa)	C_{11} (GPa)	E_{11} (GPa)	$E_2 = E_3$ (GPa)	$\nu_{12} = \nu_{13}$	ν_{23}
0	5.29	5.71	32.82	519	514	18.20	0.19	0.72
5	5.29	6.62	32.77	410	400	18.16	0.28	0.72
10	5.31	9.30	32.65	285	272	18.15	0.32	0.71
15	5.39	13.62	32.53	221	204	18.28	0.36	0.70
20	5.59	19.33	32.54	187	168	18.77	0.38	0.68
25	5.99	26.10	32.86	166	146	19.86	0.39	0.66
30	6.72	33.51	33.70	151	130	21.84	0.39	0.62
35	7.90	41.04	35.33	139	118	24.99	0.39	0.58
40	9.67	48.12	38.05	129	107	29.59	0.38	0.53
45	12.20	54.09	42.15	119	96	35.86	0.37	0.47
50	15.62	58.33	47.93	110	85	43.97	0.36	0.41

*Note that the last three columns are calculated using Equations 3.15 to 3.17.

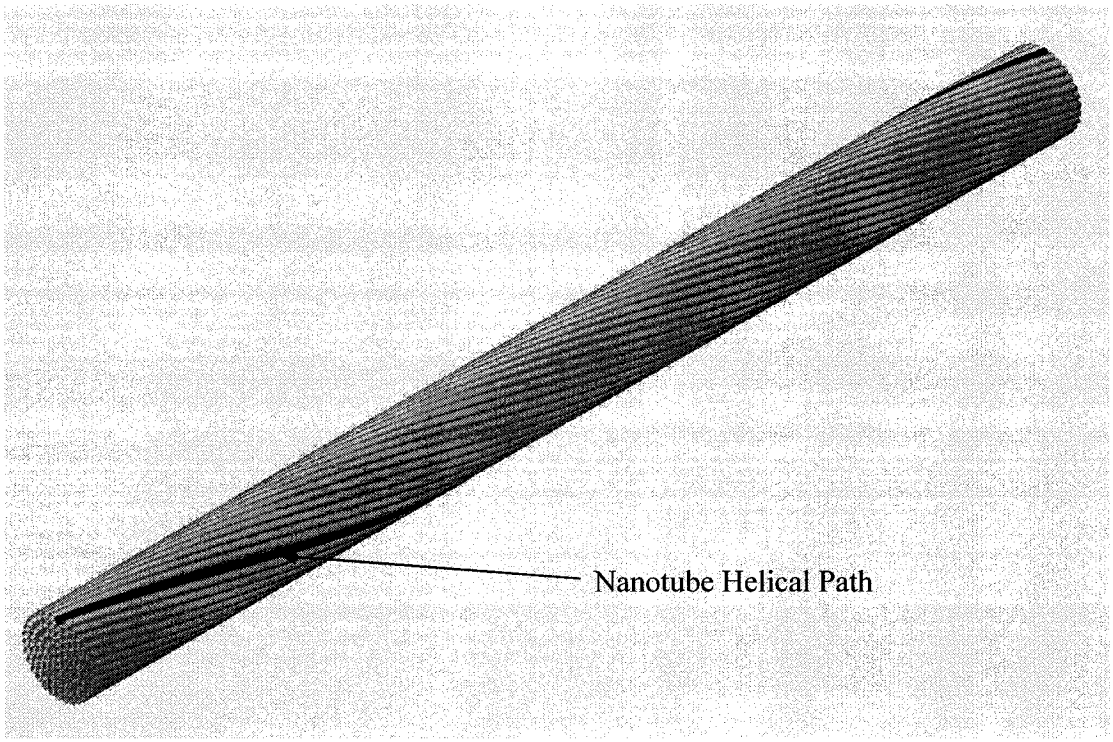

Figure 3.1 Helical carbon nanotube fiber.

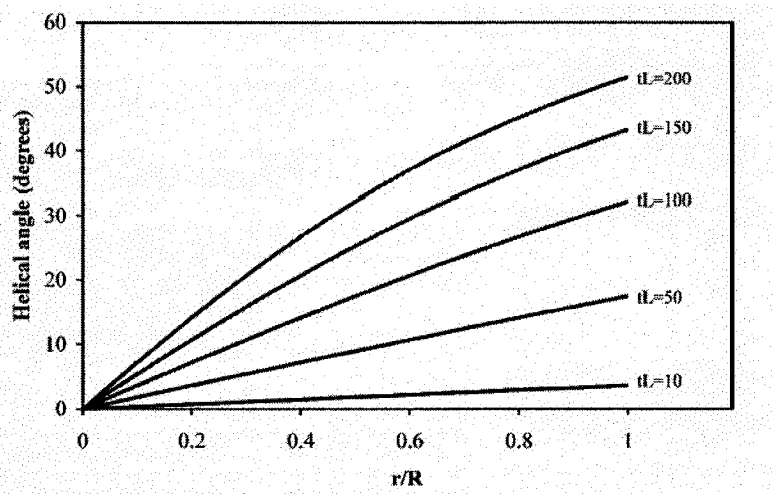

Figure 3.2 Helical angles versus radial position [61].

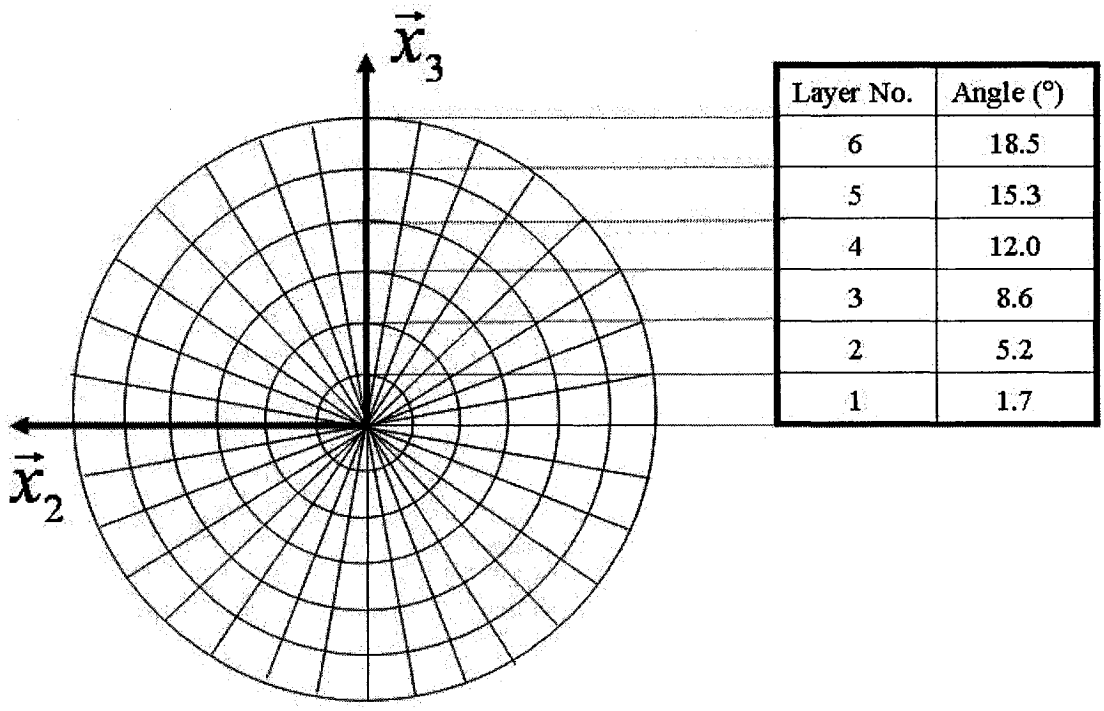

Layer No.	Angle (°)
6	18.5
5	15.3
4	12.0
3	8.6
2	5.2
1	1.7

Figure 3.3 Angle of twist for a 6-layer model with a maximum twist angle of 20°.

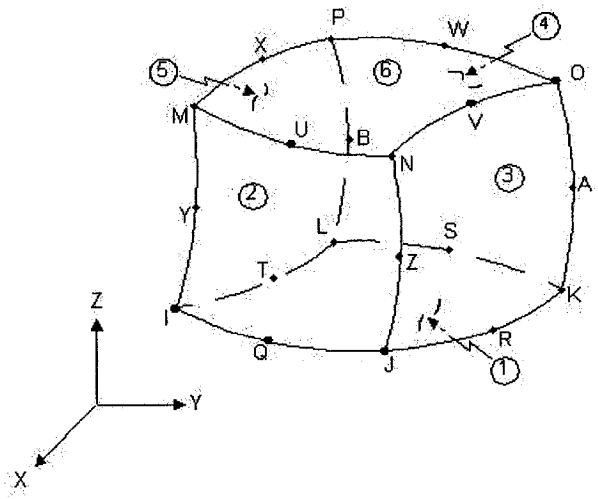

Figure 3.4 ANSYS definition of the 20-node element (ANSYS Solid 191 [72]).

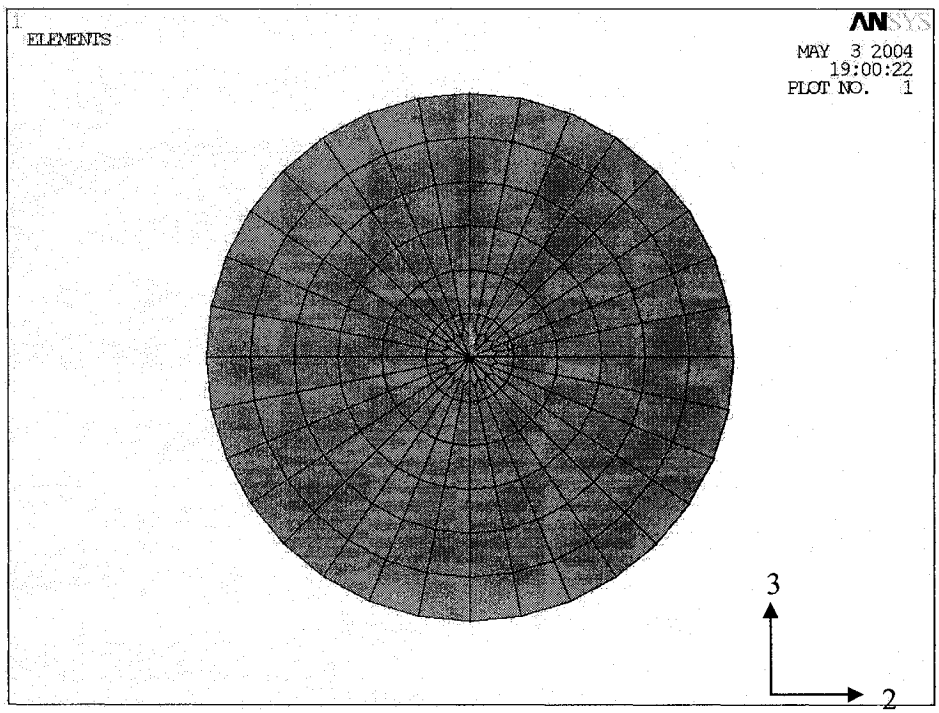

Figure 3.5 Cross section view of the mesh.

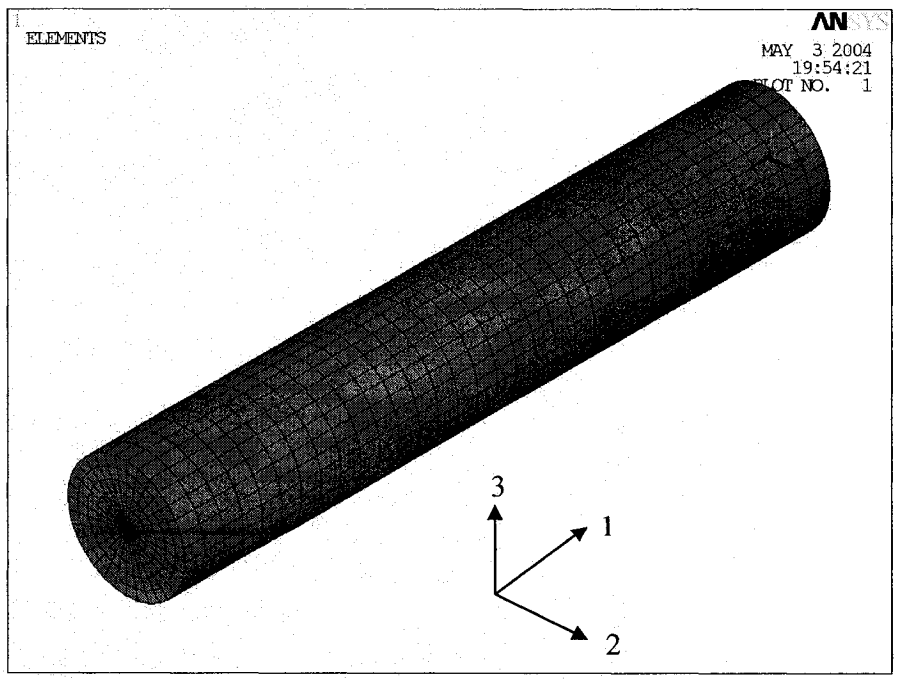

Figure 3.6 Isometric view of the mesh.

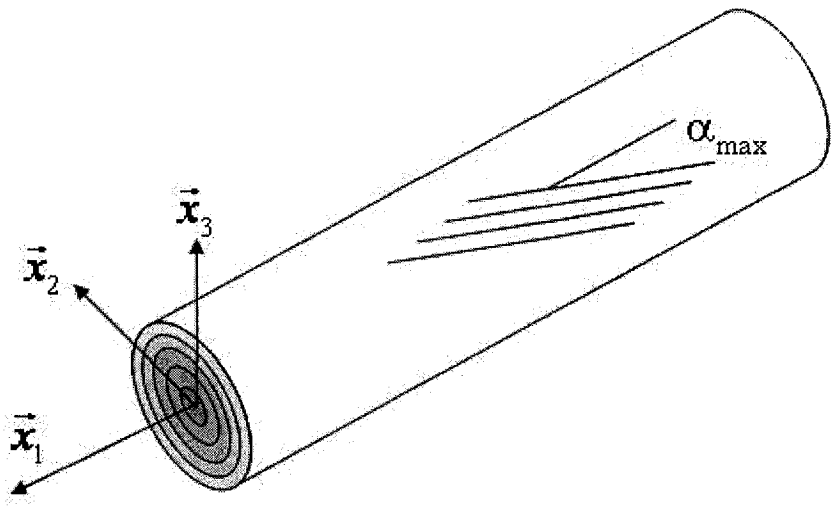

Figure 3.7 Reference coordinate system.

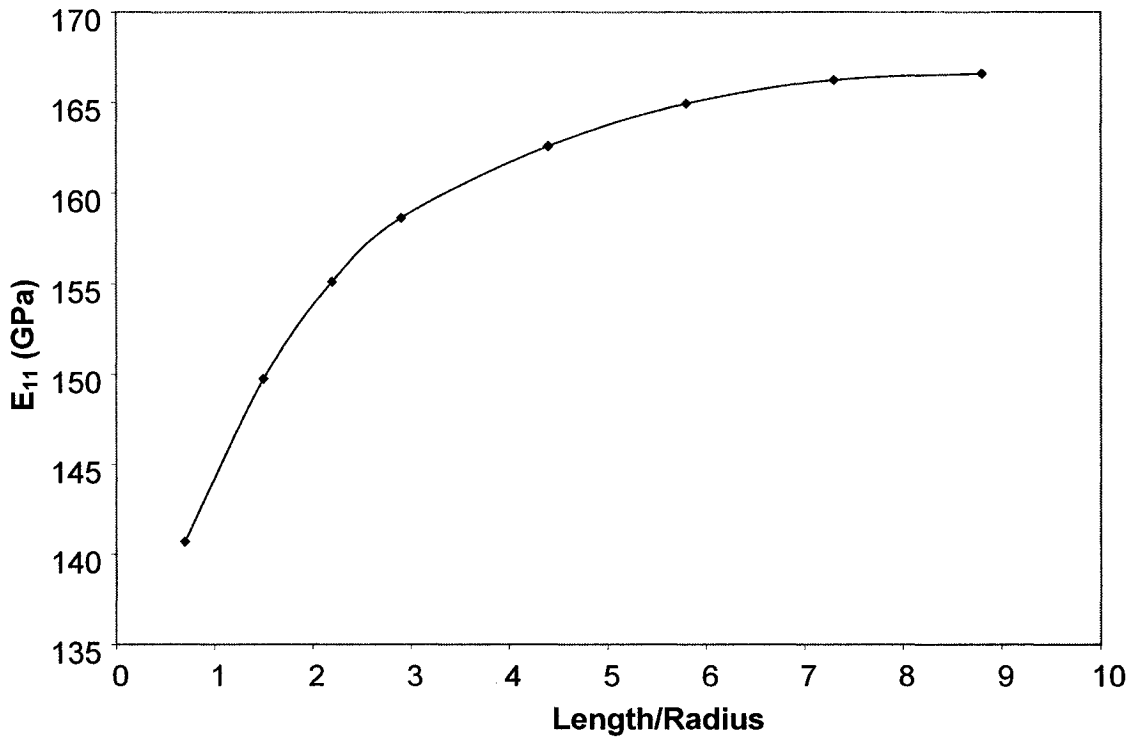

Figure 3.8 Nanotube fiber Young's modulus as a function of the aspect ratio for a twist angle of 20°.

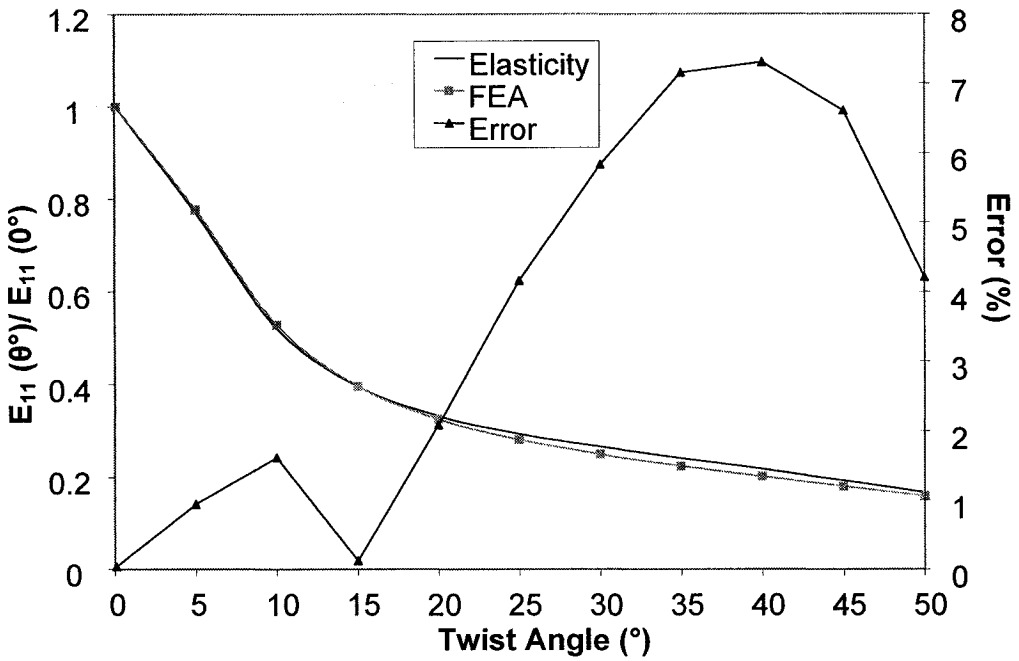

Figure 3.9 Normalized nanotube fiber Young's modulus and errors between finite element method and elasticity for Case 1 as a function of angle of twist.

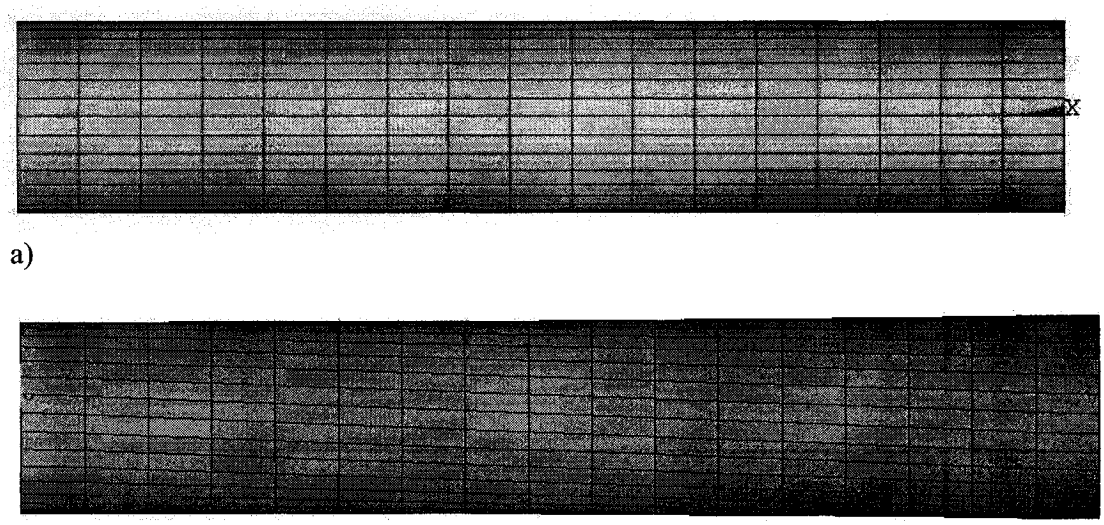

a)

b)

Figure 3.10 a) Undeformed fiber, b) deformed fiber under extensional strain for case showing the induced rotation.

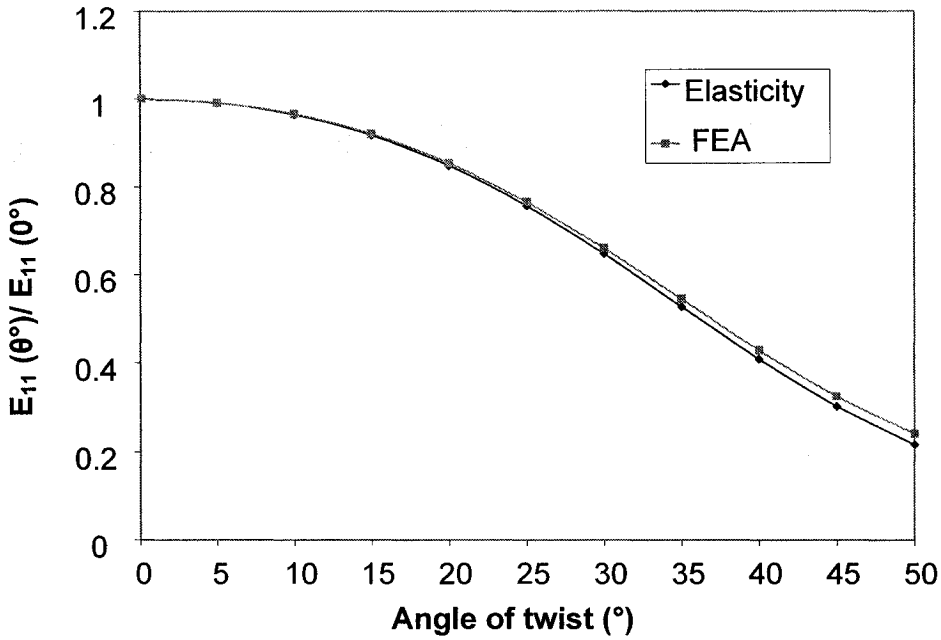

Figure 3.11 Normalized nanotube Young's modulus ratio as a function of angle of twist for Case 2.

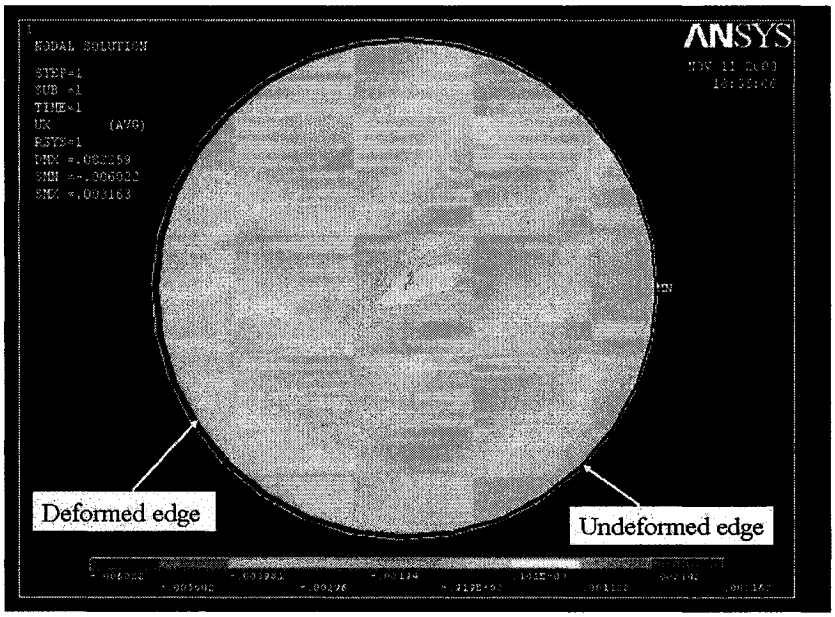

Figure 3.12 Radial displacement of the fiber under longitudinal extension for Case 1 with a twist angle of *20°*.

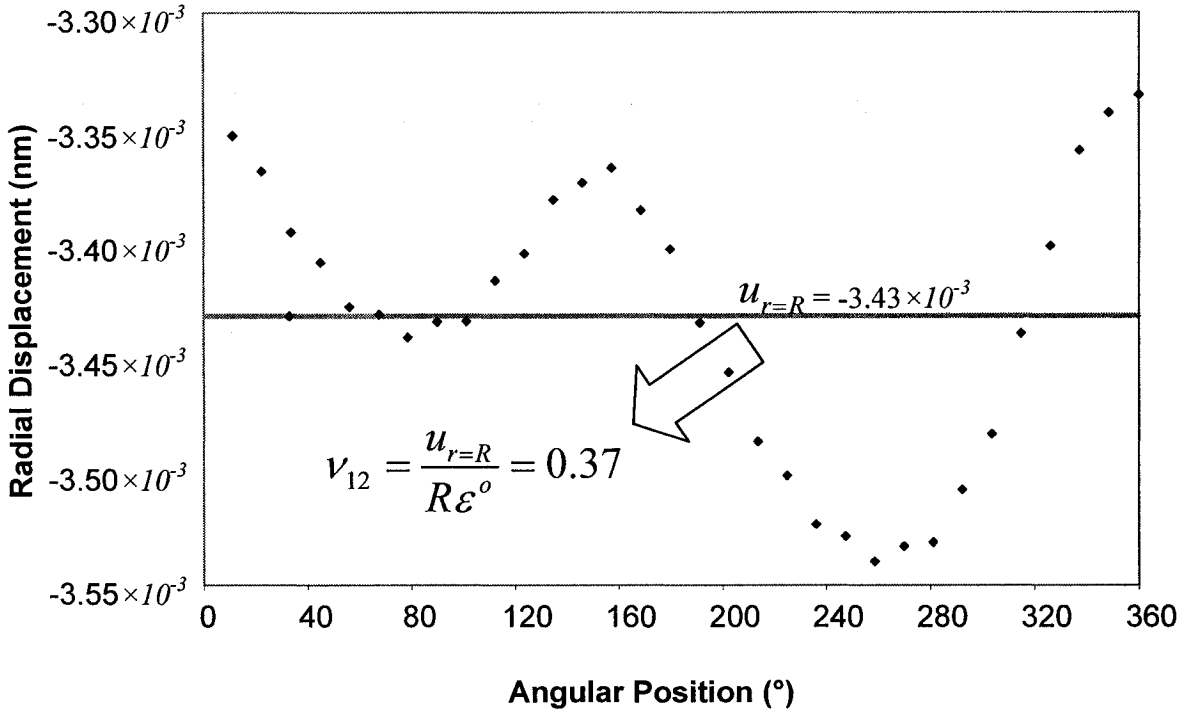

Figure 3.13 Average nodal displacement for the outermost layer nodes as a function of angular position for Case 1 with a twist angle of 20°.

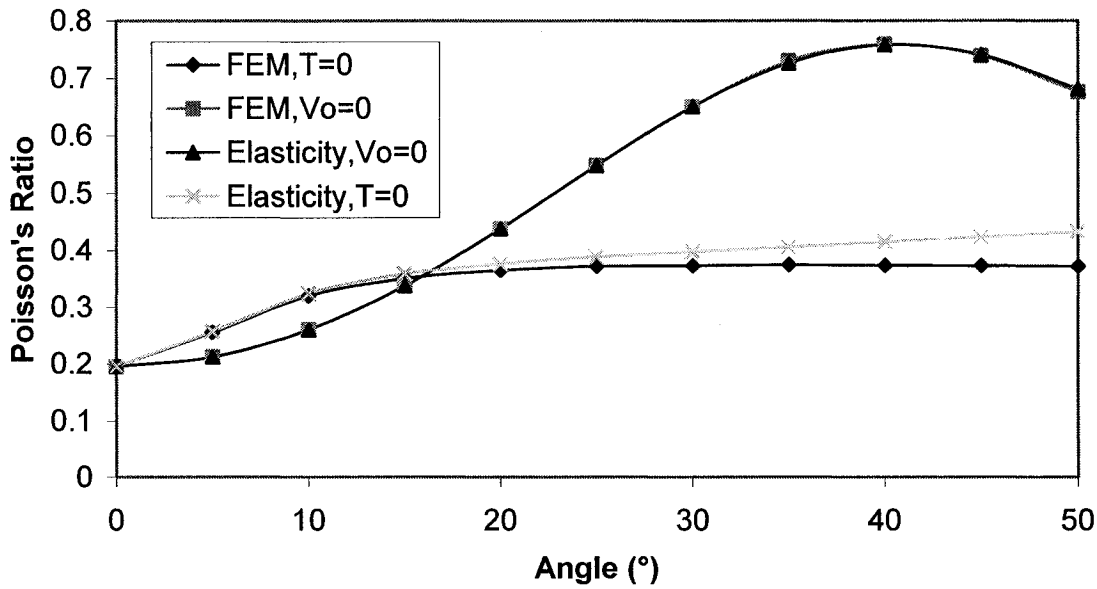

Figure 3.14 Nanotube fiber Poisson's ratio as a function of twist angle.

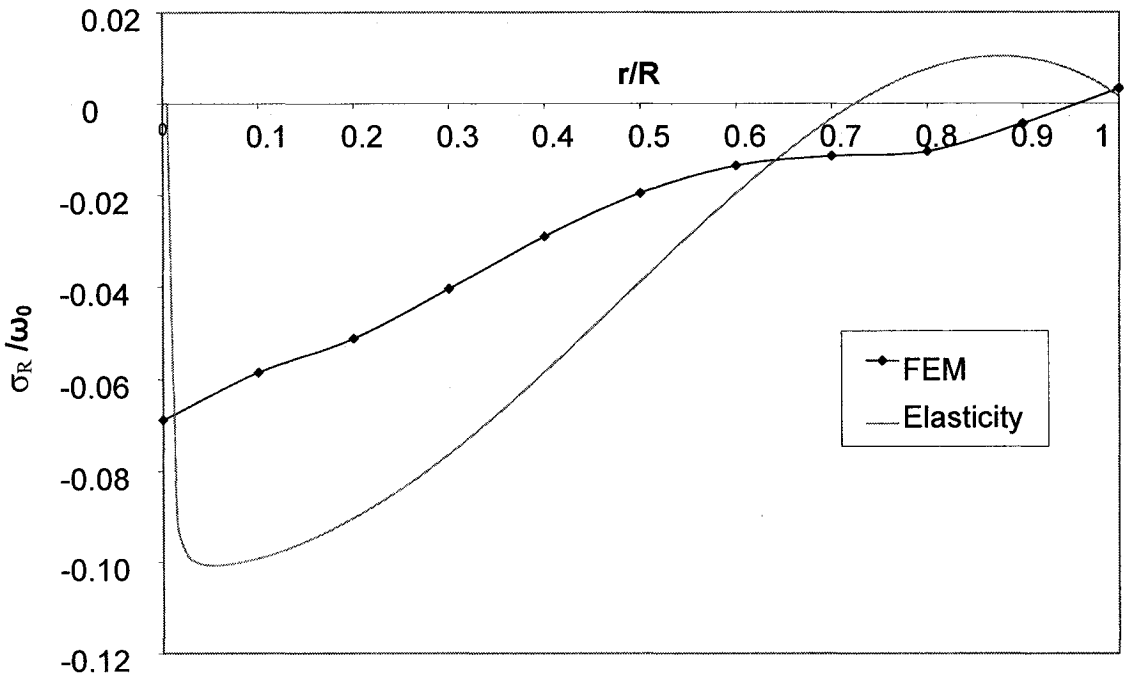

Figure 3.15 Radial stress (σ_R) as a function of radial position.

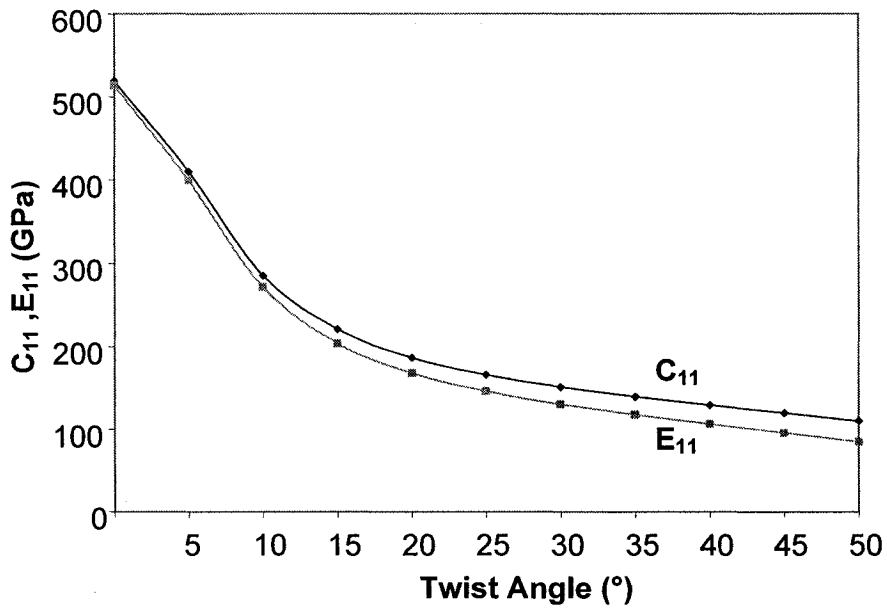

Figure 3.16 Nanotube fiber longitudinal Young's modulus and elastic constant C_{11} versus the angle of twist.

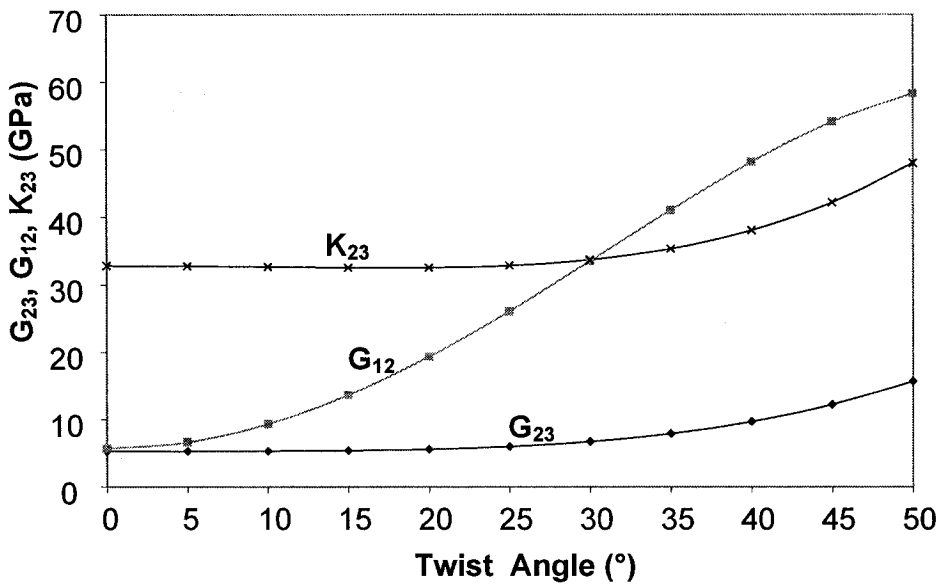

Figure 3.17 Nanotube fiber G_{23}, G_{12}, and K_{23} as a function of angle of twist.

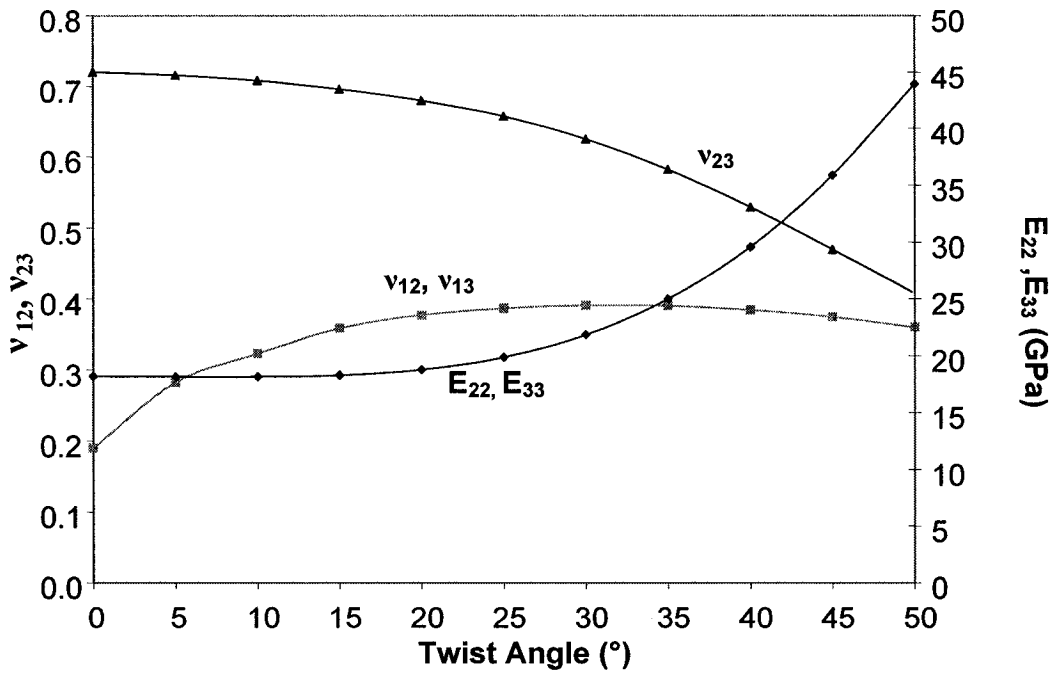

Figure 3.18 Nanotube fiber longitudinal, transverse Poisson's ratio and transverse Young's modulus versus angle of twist.

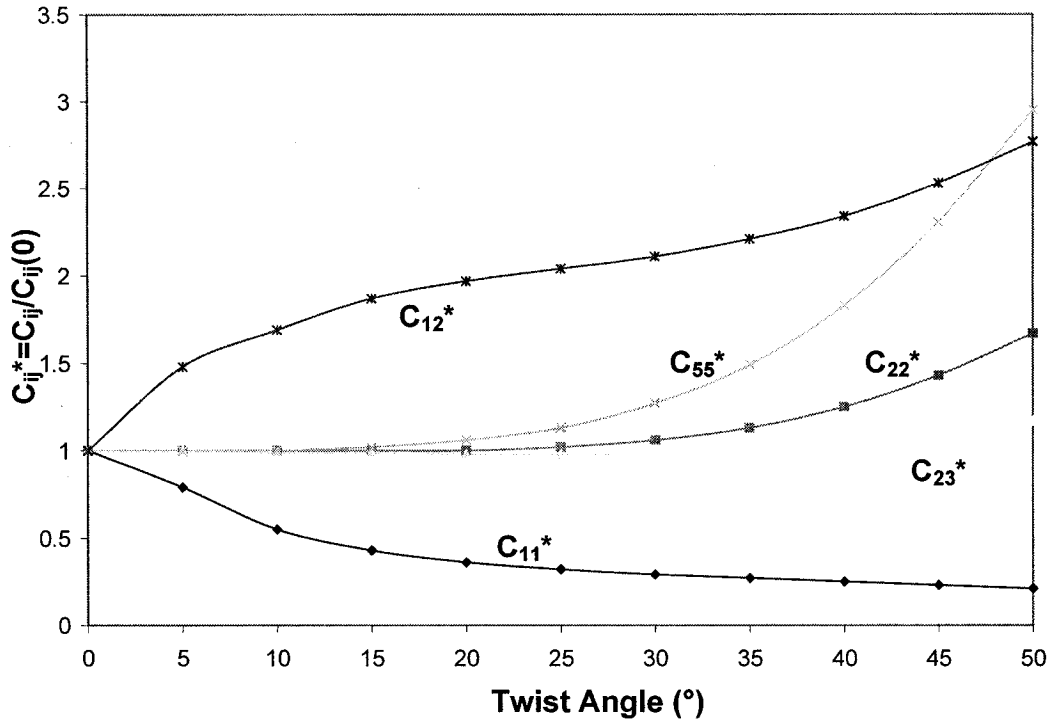

Figure 3.19 Nanotube fiber elastic moduli as a function of angle of twist.

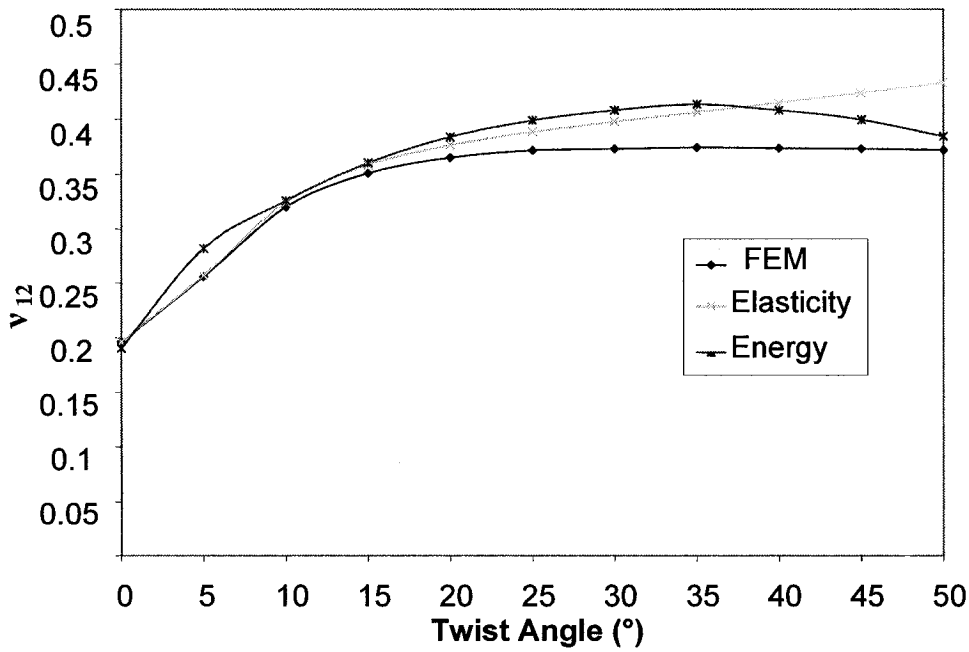

Figure 3.20 Comparison of nanotube fiber axial Poisson's ratio obtained from energy method, elasticity and finite element.

Chapter 4

Self Similar Analysis

As reviewed in Chapter 2, carbon nanotubes have extraordinary high Young's modulus at the nanoscale. The question whether the nanotube moduli change from the nanoscale to the microscale, where conventional continuum mechanics is valid, has yet to be answered. Therefore, in this chapter we use the idea of *self-similar* analysis to relate the elastic properties of carbon nanotube at the nanoscale to those of a carbon nanotube/polymer fiber at the microscale. In this approach, the elastic properties of carbon nanotube crystal or array are considered as inputs to our model. Then, the energy method is used in combination with conventional micromechanics to determine the elastic properties of carbon nanotube/polymer fibers at different scales.

4.8 Definition

The goal, here, is to span three orders of magnitude from the nanoscale to the microscale by using the methodology depicted in Figure 4.1. The self-similar method developed by Pipes and Hubert [79] is used to predict the properties of a nano-array, nano-wire, and micro-fiber. In this analysis, the properties of carbon nanotube array are obtained from Popov [24] and Salvetat *et al.* [75]. Then, the properties of the twisted nano-array are determined by using the energy method explained in detail in Chapter 3 (Step 1). These properties are later used to determine the properties of a second helical array called nano-wire made of the helical nano-array suspended in a polymer (Step 2). In order to obtain the polymer/nanotube composite properties, a conventional micromechanics model (self-consistent field model [80]) is used. Finally, the nano-wires are assembled in the third helical array called the micro-fiber (Step 3). This three-step analysis is self-similar since the geometry used for all steps is identical but different in scale. Here a *(5,5)* SWNT is used for our SWNT/polymer model. Figure 4.2-a shows the diameter for the SWNT (1.38×10^{-9} *m*), the nano-array (1.48×10^{-8} *m*), the nano-wire (1.69×10^{-7} *m*), and the micro-fiber (1.93×10^{-6} *m*), while Figure 4.2-b gives the number of SWNT per unit length of the model at each step.

Modeling the interaction between the carbon nanotube and the polymer is very complex. In our model we assume that there is a perfect load transfer between the polymer and the nanotube. While this approximation is acceptable when spanning from the nano-wire to the micro-fiber, it is not entirely true when spanning from the nano-array to the nano-wire since the SWNT and the polymer are quite dissimilar at that scale [79]. Figure 4.3 shows a flowchart that describes the procedure used to obtain the elastic properties of the carbon nanotube/polymer fiber. It is worth mentioning that while the volume fraction of the carbon nanotube can theoretically reaches 90.6% (Section 2.6), a volume fraction of 70% is considered as a practical upper bound value [79].

4.9 Nano-array properties

Popov [24] used molecular dynamics (Section 2.7) to obtain four out of five constants to describe the elastic behavior of carbon nanotube arrays. It is worth noting that the coordinate system shown in Figure 3.4 is different from the coordinate system used by Popov. While in our model axis *1* is along the fiber and axes *2* and *3* are transverse axes, Popov defined axis *3* along the fiber (Figure 2.26). The only constant that remains uncalculated is the axial shear modulus (G_{12}). In order to estimate this constant we employed a first order model described by Salvetat [75]. Based on Figure 4.4, d is the tube distance; R is the carbon nanotube fiber; A_t is the cross sectional area occupied by each tube and a is the lattice constant, thus:

$$a = 2R + d \tag{4.1}$$

$$A_t = a^2 \cos \pi / 6 \tag{4.2}$$

If we define c as the interplanar spacing of graphite (c = *0.3354 nm*), the first order approximation between the shear modulus of the carbon nanotube rope (G_{12}) and the graphite shear modulus (G_g) can be defined as:

$$G_{12} = \frac{c_n}{c} G_g \tag{4.3}$$

where as can be seen from Figure 4.4:

$$c_n = a\cos(\pi/6) = 0.866\ a \tag{4.4}$$

By considering $G_{graphite}$= *4.5 GPa* (C_{44} of single crystal graphite) [75] and the image analysis shown in Figure 2.32 (a = *1.48 nm*, c_n = *1.28 nm*), Equation 4.3 gives an axial shear modulus equal to 17.2 GPa. In summery, these five independent parameters used as elastic properties for the *(5,5)* SWNT array are given in Table 4.1. It is worth noting that in this table, G_{23} is not an independent parameter as we have:

$$G_{23} = \frac{1}{2}(C_{22} - C_{23}) \tag{4.5}$$

while C_{22} and C_{23} are function of the other five elastic constants. Appendix II provides the relations between engineering constants (G_{12}, E_{11}, E_{22}, υ_{12}, υ_{23}) and the elastic constants (C_{ij}).

4.10 Elastic constants calculation of polymer/SWNT fiber

In order to obtain the properties of the twisted polymer/SWNT fiber, the method explained in Chapter 3 is used. To consider the polymer in the model, *self-consistent field models* [89] (Figure 4.5) were used. We assume that the carbon nanotube array is located at the center of the composite fiber while the polymer is surrounding it. Only the relations to get the properties of composite fiber are presented here, the detail to obtain these relations can be found in [80]. In these equations, subscripts F, CN and P stand for the carbon nanotube/polymer fiber, the carbon nanotube and the polymer respectively. Also, V_f is the carbon nanotube volume fraction. Figure 3.7 shows the coordinate system used in our model:

$$E_{11F} = E_{11CN}V_f + E_{11P}(1-V_f) + \frac{4(\upsilon_P - \upsilon_{12CN})^2 K_{23CN}K_{TP}G_P(1-V_f)V_f}{(K_{23CN}+G_P)K_{TP} + (K_{23CN}-K_{TP})G_PV_f} \tag{4.6}$$

$$\upsilon_{12F} = \upsilon_{12CN}V_f + \upsilon_P(1-V_f) + \frac{(\upsilon_P - \upsilon_{12CN})(K_{TP}-K_{23CN})G_P(1-V_f)V_f}{(K_{23CN}+G_P)K_{TP} + (K_{23CN}-K_{TP})G_PV_f} \tag{4.7}$$

$$K_{23F} = \frac{(K_{23CN} + G_P)K_{TP} + (K_{23} - K_{TP})G_P V_f}{(K_{23CN} + G_P) - (K_{23CN} - K_{TP})V_f} \tag{4.8}$$

$$G_{12F} = G_P \frac{(G_{12CN} + G_P) + (G_{12CN} - G_P)V_f}{(G_{12CN} + G_P) - (G_{12CN} - G_P)V_f} \tag{4.9}$$

$$G_{23F} = \frac{G_P\left[K_{TP}(G_P + G_{23CN}) + 2G_{23CN}G_P + K_{TP}(G_{23CN} - G_P)V_f\right]}{K_{TP}(G_P + G_{23CN}) + 2G_{23CN}G_P - (K_{TP} + 2G_P)(G_{23CN} - G_P)V_f} \tag{4.10}$$

Finally, we have:

$$E_{22F} = \frac{1}{\frac{1}{4K_{23F}} + \frac{1}{4G_{23F}} + \frac{v_{12F}^2}{E_{11F}}} \tag{4.11}$$

$$v_{23} = \frac{2E_{11F}K_{23F} - E_{11F}E_{22F} - 4v_{12F}^2 K_{23F}E_{22F}}{2E_{11F}K_{23F}} \tag{4.12}$$

Here, the polymer is assumed to be isotropic. K_{TP} is the polymer plane strain bulk modulus, which is different from the bulk modulus (K):

$$K_{TP} = \frac{E_P}{2 - 2v_P - 4v_P^2} \tag{4.13}$$

It is worth mentioning that the axial properties E_{11} and v_{12} follow the rule of mixtures very well; therefore, the third terms in both Equations 4.6 and 4.7 can be omitted without significant errors. Moreover, from Equations 4.11 and 4.12, it is clear that E_{22} and v_{23} are given as a function of other constants and are not independent.

In summary, based on the flowchart shown in Figure 4.3, inputs to the model are: the elastic constants of the carbon nanotube array (Table 4.1), the angle of twist (between 0° to 50°), the carbon nanotube volume fraction (70% as a practical upper limit), and the polymer elastic properties. Table 4.2 summarizes the properties of three isotropic polymers considered in our study.

4.11 Results

Table 4.3 summarizes the variation of the elastic constants for different steps shown in the flowchart (Figure 4.3) for a LaRC-SI/SWNT micro-fiber with different twist angles. Figures 4.6 to 4.12 show the engineering elastic constants (E_{11}, E_{22}, G_{12}, G_{23}, υ_{12}, υ_{23}, and K_{23}) as a function of twist angles for three scaling steps: the nano-array (Step 1), the nano-wire (Step 2) and the micro-fiber (Step 3). From Figure 4.6, the longitudinal Young's modulus (E_{11}) significantly decreases even for small twist angles (less than 20°). From Table 4.1, the initial Young's modulus of the SWNT crystal is 580 GPa; however, after scaling from the nanoscale to the microscale, the micro-fiber Young's modulus drops to 137 GPa for a twist angle of 10°. This is a four-fold decrease for the Young's modulus even for small twist angles.

Figure 4.7 shows the variation of the transverse Young's modulus (E_{22}) as a function of the twist angle. In spite of E_{11}, by increasing the twist angle E_{22} increases. The same trend was previously observed in Figure 3.18. Based on Equation 4.11, E_{22} does not follow the rule of mixtures. It is clear that for small twist angles (<20°), the transverse Young's modulus remains almost constants. Moreover, in Step 3, the modulus remains almost constant since the increase due to the twist angle cancels out the decrease due to the volume fraction.

Figure 4.8 shows the axial Poisson's ratio (υ_{12}) as a function of the twist angle. While Step 1 is very similar to Figure 3.18 with a maximum of υ_{12} at a twist angle of 40°, in Steps 2 and 3 this maximum shifts to 20° and 10° respectively. Also, since the Poisson's ratio of the polymer (0.40) is higher than the axial Poisson ratio of the SWNT (0.18), the addition of the polymer causes an increase of the Poisson's ratio at each step. On the other hand, the transverse Poisson's ratio (υ_{23}) decreases as twist angle increases (Figure 4.9). Also, the addition of the polymer causes the Poisson's ratio to decrease for the second and third steps (Equation 4.12).

The axial shear modulus (G_{12}) increases with an increase of the twist angle (Figure 4.10). While this increase is considerable for the first step (i.e. for twist angle of 50°, it increases by more than 300% compared to the 0° twist angle), for the second and third steps, it becomes very moderate since the negative effect of the addition of the polymer

cancels out the positive effect of twist angle. From Table 4.3, the addition of the polymer in the Step 2 has a significant effect. For instance, a nano-array with a twist angle of 20° has a G_{12} equal to 31.08 GPa. With the addition of the polymer, G_{12} is reduced to 8.45 GPa based on Equation 4.9. From Figure 4.11, the transverse shear modulus (G_{23}) increases by twist angles. This increase, in spite of E_{11}, mainly starts at large twist angles (>20°) and the effect of adding the polymer can be observed only at large twist angles especially between Step 1 and Step 2.

Finally, Figure 4.12 shows that the twist angle does not have any effect on the transverse bulk modulus for small twist angles. A small increase can be observed for twist angles of 30° or more only for the first step. Also, the effect of the volume fraction between Step 1 and Step 2 is more important than between Step 2 and Step 3.

Figures 4.13 to 4.16 show the scaling effect on the elastic properties of the SWNT/LaRC-SI fiber for four different twist angles (0°, 10°, 30°, 50°). Based on Figure 4.13, both scaling and twist angles can cause the reduction of the axial Young's modulus. Here, it is again clear that for small twist angles, the reduction of E_{11} is very significant. Figures 4.14 and 4.15 show the scaling effect on both the transverse and the axial Poisson's ratios. From Figure 4.14, υ_{23} is sensitive to larger twist angles in spite of E_{11} (0° fiber and 10° fiber have very little difference) and the effect of scaling is important especially for medium twist angles (i.e. 30°). The behavior for the υ_{12} is complicated here (Figure 4.15). While the axial Poisson's ratio increases by scaling for any twist angle, the fiber with twist angle of 30° has the maximum value of Poisson's ratio compared to the other fibers, and the fiber with twist angle of 10° is the most sensitive to the scaling. Figures 4.16 and 4.17 show the scaling effect on the transverse Young's modulus and the elastic constants for a twist angle of 20°, respectively. As can be seen, all the elastic constants decrease by scaling because of the addition of polymer. The only properties that remained almost constant for this specific twist angle is C_{44}= G_{23}. This fact can also be seen in Figure 4.11. Finally, Figure 4.18 shows the difference between C_{11} and E_{11}. As can be seen the difference between them remains almost constants when scaling.

Three polymers (LaRC-SI, epoxy and polyethylene) were chosen to see the polymer effect on the axial Young's modulus and the axial Poisson's ratio of the fiber with a twist

angle of 20° (Figure 4.19 and 4.20, respectively). The elastic properties of these polymers were given in Table 4.2. From Figure 4.19, it can be seen that the polymer properties can have a major effect on the properties of the fiber. All three fibers have an E_{11} equal to 263 GPa at Step 1, but by adding the polymer at Step 2, the SWNT/epoxy fiber shows higher Young's modulus (129 GPa) comparing to the SWNT/LaRC-SI fiber (109 GPa) and the SWNT/polyethylene fiber (96 GPa). Based on Table 4.2, the epoxy has the highest Young's modulus between these polymers. However, because of the twist angle of the fiber (20°), these differences between the Young's modulus of the fibers with different polymers are more than the effect of the rule of mixture (Equation 4.7). This fact will be clarified when comparing the effects of the twist angle and the polymer on the properties of the fiber. Also, from Figure 4.20, the axial Poisson's ratio of the fiber increases with the addition of polymer. Since polyethylene has the highest Poisson's ratio (Table 4.2), the increase of the axial Poisson's ratio for SWNT/polyethylene is higher than the other two fibers.

Finally, in Figure 4.21 the micro-fiber properties are compared to the published data [4,6,7]. Further details about the carbon nanotube fiber with a high concentration can be found in Section 2.7.1. The total volume fraction of 0.50 and a twist angle of 15° were considered for the model. Vigolo [4] has produced carbon nanotube fibers with a diameter of 35 μm, a volume fraction of 0.5 and an average twist angle of 15° with a modulus of 40 GPa, while Wei [6] has made composite fibers with diameters between 5 and 20 μm and a SWNT volume fraction of 48%, and Baughman [7] has produced SWNT's fibers with a diameter of 50 μm containing around 60% SWNTs by weight.

4.12 Discussions

From Figure 4.6, it was clear that even for small twist angles (<20°) the axial Young's modulus drops dramatically. Therefore, in order to maintain high stiffness of the SWNT crystals, the alignment of the fibers are crucial. However, as mentioned before, this alignment has negative effect on the load transfer efficiency between the tubes. The volume fraction has also an important effect on the fiber modulus reduction. As explained previously, a volume fraction of 70% was considered for each scaling step; therefore, by considering the addition of the polymer to the model twice, the overall

volume fraction of SWNT in the fiber becomes 49%. In order to understand the relative importance of the addition of polymer and the twist angle on the axial Young's modulus, Figure 4.22 shows the E_{11} drop when scaling from nanoscale (SWNT) to the microscale (micro-fiber) considering both the polymer effect and the twist angle effect for three different twist angles. For the twist angle of zero, it is obvious that this drop is only due to adding the polymer to the fiber. However, for the twist angle of 20°, only 15% of the modulus drop is due to the addition of the polymer, and twist angle has a major effect (85%) on the modulus reduction. It was also shown that the transverse properties remain constant for twist angles less than 15°. Moreover, it was shown that the polymer properties can have an important effect on the elastic properties of the SWNT/polymer fiber. For instance, E_{11} of SWNT/epoxy is 32% higher compared to the SWNT/polyethylene for a twist angle of 20°. The modulus comparison between the model developed here and the data of the carbon nanotube/polymer fiber (Figure 4.21) demonstrates the appropriateness of our model to predict the elastic properties of carbon nanotube/polymer fiber. However, our model predicts the modulus relatively higher than the practical results. This could be due to the local defects in the experimental fibers, partial load transfer between tubes instead of complete load transferred considered in our model, and also uncertainty in the type and the diameter of carbon nanotube in the literature since the carbon nanotubes with different diameter have quite different properties (Figure 2.36).

Table 4.1

Properties of *(5,5)* SWNT array

E_{11}^{*}	*580 GPa*
$E_{22} = E_{33}^{*}$	*9.4 GPa*
$\nu_{12} = \nu_{13}^{*}$	*0.18*
ν_{23}^{*}	*0.90*
$G_{12}=G_{13}^{\dagger}$	*17.2 GPa*
$G_{23}^{\ddagger}$	*2.47 GPa*

*Based on Popov [24]

†Based on Salvetat et al [75]

‡Not an independent parameter (See Appendix II).

Table 4.2

Elastic properties of polymers

Polymer	***E (GPa)***	***G (GPa)***	***υ***
Epoxy [82]	*7.20*	*2.64*	*0.36*
Polyethylene [82]	*2.55*	*0.91*	*0.41*
LaRC-SI [69]	*3.80*	*1.36*	*0.40*

Table 4.3

Scaling effect on elastic constants

	Angle	E_{11}	E_{22}	v_{12}	v_{23}	G_{12}	G_{23}	K_{23}
Nano-array Properties (Step 1)	*0°*	*580*	*9.39*	*0.18*	*0.9*	*17.2*	*2.47*	*47.5*
	10°	*417*	*10.21*	*0.25*	*0.89*	*20.87*	*2.7*	*47.34*
	20°	*264*	*13.35*	*0.31*	*0.85*	*31.08*	*3.61*	*47.31*
	30°	*192*	*20.64*	*0.33*	*0.76*	*45.46*	*5.85*	*48.65*
	40°	*151*	*34.17*	*0.33*	*0.63*	*60.15*	*10.48*	*53.46*
	50°	*118*	*57.17*	*0.32*	*0.47*	*70.28*	*19.51*	*65.32*
Apply Polymer (1)	*0°*	*459*	*7.86*	*0.23*	*0.82*	*6.99*	*2.16*	*22.15*
	10°	*330*	*8.34*	*0.28*	*0.81*	*7.51*	*2.31*	*22.12*
	20°	*209*	*10.01*	*0.33*	*0.76*	*8.49*	*2.84*	*22.12*
	30°	*152*	*13.1*	*0.35*	*0.69*	*9.27*	*3.88*	*22.36*
	40°	*120*	*16.98*	*0.35*	*0.6*	*9.75*	*5.31*	*23.17*
	50°	*94*	*20.8*	*0.33*	*0.53*	*9.97*	*6.79*	*24.81*
Nano-wire Properties (Step2)	*0°*	*459*	*7.86*	*0.22*	*0.82*	*6.99*	*2.16*	*22.15*
	10°	*221*	*8.6*	*0.33*	*0.8*	*9.64*	*2.39*	*22.11*
	20°	*109*	*11.24*	*0.36*	*0.72*	*13.17*	*3.26*	*22.37*
	30°	*70*	*15.77*	*0.36*	*0.6*	*15.56*	*4.92*	*23.34*
	40°	*50*	*21.06*	*0.35*	*0.48*	*16.63*	*7.11*	*25.29*
	50°	*38*	*25.92*	*0.34*	*0.38*	*16*	*9.36*	*28.17*
Apply Polymer (2)	*0°*	*363*	*6.9*	*0.26*	*0.77*	*4.46*	*1.95*	*15.32*
	10°	*175*	*7.37*	*0.34*	*0.75*	*5.35*	*2.11*	*15.3*
	20°	*87*	*8.9*	*0.37*	*0.68*	*6.24*	*2.64*	*15.4*
	30°	*56*	*11.12*	*0.37*	*0.59*	*6.71*	*3.49*	*15.78*
	40°	*41*	*13.19*	*0.36*	*0.52*	*6.9*	*4.35*	*16.5*
	50°	*31*	*14.7*	*0.35*	*0.46*	*6.79*	*5.03*	*17.47*
Micro-fiber Properties (Step 3)	*0°*	*363.48*	*6.9*	*0.26*	*0.77*	*4.46*	*1.95*	*15.32*
	10°	*127.38*	*7.51*	*0.36*	*0.74*	*6.44*	*2.16*	*15.32*
	20°	*56.91*	*9.52*	*0.37*	*0.65*	*7.9*	*2.89*	*15.6*
	30°	*35.39*	*12.27*	*0.36*	*0.53*	*8.35*	*4*	*16.3*
	40°	*25.84*	*14.69*	*0.35*	*0.44*	*8.16*	*5.11*	*17.35*
	50°	*20.44*	*16.27*	*0.34*	*0.37*	*7.53*	*5.92*	*18.49*

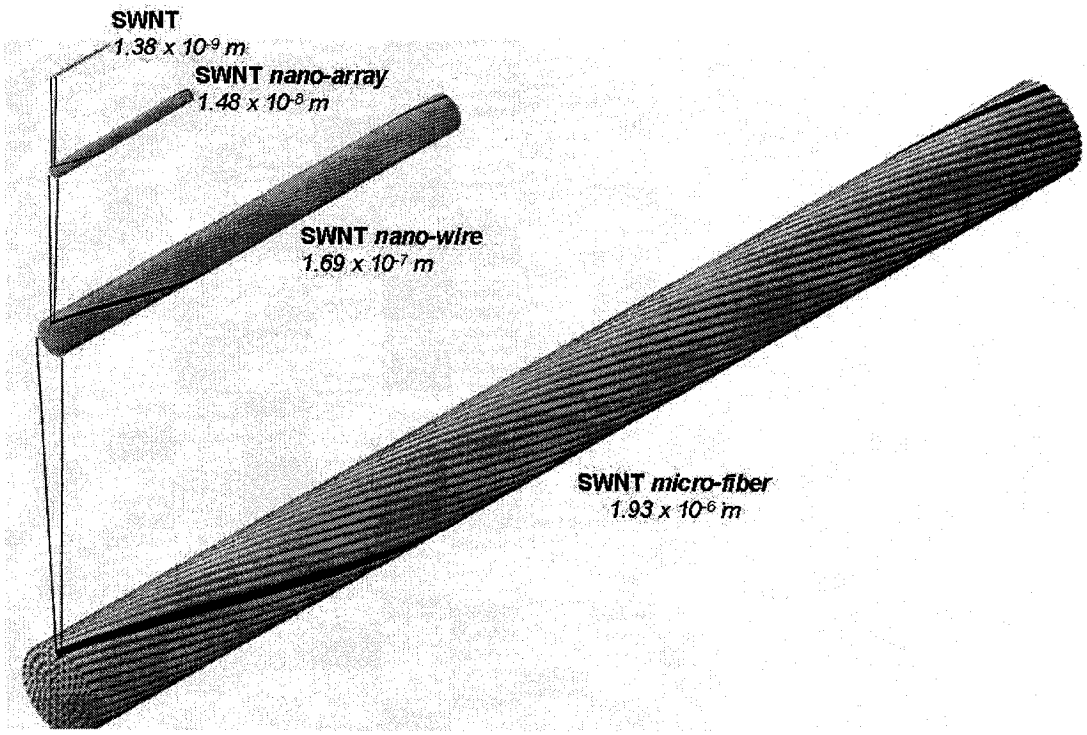

Figure 4.1 Self similar modeling of a twisted array of carbon nanotube/polymer fiber.

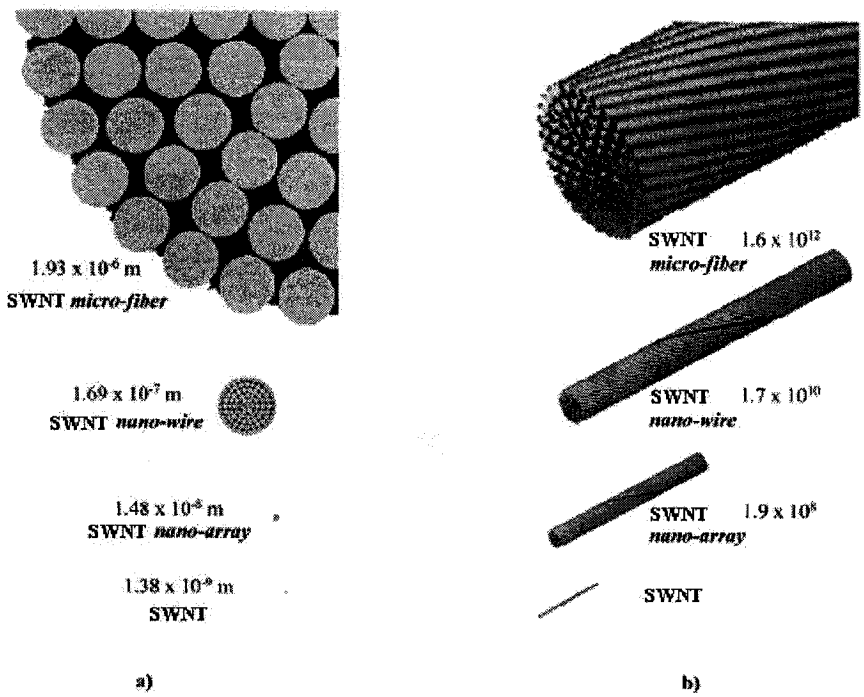

Figure 4.2 a) Dimension b) Number of SWNT for carbon nanotube/polymer fiber [79].

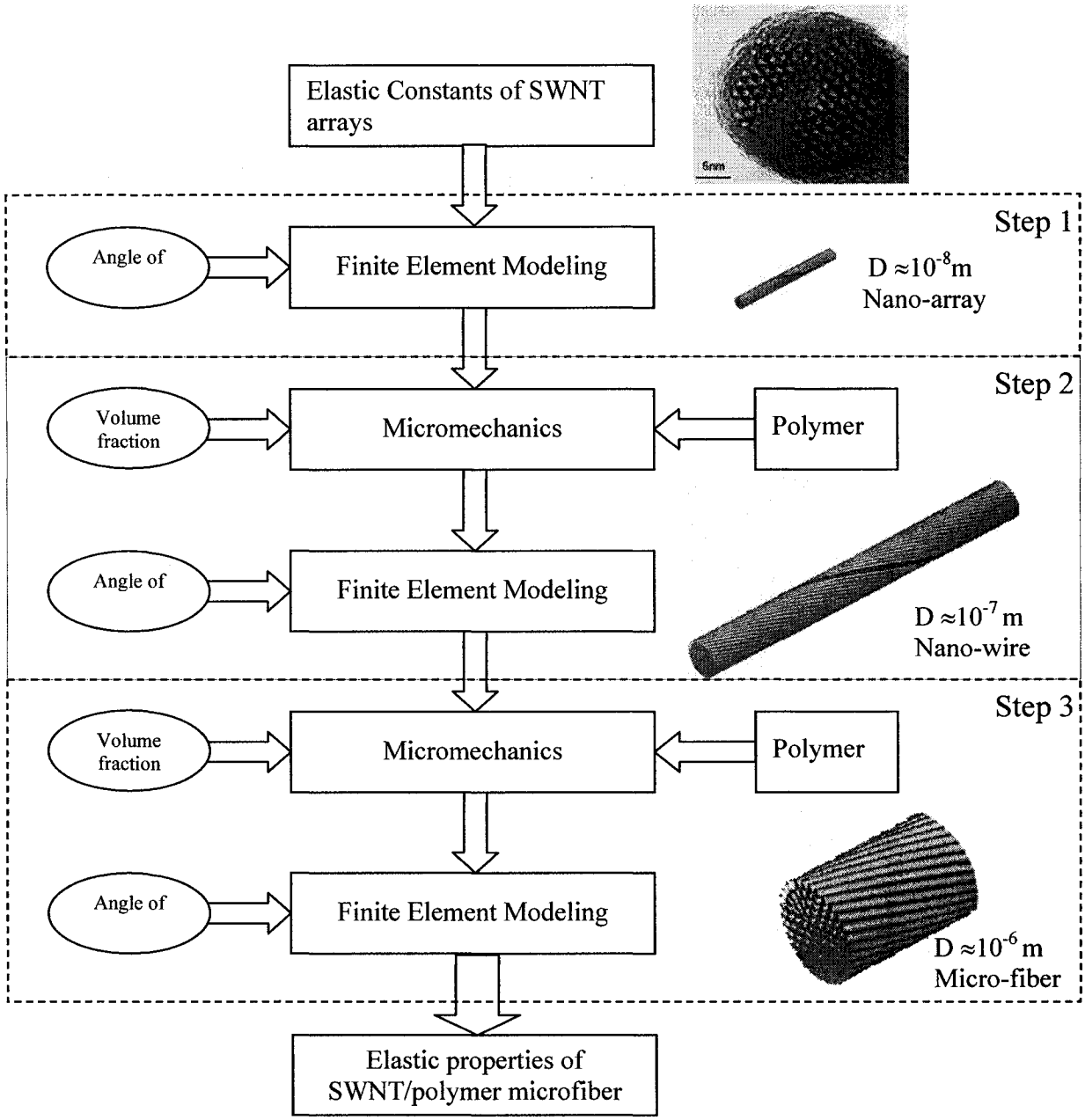

Figure 4.3 Procedure for the self-similar analysis.

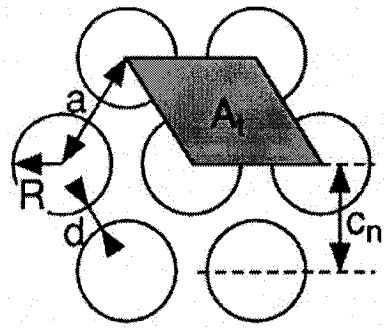

Figure 4.4 Hexagonal packing of a carbon nanotube array with different parameters used to define the model [75].

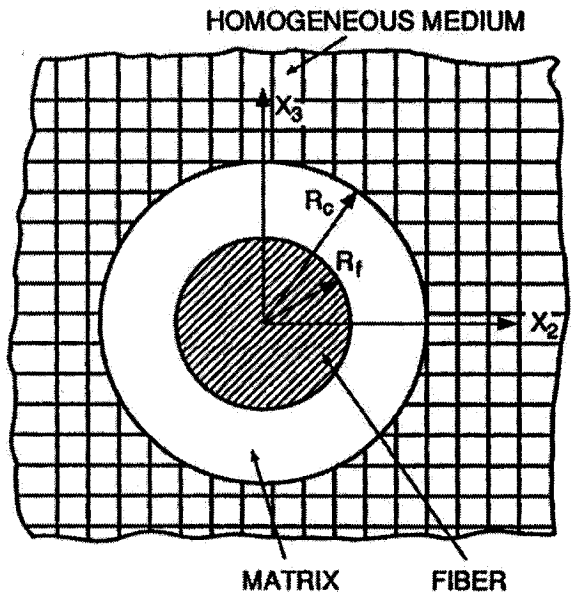

Figure 4.5 Geometry of self-consistent model [80].

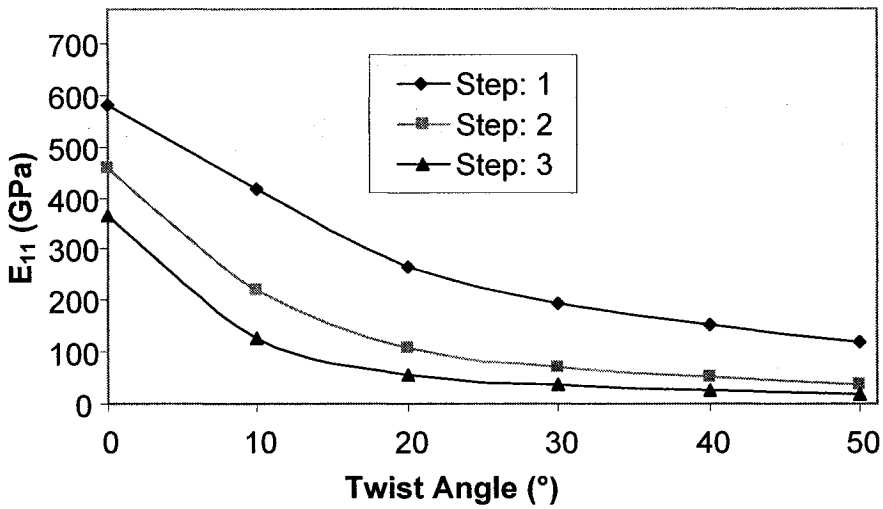

Figure 4.6 Longitudinal Young's modulus of a LaRC-SI/SWNT fiber as a function of twist angle.

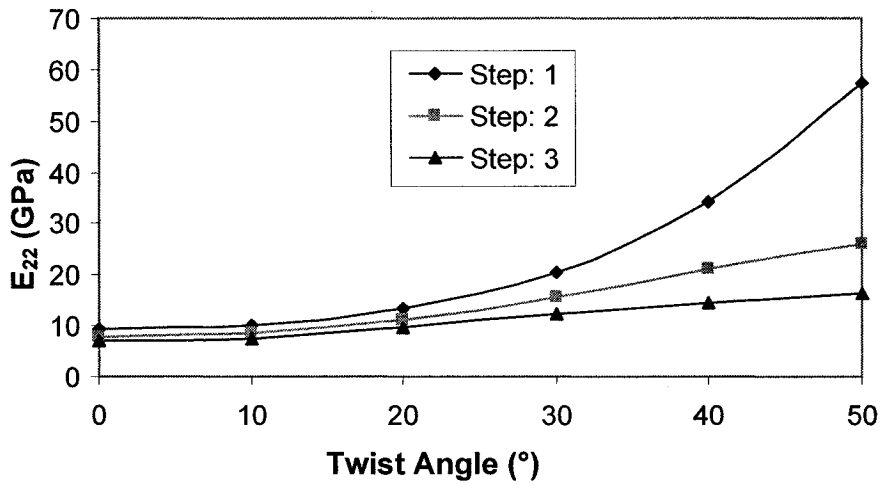

Figure 4.7 Transverse Young's modulus of a LaRC-SI/SWNT fiber as a function of twist angle.

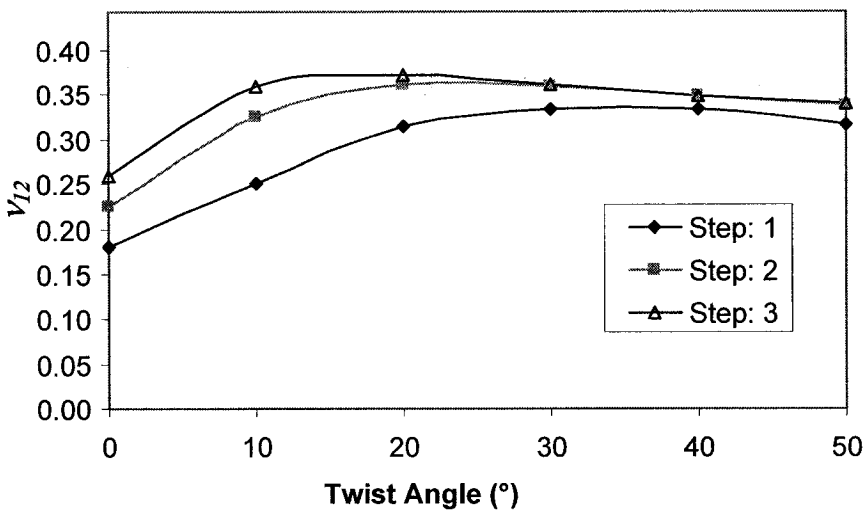

Figure 4.8 Axial Poisson's ratio of a LaRC-SI/SWNT fiber as a function of twist angle.

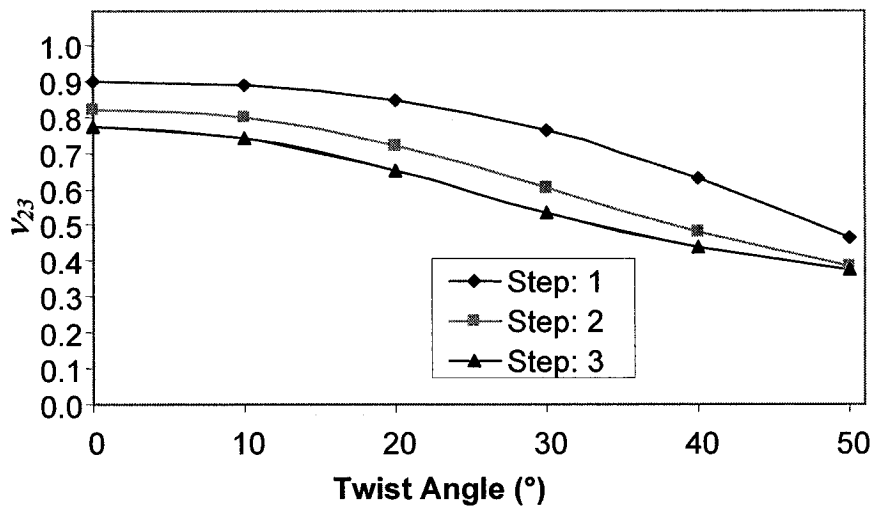

Figure 4.9 Transverse Poisson's ratio of a LaRC-SI/SWNT fiber as a function of twist angle.

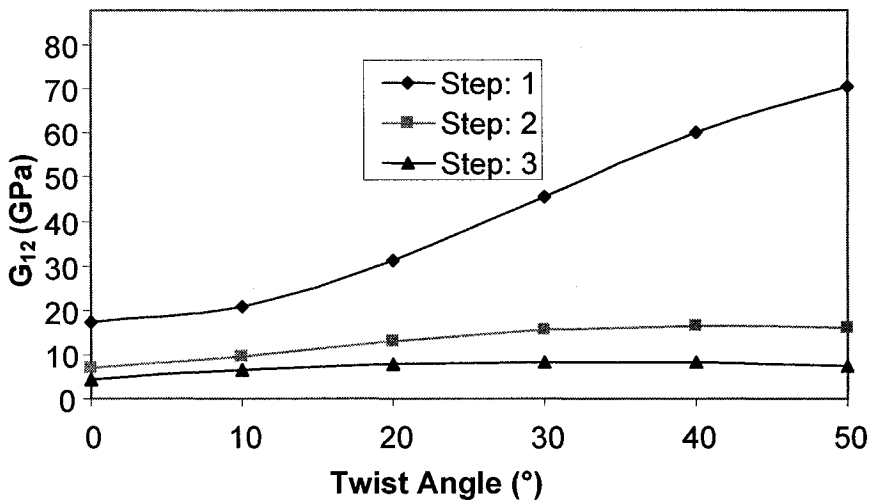

Figure 4.10 Axial shear modulus of a LaRC-SI/SWNT fiber as a function of twist angle.

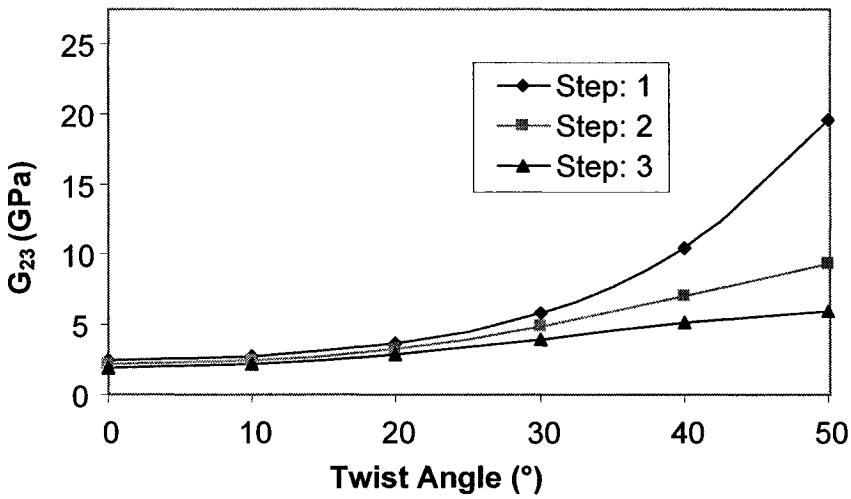

Figure 4.11 Transverse shear modulus of a LaRC-SI/SWNT fiber as a function of twist angle.

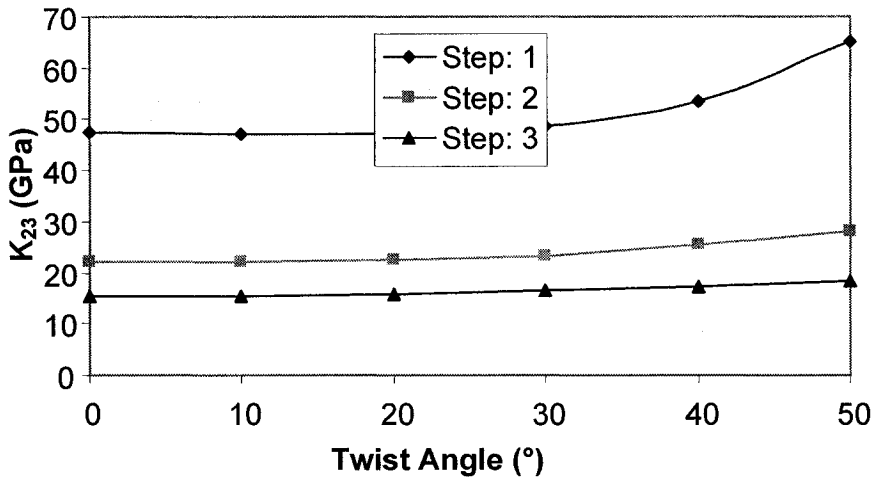

Figure 4.12 Transverse bulk modulus of a LaRC-SI/SWNT fiber as a function of twist angle.

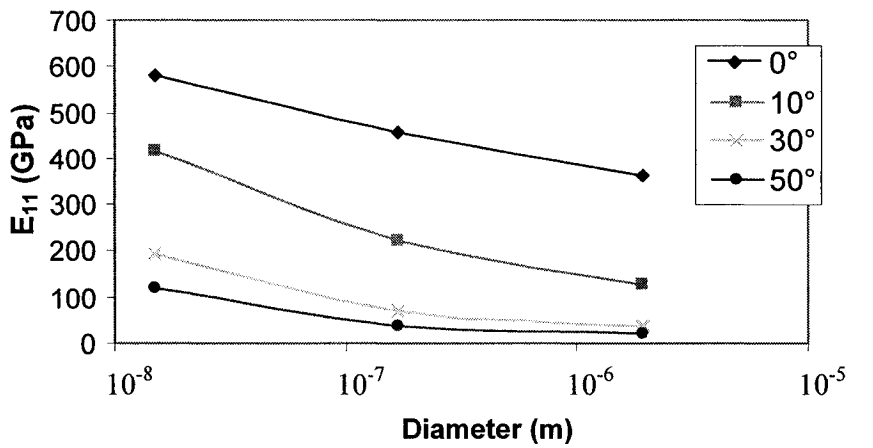

Figure 4.13 Scaling effect on the axial Young's modulus of LaRC-SI/SWNT fiber for different twist angles.

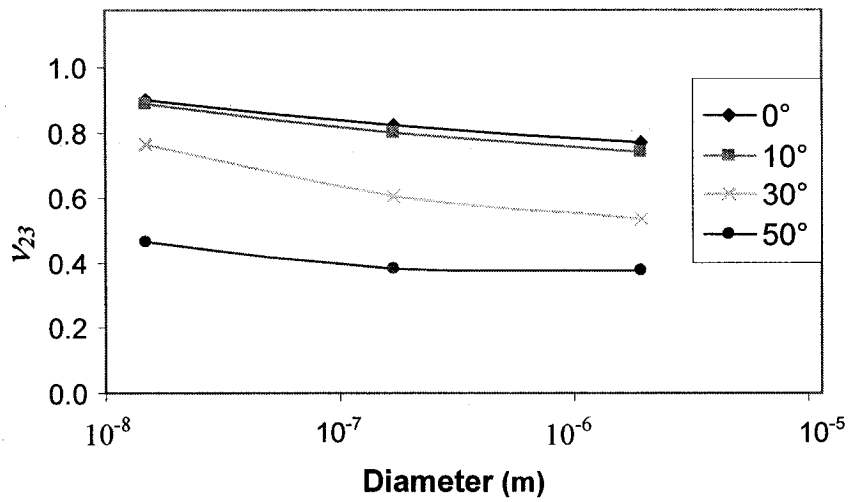

Figure 4.14 Scaling effect on the transverse Poisson's ratio of LaRC-SI/SWNT fiber for different twist angles.

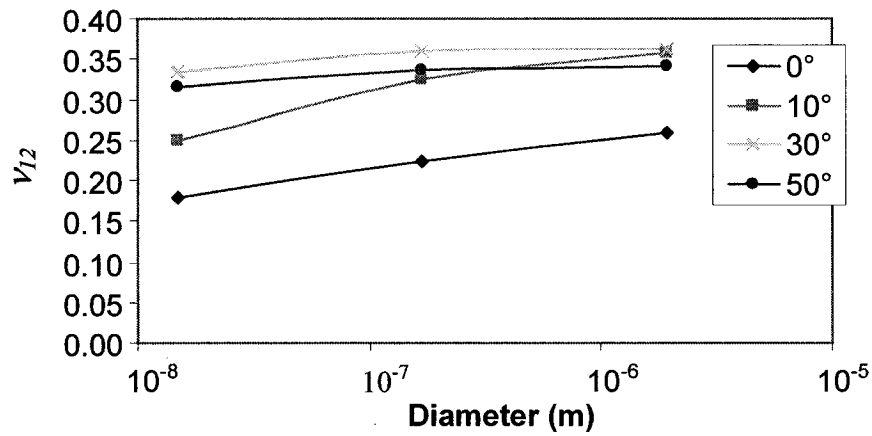

Figure 4.15 Scaling effect on the axial Poisson's ratio of LaRC-SI/SWNT fiber for different twist angles.

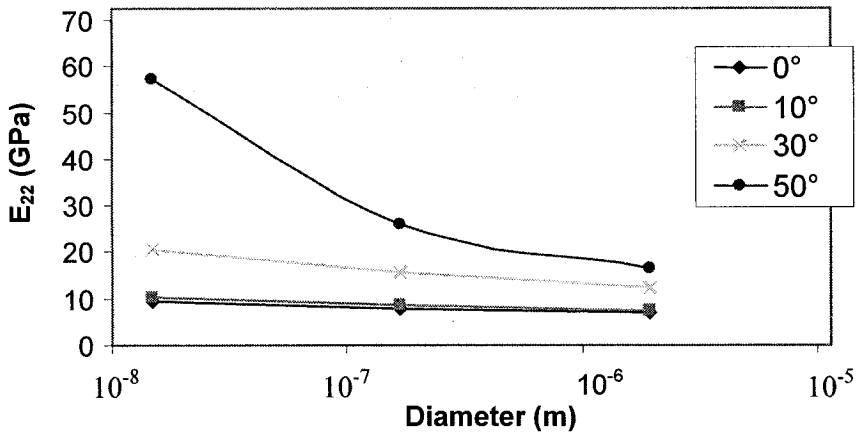

Figure 4.16 Scaling effect on the transverse Young's modulus of LaRC-SI/SWNT fiber for different twist angles.

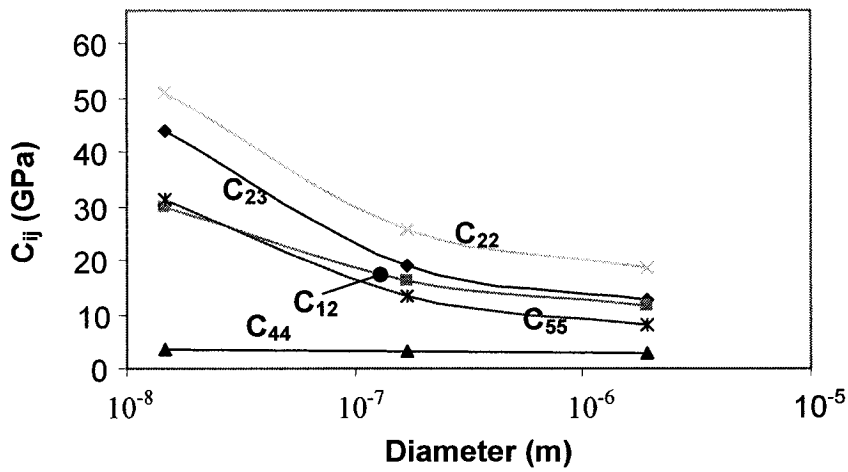

Figure 4.17 Effect of scaling on elastic constants of LaRC-SI/SWNT fiber with a twist angle of 20°.

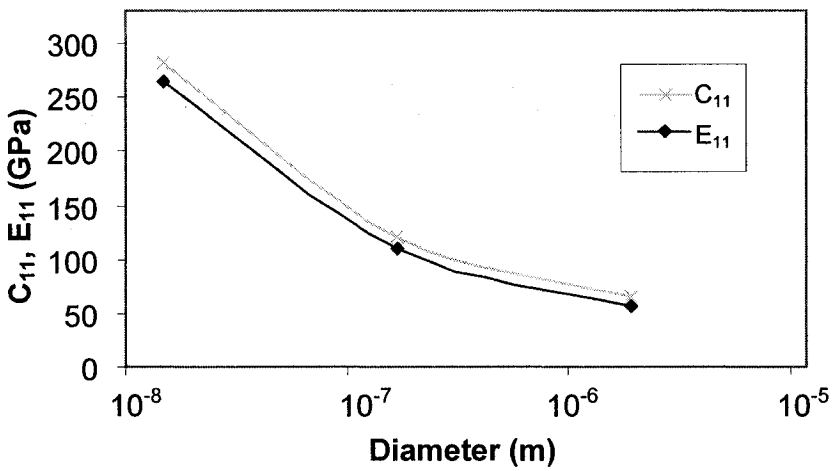

Figure 4.18 Scaling effect on both E_{11} and C_{11} of LaRC-SI/SWNT fiber with twist angle of 20°.

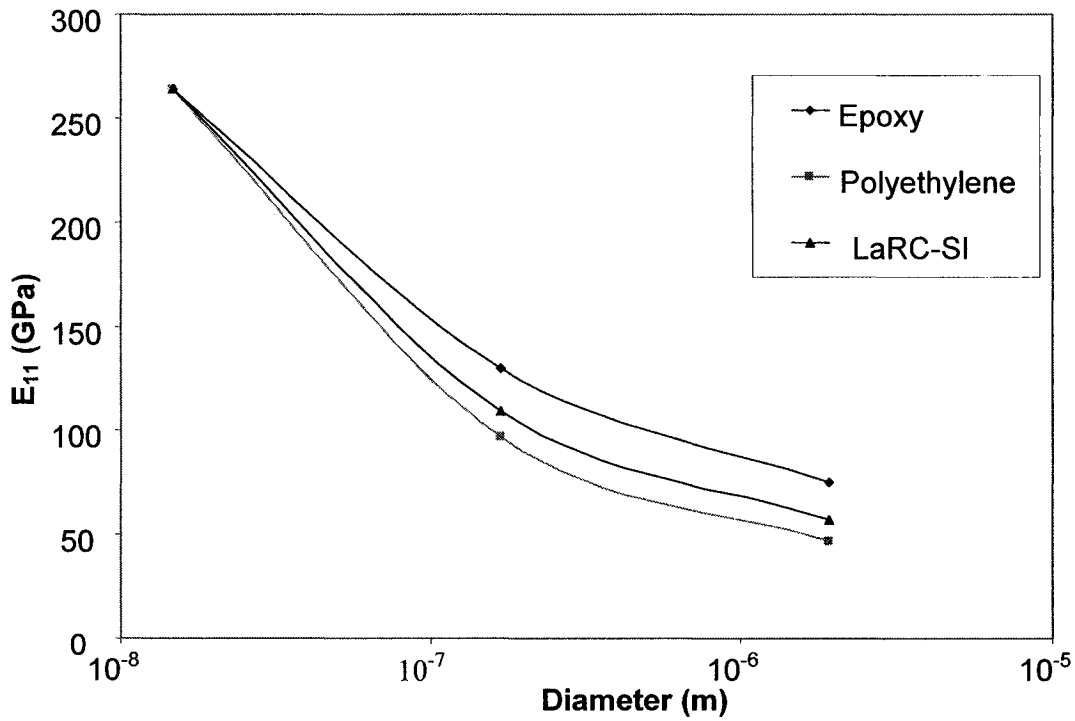

Figure 4.19 Effect of the different polymers on the axial Young's modulus.

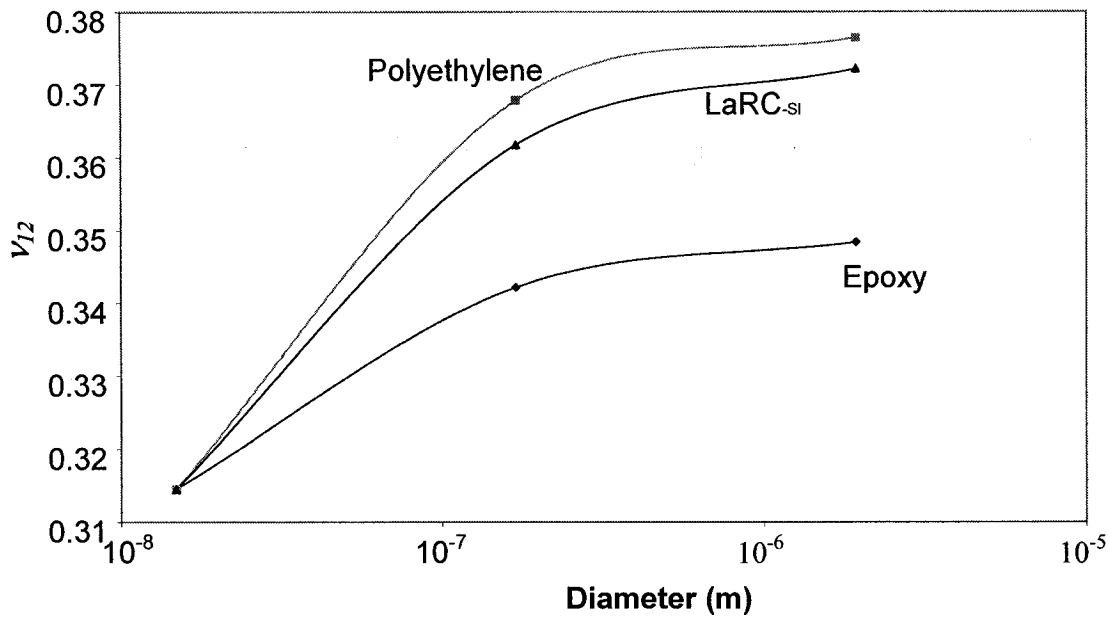

Figure 4.20 Effect of the different polymers on the axial Poisson's ratio.

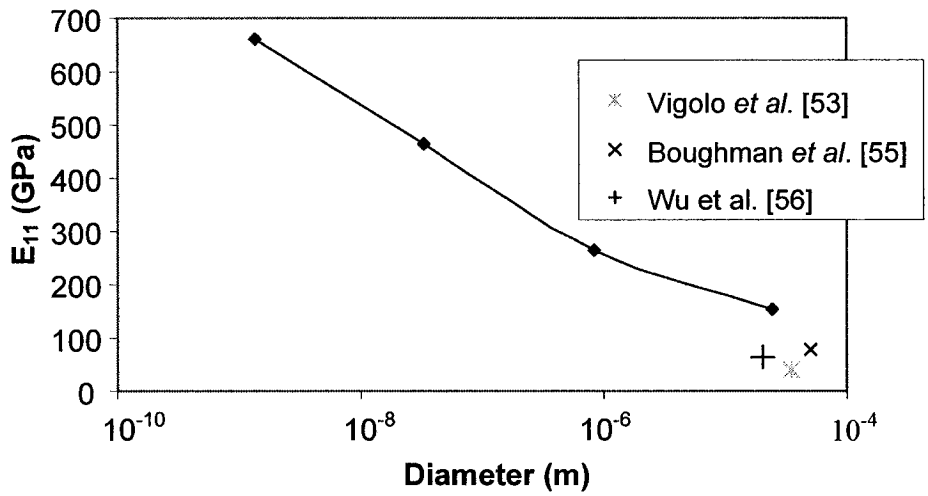

Figure 4.21 Comparison between E_{11} predicted by the self similar analysis and published data for nanotube/polymer fiber modulus.

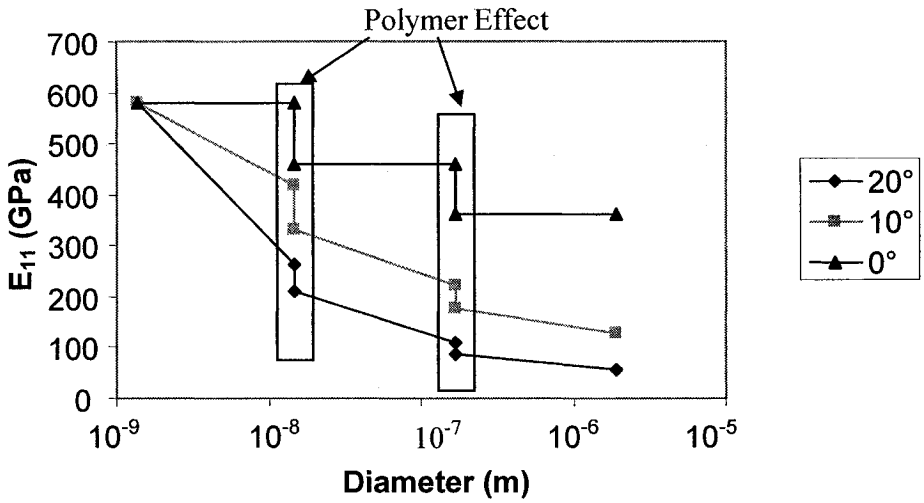

Figure 4.22 Effects of the polymer and the twist angle on the axial Young's modulus drop when scaling.

Chapter 5

Twisted SWNT/polymer Composite

In this chapter, the elastic properties of the polymer composites reinforced with twisted carbon nanotube fibers are determined by using traditional micromechanics (Mori-Tanaka method [69, 85]). Here, the effects of different parameters such as the degree of the alignment, the twist angle and the volume fraction of the fiber on the polymer composite properties are examined.

5.1 Micromechanics

In order to determine the elastic properties of the twisted carbon nanotube fiber/ polymer composite, the Mori-Tanaka method [69, 85] was used. This method has been successfully applied to transversely-isotropic inclusions by Qui and Weng [69,86]. With this method, the elastic stiffness tensor of the composite is given by [69]:

$$C = C^m + v_f \left\langle (C^f - C^m) A^f \right\rangle \left[(1 - v_f) I + v_f \left\langle A^f \right\rangle \right]^{-1} \tag{5.1}$$

where v_f is the fiber volume fraction, I is the identity tensor, C^m and C^f are the stiffness tensors of the matrix and the fiber, respectively, and A^f is the dilute mechanical strain concentration tensor for the fiber, given by:

$$A^f = \left[I + S(C^m)^{-1}(C^f - C^m) \right]^{-1} \tag{5.2}$$

where the tensor S is Eshelby's tensor given by Eshelby [87] and Mura [83]. In Equation 5.1, the terms enclosed brackets represent the average of the term over all orientations defined by the transformation from the local fiber coordinates to the global composite coordinate system. In this work, only two general cases were examined, perfectly random and perfectly aligned cases. However, the properties of the fiber with a specific amount of the alignment can be found using a statistical method [69]. For the case of unidirectionally aligned fibers, the orientation averaging in Equation 5.1 is not necessary, and the resulting elastic stiffness components of the composite have orthotropic

symmetry. For three-dimensional random fibers, the orientation average of tensor, A, is [88]:

$$\langle A_{ijmn} \rangle = \left(\kappa - \frac{2}{3}\mu \right)\left(\delta_{ij}\delta_{mn}\right) + \mu\left(\delta_{im}\delta_{jn} + \delta_{in}\delta_{jm}\right) \tag{5.3}$$

where $i, j, m, n = 1, 2, 3$; the indicial summation convention is used, and δ_{ij} is the Kronecker delta, and:

$$\kappa = \frac{1}{9} A_{iijj} \tag{5.4}$$

$$\mu = \frac{1}{10}\left(A_{ijij} - \frac{1}{3} A_{iijj} \right) \tag{5.5}$$

As can be seen from these equations, $\langle A \rangle$ is isotropic.

The Eshelby's tensor, S, depends on the form of the fiber and derivation details can be found in [83,87]. Table 5.1 gives the tensor S for an ellipsoid inclusion [84] used to model the fibers. In this Table, s is the fiber aspect ratio, and ν is the matrix Poisson's ratio, while I_1, Q, R, T, I_3 are given by:

$$I_1 = \frac{2s}{\sqrt{(1-s^2)^3}}\left[s\sqrt{s^2-1} - \cosh^{-1}(s) \right] \tag{5,6}$$

$$Q = \frac{3}{8(1-\nu)} \tag{5.7}$$

$$R = \frac{1-2\nu}{8(1-\nu)} \tag{5.8}$$

$$T = Q\frac{4-3I_1}{3(s^2-1)} \tag{5.9}$$

$$I_3 = 4 - 2I_1 \tag{5.10}$$

It is worth mentioning that the last column of Table 5.1 gives the S matrix for an infinite cylindrical fiber, and is determined by letting $s \rightarrow \infty$ for the ellipsoid fiber.

5.2 Results

Here, the results for the composite made of the LaRC-SI polymer and the twisted SWNT arrays are given for the two general cases (completely random and completely aligned). The method to obtain the elastic properties of the SWNT arrays is given in Chapter 3. Figure 5.1 shows the effect of the aspect ratio of twisted carbon nanotube fibers with a volume fraction of 1% on Young's modulus for two different twist angles of 0° and 10°. As can be seen here for the aligned case (zero twist angle), very short fibers (aspect ratios<25) have considerably lower modulus. Moreover, it seems clear that composites made of SWNT arrays with a twist angle of 0° have a Young's modulus 20% higher compared to arrays with a twist angle of 10°. Also, for a twist angle of 0°, an aspect ratio of 200 is required to reach the point where further increase in the aspect ratio does not significantly change the Young's modulus. An aspect ratio of 100 is sufficient for the case with a twist angle of 10°. For the random case, the effect of the aspect ratio is negligible with the aspect ratio of 50 and higher. In summary, even for a small volume fraction of SWNT (1%) the modulus of the random case is almost half of the aligned case for both twist angles. These results show the importance of the alignment of the carbon nanotube fibers in the polymer.

Table 5.2 gives elastic constants of the composite made of the aligned and random SWNT fibers. For the aligned case, while E_{11} increases with aspect ratio, G_{11}, G_{23} and υ_{12} remain almost constants. On the other hand, for the random case (isotropic composite), all three constants are weakly dependent to the aspect ratio of the fiber. For instance, a 5% increase of the fiber shear modulus is observed when the aspect ratio changes from 25 to ∞. This proves that for the random case, the length of the carbon nanotube array is not very important compared to the aligned case.

Figure 5.2 shows the effect of volume fraction on the axial Young's modulus of the composite reinforced by the aligned SWNT fiber with twist angles of 0° and 10° for two different aspect ratios (12 and 600). As can be seen here, in all cases, the moduli are a

linear function of the nanotube array volume fraction. For an aspect ratio of 12, both 0° and 10° fibers follow the same trend which proves that for low aspect ratios the twist angle does not have significant effect on the properties of the composites. On the other hand, for high aspect ratio E_{11} for the twist angle of 0° is about 20% higher compared to a twist angel of 10°. However, it is again worth mentioning that the value of the E_{11} for a twist angle of 0° could drop dramatically as a result of poor load transfer between the adjacent tubes.

Figure 5.3 shows the shear moduli (G_{12} and G_{23}) of the aligned case for SWNT array/LaRC-SI composite with a twist angle of 10° versus the volume fraction where the array aspect ratio of 600. As expected, the transverse shear modulus (G_{23}) remains almost constant for specified range of volume fractions (from 1.36 GPa for a volume fraction of 0% to 1.54 GPa for a volume fraction of 20%). This is because the aligned fibers cannot dramatically change the properties of the composite in the perpendicular direction. However, the axial shear modulus (G_{12}) increases with the volume fraction. This is due to the fact that the fibers can bear load against the axial shearing (a 40% increase of the G_{12} was observed for a volume fraction of 20%). Moreover, the effect of the volume fraction on the shear modulus of random SWNT array/LaRC-SI composite for two different twist angles (0° and 10°) were examined (Figure 5.3). A four-fold increase for a twist angle of 10° and a five-fold increase for a twist angle of 0° were observed with a volume fraction of 20%. These increases are significantly higher than the aligned case because of the isotropic behavior of the random case. Figure 5.4 shows the Poisson's ratio for the aligned and random cases versus the SWNT volume fraction for two different aspect ratios. While υ_{12} with an aspect ratio of 12 and υ of random cases moderately decreases linearly with the volume fraction, υ_{12} with an aspect ratio of 600 decreases considerably particularly at smaller volume fractions (<10%).

In Figures 5.5 and 5.6, the current model of a SWNT array/LaRC-SI composite with a twist angle of 0° (parallel SWNT array) was compared with the constitutive model of individual nanotube-reinforced polymer composite of Odegard *et al.* [69] (Section 2.8.2). In Figure 5.5, the effect of aspect ratio on the Young's modulus of the composite of both aligned and random dispersion of 1% of SWNT is shown. The constitutive model

predicts higher modulus when compared to present model. This difference comes from the fact that the properties of the SWNT arrays used in the present model are lower than the properties of the individual SWNT used by Odegard *et al.* (i.e. while the axial Young's modulus of the SWNT array is 514 GPa, that of individual SWNT is about 850 GPa). Figure 5.6 shows the effect of the volume fraction of SWNT on the Young's modulus of both models for both aligned and random cases. Similarly, the constitutive model predicts higher modulus for a specific volume fraction.

Here, as mentioned previously [89], it becomes possible to produce SWNT fibers with infinite length by applying a twist angle to the SWNT array. Therefore, in Figure 5.7 two models are compared by assuming that the current model consists of infinite SWNT arrays with a twist angle of 10° while the other model consists of individual SWNT with an aspect ratio of 65 as a practical value. As can be seen here, the constitutive model of Odegard *et al.* [69] predicts higher Young's modulus comparing to the current model (i.e. for a volume fraction of 7% their model is about 33% percent higher than the current model). This again can be explained by using the individual SWNT instead of the SWNT array. Moreover, as previously seen, even small twist angle significantly drops the modulus of the array.

5.3 Conclusion

As explained before, the composites reinforced with aligned SWNT arrays (zero twist angle) need higher aspect ratio to reach to the stable value of Young's modulus. Moreover, the composite reinforced by the aligned SWNT array shows higher modulus compared to the composite made of SWNT arrays with a twist angle of 10°. However, it is clear that in order to have perfect load transfer between the perfectly aligned tubes (zero twist angle), a length of at least 10,000 nm is necessary [32]; therefore, it can be predicted that the modulus of the composite made of fiber with a twist angle of 0° is lower than the predicted result shown in Figure 5.1. From Figure 5.1 it was shown that the alignment of the fiber can significantly increase the modulus of the composite. Also, for random SWNT array dispersion in the composite, it was shown that the length of the carbon nanotube array does not have a significant effect on the elastic properties of the

fiber. Moreover, it was shown that higher aspect ratio can cause higher drop in Poisson's ratio of the composite comparing the lower one. By comparing the current model and the constitutive model done by Odegard *et al.*, it was shown that the former predicts higher modulus for the composite because of the higher elastic properties of SWNT compared to SWNT arrays. However, an important advantage of the current approach is the possibility of making infinite SWNT arrays due to the twist angle that provide additional load transfer and enable the assembly of discontinuous nanotubes. In summary, although the twist angle of 10° significantly reduces the Young's modulus of the array, from Figure 5.7 it was observed that these two models are still comparable due to the infinite length of the fiber of the current model. In practice, dispersing the individual carbon nanotubes into a polymer and aligning them are very difficult and is a huge obstacle in production of the carbon nanotube/polymer composite. However, in the current model the twisted SWNT arrays are at least one order of magnitude larger in diameter compared to SWNT. Therefore, it is predicted that the process of dispersing of the SWNT arrays and specially aligning them could be more practical.

Table 5.1

Eshelby's constants for ellipsoid and infinite cylindrical inclusions [84].

	Ellipsoid inclusion	**Infinite cylinder inclusion**
S_{11}	$\frac{4Q}{3} + RI_3 + 2s^2T$	0
$S_{22} = S_{33}$	$Q + RI_1 + \frac{3T}{4}$	$\frac{5-\nu}{8(1-\nu)}$
$S_{23} = S_{32}$	$\frac{Q}{3} - RI_1 + \frac{4T}{3}$	$\frac{-1+4\nu}{8(1-\nu)}$
$S_{21} = S_{31}$	$-RI_1 - s^2T$	$\frac{\nu}{2(1-\nu)}$
$S_{12} = S_{13}$	$-RI_3 - T$	0
S_{44}	$\frac{Q}{3} + RI_1 + \frac{T}{4}$	$\frac{3-4\nu}{2(1-\nu)}$
$S_{55} = S_{66}$	$2R - \frac{RI_1}{2} - \frac{1+s^2}{2}T$	$\frac{1}{4}$
For other S_{ij}	0	0

Table 5.2

Effect of the aspect ratio on the composite properties for a SWNT volume fraction of 1% and a twist angle of 10°.

SWNT Array Aspect Ratio	**Aligned Case**				**Random Case**		
	G_{23}	**G_{12}**	**υ_{12}**	**E_{11}**	**E**	**G**	**υ**
∞	1.369	1.403	0.395	7.93	4.52	1.631	0.387
250	1.369	1.403	0.395	7.84	4.51	1.625	0.387
200	1.369	1.403	0.395	7.79	4.50	1.622	0.387
150	1.369	1.403	0.395	7.71	4.48	1.616	0.387
100	1.369	1.403	0.396	7.50	4.45	1.602	0.388
50	1.369	1.403	0.396	6.78	4.32	1.553	0.390

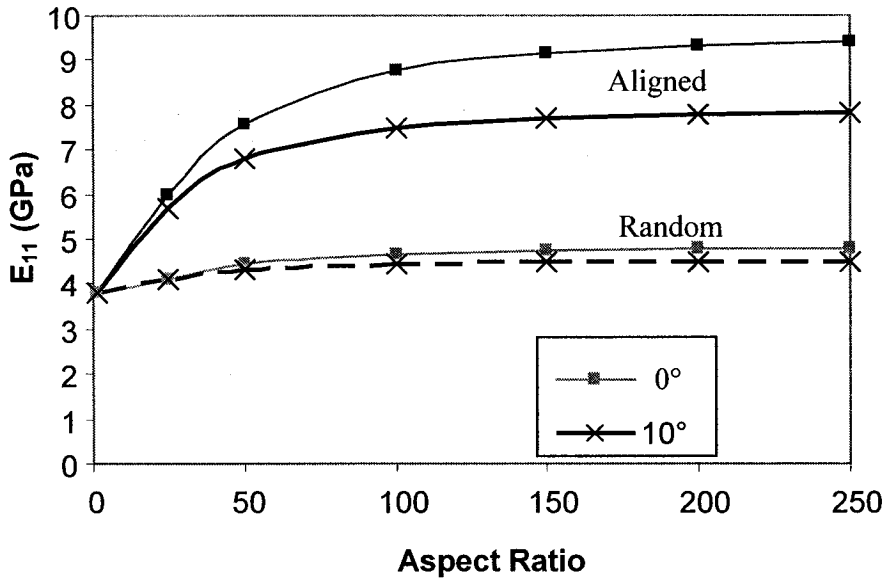

Figure 5.1 Young's modulus of a 1 % SWNT array/LaRC-SI composite for both aligned and random dispersed SWNT array versus the array aspect ratio for twist angles of 0° and 10°.

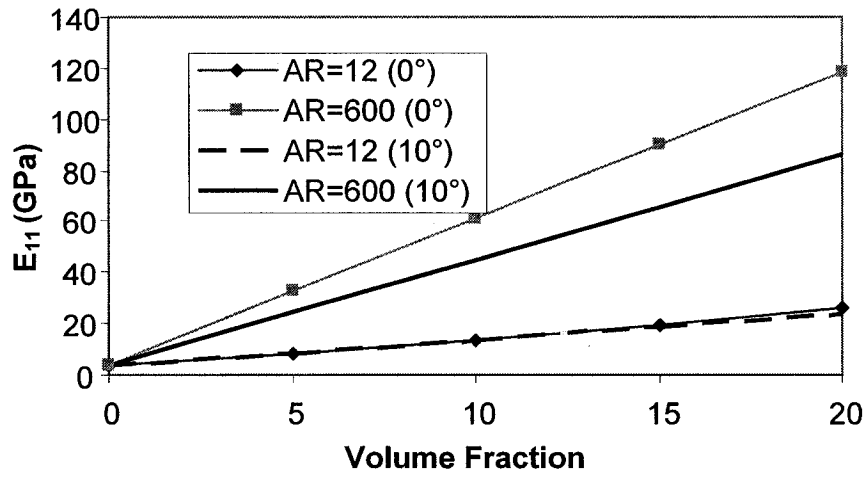

Figure 5.2 Axial Young's modulus of SWNT array/LaRC-SI composite versus the SWNT volume fraction for twist angles of 0° and 10°.

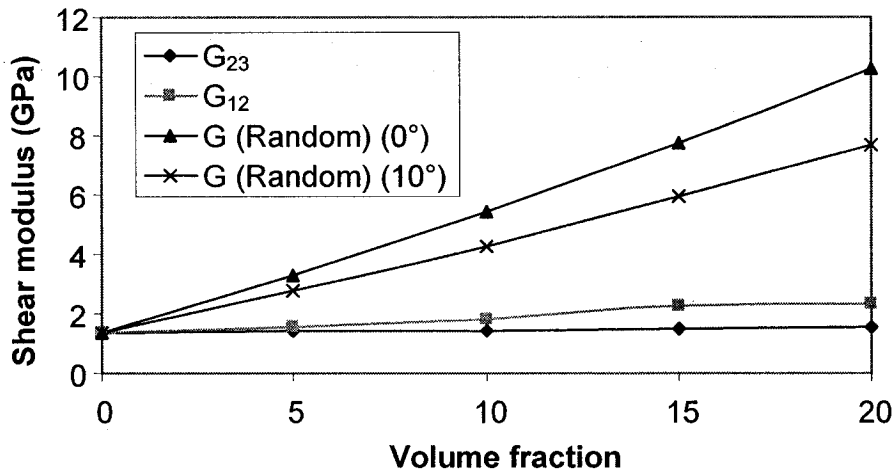

Figure 5.3 Shear modulus of SWNT array/LaRC-SI composite for both aligned and random dispersed array SWNT versus the SWNT volume fraction for twist angles of 0° and 10°.

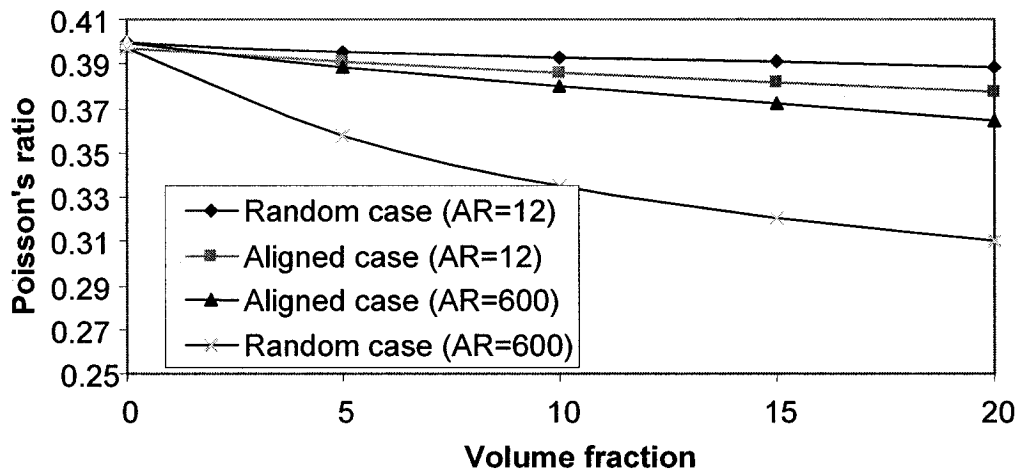

Figure 5.4 Poisson's ratio of SWNT array/LaRC-SI composite for both aligned and random dispersed SWNT array versus the SWNT volume fraction for a twist angle of 10°.

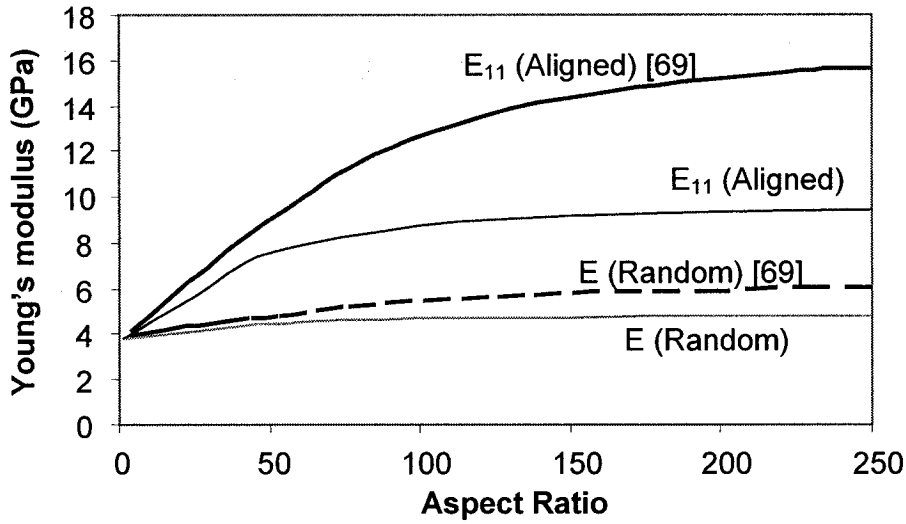

Figure 5.5 Young's modulus of SWNT array/LaRC-SI composite as a function of the aspect ratio for both aligned and random dispersed SWNT arrays with 0° twist angle and the SWNT volume fraction of 1% and the comparison between this model and the constitutive model of Odegard *et al.* [69].

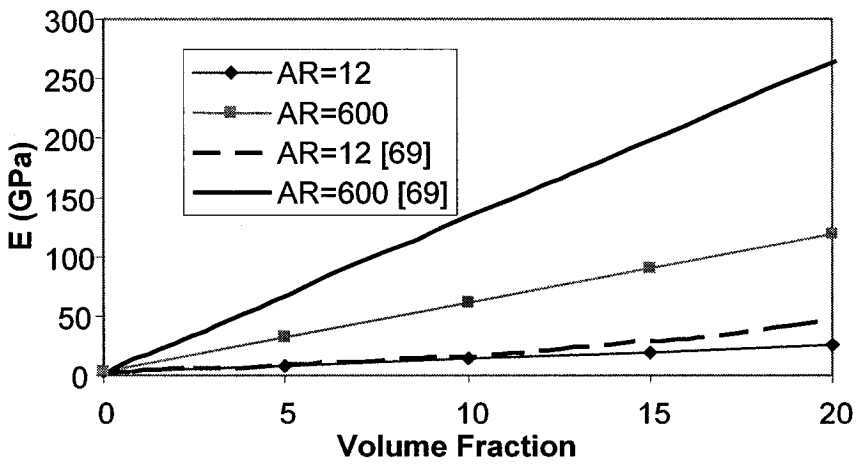

Figure 5.6 Axial Young's modulus of SWNT/LaRC-SI composite versus the SWNT volume fraction of both aligned and random SWNT arrays with 0° twist angle and the comparison between this model and the constitutive model of Odegard *et al.* [69].

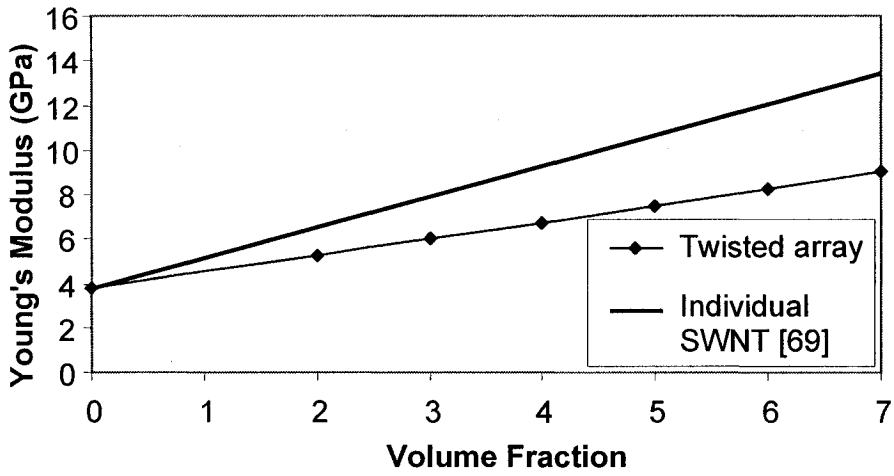

Figure 5.7 Comparison between nanotube-reinforced composite model [69] and the current model.

Chapter 6

Conclusion

This work tried to investigate the elastic properties of carbon nanotube/polymer composites. In Chapter 3, a helical carbon nanotube fiber was modeled by using the finite element method. This model was compared with anisotropic elasticity presented in Section 2.8.1. These two models showed very good agreement. It was shown that strain energy was a very powerful method for computing the elastic constants of the model. Since the model is transversely isotropic, five sets of boundary conditions are enough to obtain the material stiffness moduli. It was also shown that the energy method was more accurate compared to the elasticity method, where it was supposed that $\sigma_{r\theta} = 0$. Since each layer had a different twist angle, the layers tendency to slip from each other would induce a non-zero $\sigma_{r\theta}$ (Figure 2.41). Also, the results illustrate that the Young's modulus of carbon nanotube fibers decreases dramatically even for small twist angles (less than *20°*) without any contribution to the transverse properties as transverse properties remain constants for twist angles between *0°* to *15°*.

In Chapter 4, it was shown that even for small twist angles (<20°) the axial Young's modulus of a nanotube micro-fiber dropped dramatically. Therefore, in order to maintain high stiffness of SWNT arrays, the nanotube alignment of the fiber is essential. However, as mentioned before, this alignment has a negative effect on the load transfer efficiency between the tubes. While the entire drop in properties of the fiber with a twist angle of zero is caused by polymer addition, only 15 % of the modulus drop with a twist angle of 20° is due to the polymer addition while the other 85% is caused by the twist angle. It was also shown that the transverse properties of the micro-fiber remain constant for twist angles less than 15°. Finally, it was shown that the polymer properties can have an important effect on the elastic properties of the SWNT/polymer fiber.

In Chapter 5, it was illustrated that the composites reinforced with aligned SWNT arrays (zero twist angle) need higher aspect ratio to reach to a constant value for the Young's modulus. Moreover, composites reinforced by the aligned SWNT arrays have higher

elastic modulus compared to composites made of SWNT arrays with a twist angle of 10°. However, in order to have perfect load transfer between the perfectly aligned tubes (zero twist angle), a length of at least 10,000 nm was necessary [21]; therefore, it is expected that the modulus of composites made of SWNT arrays with a twist angle of 0° is lower than the predicted result obtained from conventional micromechanics. Also, for random SWNT array dispersions in the polymer, it was shown that the nanotube array length does not have a significant effect on the composite elastic properties. Moreover, by comparing the current model and the constitutive model done by Odegard et al., the latter predicted higher modulus for the composite because of higher elastic properties of individual SWNT compared to SWNT array. However, an important advantage of using twisted array of SWNT instead of individual SWNT was the possibility of making infinite SWNT arrays because of higher load transfer between tubes as a result of the twist angle. In summary, although the twist angle of 10° significantly reduced the array Young's modulus, it was observed that these two models were still comparable due to the infinite length of the fiber of the current model.

In summary, the effect of the twist angle on the carbon nanotube/polymer fiber was examined. It became clear that small twist angles (<20°) significantly reduced the axial modulus. Moreover, spanning three orders of magnitude from SWNT to SWNT/polymer fiber resulted in a significant drop of the properties depending on the volume fraction of the polymer and twist angle of the fiber.

It is worth mentioning that while a ideal interaction or load transfer between the tubes and the polymer molecules was assumed in this work, further work similar to the work done by Odegard et al [67] is necessary to completely model this interaction. Another area open to further studies is the investigation of the effect of twist angle on the load transfer between tubes. While a preliminary model done by Qian [65] shows a significant increase on load transfer, more accurate models are necessary to obtain the optimum twist angle.

References

[1] Koch C. C, 'Nanostructured materials: processing, properties and potential applications'; Noyes Publication (2002).

[2] Liz-marzan L. M, Kamat P. V, 'Nanoscale Materials'; Kluwer Academic Publishers (2003).

[3] Poulin P, Vigolo B, Launois P, 'Films and fibers of oriented single wall nanotubes',

Carbon, 40, 1741–9 (2002).

[4] Vigolo B, Poulin P, Lucas M, Launois P, Penicaud A, Bernier P, 'Improved structure and properties of single-walled carbon nanotube spun fibers'; Applied Physics Letters, 81, 1210-12 (2002).

[5] Vigolo B, Penicaud A, Coulon C, Sauder C, Pailler R, Journet C, Bernier P, Poulin P, 'Macroscopic fibers and ribbons of oriented carbon nanotubes'; Science; 290, 1331-4 (2000).

[6] Zhu H. W, Xu C. L, Wu D. H, Wei B. Q, Vajtai R, Ajayan P. M, 'Direct synthesis of long single-walled carbon nanotube strands'; Science, 296, 884-6 (2002).

[7] Dalton B. A, Collins S, Munoz E, Razal M. J, Von Howard E, Ferraris P. J, Coleman N. J, Kim G. B, Baughman H. R, 'Super-tough carbon-nanotube fibers'; Nature, 423, 703 (2003).

[8] Andrews R, Jacques D, Minot M, Rantell T, 'Fabrication of carbon multiwall nanotube/polymer composites by shear mixing'; Macromolecular Material Engineering, 287, 395–403 (2002).

[9] Sandler J, Werner P, Shaffer M.S.P, Demchuk V, Altsta V, Windle A. H, 'Carbon-nanofibre-reinforced poly (ether ether ketone) composites'; Composites: Part A, 33 1033–9 (2002).

[10] Kearns J. C, Shambaugh R. L, 'Polypropylene fibers reinforced with carbon nanotubes'; J. Applied Polymer Science, 86, 2079–84 (2002).

[11] Coleman J. N, Blau W. J, Dalton A. B, Munoz E, Collins S, Kim B. G, Razal J, Selvidge M, Vieiro G, Baughman R. H, 'Improving the mechanical properties of single-walled carbon nanotube sheets by intercalation of polymeric adhesives'; Applied physics letters, 82, 1682-4 (2003).

[12] Kroto H. W, Heath J. R, O'Brien S. C, Curl R.F, Smalley R.E, 'C_{60}: buckminsterfullerene'; Nature, 318, 162 (1985).

[13] Krastschmer W, Lamb L. D, Fostiropoulos K, Huffman D.R, 'Solid C_{60}: a new form of carbon'; Nature, 347,354 (1990).

[14] Iijima S, 'Helical Microtubules of graphitic carbon', Nature, 354, 56 (1991).

[15] Iijima S, Ichihashi T, 'Single-shell carbon nanotubes of 1-nm diameter'; Nature, 363, 603 (1993).

[16] Bethune D. S, Kiang C. H, de Vries M. S, Gorman G, Savoy R, Vasquez J, Beyers R, 'Cobalt-catalyzed growth of carbon nanotube with single-atomic-layer walls'; Nature, 363, 605 (1993).

[17] Harris P, 'Carbon Nanotubes and Related Structures', Cambridge University Press (1999).

[18] Renzik D, Oik C. H, Neumann D.A, and Copley R. D, 'X-ray power diffraction from carbon nanotubes and nanoparticles'; Physical Review B, 52, 116 (1995).

[19] Saito R, Fujita M, Dresselhaus G, Dresselhaus M. S, 'Electronic structure of chiral graphene tubules'; Applied Physics Letters, 60 (18) (1992).

[20] Thastenson E.T, Ren Z, Chou T.W, 'Advances in the science and technology of carbon nanotubes and their composites: a review'; Composite Science and Technology, 61, 1899-1912 (2001).

[21] Ruland W, Schaper A. K, Hou H, Greiner A, 'Multi-wall carbon nanotube with uniform Chirality: evidence for scroll structures'; Carbon 41, 423 (2003)..

[22] Zhang X. F, Zhang X. B, Tendeloo G.V, Amelinckx S, Beeck M, Landuyt J, 'Carbon nano-tube; their formation process and observation by electron microscopy'; Journal of Crystal Growth, 130, 368 (1993).

[23] Pipes B.R, Frankland S.J.V, Hubert P, Saether E, 'Self-consistent properties of carbon nanotubes and hexagonal arrays as composite reinforcements'; Composites Science and Technology , 63(10), 1349-58 (2003).

[24] Popov V. N, Van Doren V. E, Balkanski M, 'Elastic properties of crystals of carbon nanotubes'; Solid State Communications; 114, 395–9 (2000).

[25] Cornwell C. F, Wille L. T, 'Elastic properties of single-walled nanotubes in compression'; Solid State communications, 101(8), 555–8 (1997).

[26] Popov V. N, Van Doren V. E, 'Elastic properties of single-walled carbon nanotubes'; Physical Review B, 61 (4), 3078–84 (2000).

[27] Lourie O, Wagner H. D, 'Evaluation of young's modulus of carbon nanotubes by micro-raman spectroscopy'; Journal of Material Resources, 13(9), 2418–22 (1998).

[28] Yu MF, Files BS, Arepalli S, and Ruoff RS, Tensile loading of ropes of single wall carbon nanotubes and their mechanical properties, Physical Review Letters, 84(24) 5552–5 (2000).

[29] Yu M. F, Lourie O, Dyer M. J, Moloni K, Kelly T. F, and Ruoff R. S, 'Strength and breaking mechanism of multiwalled carbon nanotubes under tensile load'; Science, 287 (5453), 637–40 (2000).

[30] Robertson D. H, Brenner D. W, and Mintmire J. W, 'Energetics of nanoscale graphitic tubules'; Physical Review B, 45 (21), 12592–5 (1992).

[31] Lu J. P, 'Elastic properties of carbon nanotubes and nanoropes'; Physical Review Letters, 79(7), 1297–300 (1997).

[32] Qian D, Wagner G. J, Liu W. K, Yu M, Ruoff R. S, 'Mechanics of carbon nanotube'; Applied Mechanics Review, 55 (6), 495-533 (2002).

[33] Yakobson BI and Smalley RE, 'Fullerene nanotubes: C-1000000 and beyond'; American Scientist, 85 (4), 324–37 (1997).

[34] Treacy M. M. J, Ebbesen T. W, and Gibson J. M, 'Exceptionally high young's modulus observed for individual carbon nanotubes'; Nature, 381 (6584), 678–80 (1996).

[35] Poncharal P, Wang Z. L, Ugarte D, de Heer W.A, 'Electrostatic deflections and electromechanical resonances of carbon nanotubes'; Science 283 (5407), 1513–6 (1999).

[36] Yu M. F, Dyer M. J, Chen J, Bray K, 'Multiprobe nanomanipulation and functional assembly of nanomaterials inside a scanning electron microscope'; International Conf IEEE-NANO2001 (eds), Maui (2001).

[37] Shen W. D, Jiang B, Han B. S, and Xie S. S, 'Investigation of the radial compression of carbon nanotubes with a scanning probe microscope'; Physical Review Letters, 84 (16), 3634–7 (2000).

[38] Chesnokov S. A, Nalimova V. A, Rinzler A. G, Smalley R. E, and Fischer J. E, 'Mechanical energy storage in carbon nanotube springs'; Physical Review Letters 82 (2), 343–6 (1999).

[39] Yakobson B. I, Brabec C. J, and Bernholc J, 'Nanomechanics of carbon tubes: Instabilities beyond linear response'; Physical Review Letters, 76 (14), 2511–4 (1996).

[40] Lourie O, Cox D. M, and Wagner H. D, 'Buckling and collapse of embedded carbon nanotubes'; Physical Review Letters, 81 (8), 1638–41 (1998).

[41] Hubert P., Pipes R. B, 'Self-Consistent Properties of the MWCN and Hexagonal Arrays as Composite Reinforcements'; The 14th International Conference on Composite Materials (ICCM-14), San Diego, CA, July (2003).

[42] Yu M. F, Lourie O, Dyer M. J, Moloni K, Kelly T. F, and Ruoff R. S (1998), 'Strength and breaking mechanism of multiwalled carbon nanotubes under tensile load'; Science 287 (5453), 637–40 (1998).

[43] Wagner H. D, Lourie O, Feldman Y, and Tenne R, 'Stress induced fragmentation of multiwall carbon nanotubes in a polymer matrix'; Applied Physics Letters, 72 (2), 188–90 (1998).

[44] Lourie O, Cox D. M, and Wagner H. D, 'Buckling and collapse of embedded carbon nanotubes'; Physical Review Letters, 81 (8), 1638–41 (1998).

[45] Yakobson B. I, Brabec C. J, and Bernholc J, 'Nanomechanics of carbon tubes: Instabilities beyond linear response'; Physical Review Letters 76 (14), 2511–4 (1996).

[46] Yakobson B. I, Avouris P, 'Mechanical properties of carbon nanotubes'; Carbon Nanotubes 287–327 (2001).

[47] Yakobson B. I, Campbell M. P, Brabec C. J, and Bernholc J, 'High strain rate fracture and c-chain unraveling in carbon nanotubes'; Computational Material Science. 8 (4), 341–8 (1997).

[48] Yu M. F, Yakobson B. I, and Ruoff R. S, 'Controlled sliding and pullout of nested shells in individual multiwalled carbon nanotubes'; Journal of .Physical Chemistry B, 104 (37), 8764–7 (2000).

[49] Peter J. F. Harris, 'Carbon Nanotubes and Related Structures, New Materials for the Twenty-first Century'; Cambridge University Press, 1999.

[50] Saito Y, Nishikubo K, Kawabata K, Matsumoto T, 'Carbon nanocapsules and single-layered nanotubes produced with platinum-group metals'; J. Applied Physics, 80, 3062 (1996).

[51] Guo T, Nikolaev P, Rinzler A. G, Tomanek D, Colbert D. T, Smalley R. E, 'Self-Assembly of Tubular Fullerenes', J. Physical Chemistry, 99, 10694 (1995).

[52] Edno M, Tsakeuchi K, Igarashi S, Kobori K, Shiraishi M, Kroto H. W, 'The Production and Structure of Pyrolytic Carbon Nanotubes PCNT's'; Physical Chemical Solids, 54, 1841 (1993).

[53] Endo M., Takeuchi K, Kobori K, Takahashi K, Kroto H. W, Sarkar A, 'Pyrolytic carbon nanotubes from vapor-grown carbon fibers'; Carbon, 33, 873 (1995).

[54] Ge M, Satter K, 'Vapor-condensation generation and STM analysis of fullerene tubes'; Science, 260, 515 (1993).

[55] Nikolaev P, Bronikowski M. J, Bradley R. K, Fohmund F, Colbert D. T, Smith K. A, 'Gas-phase catalytic growth of singe walled carbon nanotubes from carbon monoxide'; Chemical Physical Letters, 313, 91-7 (1995).

[56] Ge M, Sattler K, 'Bundles of carbon nanotubes generated by vapor-phase growth'; Applied Physics Letters; 64(6), 710–1 (1994).

[57] Che G, Lakshmi B. B, Martin C. R, Fisher E. R, Ruo. R. S, 'Chemical vapor deposition based synthesis of carbon nanotubes and nanofibers using a template method'; Chemistry of Materials, 10 (1), 260–7 (1998).

[58] Li W. Z, Xie S. S, Qian L. X, Chang B. H, Zou B. S, Zho W. Y, 'Large-scale synthesis of aligned carbon nanotubes'; Science; 274, 1701–3 (1996).

[59] Zhang X. X, Li Z. Q, Wen G. H, Fung K. K, Chen J, Li Y, 'Microstructure and growth of bamboo-shaped carbon nanotubes'; Chemical Physics Letters, 333(6): 509–14, (2001).

[60] Ren Z. F, Huang Z. P, Xu J. W, Wang J. H, Bush P, Siegal M. P, 'Synthesis of large arrays of well-aligned carbon nanotubes on glass', Science, 282, 105–7 (1999).

[61] Pipes R. B, Hubert P, 'Helical carbon nanotube arrays: mechanical properties'; Composite Science and Technology, 62, 419-28 (2002).

[62] Haile J. M, 'Molecular Dynamics Simulation', Wiley Interscience (1992).

[63] Dresselhaus M. S, Dresselhaus G, Saito R, 'Physics of carbon nanotubes'; Carbon; 33 (7), 883–91 (1995).

[64] Thess A, Lee R, Nikolaev P, Dai H, Petit R. J, Robert J, 'Crystalline ropes of metallic carbon nanotubes'; Science, 273, 483–7 (1996).

[65] Yao N and Lordi V, 'Young's modulus of single-walled carbon nanotubes'; J. Applied Physics, 84 (4), 1939–43 (1998).

[66] Thostenson E. T, Chou T, 'Aligned multi-walled carbon nanotube-reinforced composites: processing and mechanical characterization'; J. Applied Physics D, 35, L77–L80, (2002).

[67] Qian D, Liu W. K, Ruoff R. S, 'Load transfer mechanism in carbon nanotube ropes', Composite Science and Technology, 63, 1561-9 (2003).

[68] Hearle J. W. S, Grosberg P, Backer S, 'Structural mechanics of fibers, yarns, and fabrics'; volume 1, New York: John Wiley & Sons (1969).

[69] Odegard G. M, Gates T. S, Wise K. E, Park C, Siochi E. J, 'Constitutive modeling of nanotube-reinforced polymer composites'; Composite Science and Technology 63, 1671-87 (2003).

[70] Thostenson E. T, Chou T. W, 'On the elastic properties of carbon nanotube-based composites: modeling and characterization'; J. Applied Physics D, 36, 573-82 (2003).

[71] Halpin J. C, Tsai S. W, 'Environmental factors in composite materials design'; US Air Force Technical Report AFML TR 67–423 (1967).

[72] ANSYS, Version 7.1, Canonsburg (PA): SAS IP (2001).

[73] Hashin Z, Rosen W. B, 'The elastic moduli of fiber-reinforced materials'; Journal of Applied Mechanics, 31, 223–32 (1964).

[74] http://invsee.asu.edu/nmodules/Carbonmod/crystalline.html.

[75] Salvetat J, Briggs A. G. D, Bonard J, Bacsa R, Kulik A. J., Stöckli T, Burnham N. A, Forró L, 'Elastic and shear moduli of single-walled carbon nanotube ropes'; Physical Review Letters; 82 (5), 944-7 (1999).

[76] Kis A, Csanyi G, Salvetat J, Thien L, Couteau E, Kulik A. J, Benoit W, Brugger J, Forró L, 'Reinforcement of single-walled carbon nanotube bundles by intertube bridging'; Nature Materials, 3, 153-6 (2004).

[77] J. M. Gere and S. P. Timoshenko, 'In Mechanics of Materials'; PWS-KENT, Boston (1990).

[78] Gommans H. H, Alldredge J. W, Tashiro H, Park J, Magnuson J, Rinzler A. G, 'fibers of aligned single-walled carbon nanotubes: Polarized Raman spectroscopy'; J Applied Physics, 88, 2509–14 (2000).

[79] Pipes R. B, Hubert P, 'Scale effects in carbon nanostructures: self-similar analysis'; Nano Letters, 3 (2), 239-43 (2003).

[80] Whitney J. M, McCullough R. L, 'Micromechanical materials modeling', Vol. 2 Technomic Publishing Company (1990).

[81] Daniel I. M, 'Engineering mechanics of composite materials', Oxford University Press (1994).

[82] Van Krevelen D.W, 'Properties of polymers' Elsevier, third edition (1994).

[83] Mora M, 'Micromechanics of defects in solids', Kluwer Academic (1987).

[84] Clyne T. W, Withers P.J, 'An introduction to metal matrix composites', Cambridge University Press (1995).

[85] Mori T, Tanaka K, 'Average stress in matrix and average elastic energy of materials with misfitting inclusions'; Acta Metallurgica, 21, 571–4 (1973).

[86] Qui Y. P, Weng G. J, 'On the application of Mori–Tanaka's theory involving transversely isotropic spheroidal inclusions'; International Journal of Engineering Science, 28 (11), 1121–37 (1990).

[87] Eshelby J. D, 'The determination of the elastic field of an ellipsoidal inclusion, and related problems'; Proceedings of the Royal Society of London, Series A 1957, A241, 376–96.

[88] Odegard G. M, Frankland S. J. V, Gates T. S, 'The effect of chemical functionalization on mechanical properties of nanotube/polymer composites'; ASME Conference, 7-10 April, Norfolk, Virginia (2003).

[89] Li Y, Kinloch I. A, Windle A. H, 'Direct spinning of carbon nanotube fibers from chemical vapor deposition synthesis'; Science, 304, 276-8 (2004).

[90] http://nanotech-now.com/

Appendix 1

Carbon Atomic Structure

Carbon has 6 electrons, 4 of the electrons are in its valence shell also called outershell (Figure A1.1). The circles in this figure show the energy levels, representing increasing distances from the nucleus. As can be seen here, carbon's nucleus contains 6 protons and 6 neutrons. This diagram is, however, a simplification and can be misleading. It gives the impression that the electrons are circling the nucleus in orbits like planets around the sun. Actually it is not possible to know exactly where the electrons are located.

A more realistic representation of carbon atom is by using an energy level graph shown in Figure A1.2. Here we see carbon has six electrons represented by arrows (the direction of the arrow represents the electron spin). Two electrons are found in the *1s* orbital close to the nucleus. The next two will go into the *2s* orbital. The remaining ones will be in two separate *2p* orbitals. Therefore, electronic structure of a carbon atom is $(1s)^2(2s)^2(2p)^2$. This is because the *p* orbitals have the same energy and the electrons would rather be in separate orbitals. In general, when reacting, one of *2s* electron jumps to $2p_z$. Thus, it would be possible for carbon to form 4 bonds. In diamond these four electrons makes four sp^3. However, in graphite these four electrons make three sp^2 while the remaining *p* (p_z) makes week van der Waals between graphite layers. The actual location of electrons cannot be determined with certainty and the electrons appear to be 'smeared' into orbitals.

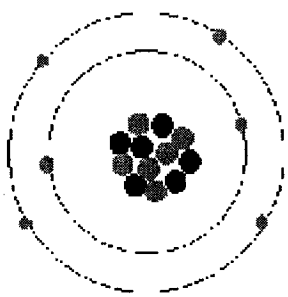

Figure A1.1 Electrons in a carbon atom.

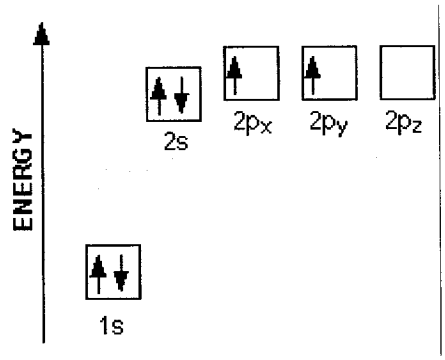

Figure A1.2 Carbon energy level graph.

Appendix 2

Relations between Elastic Constants

Since both carbon nanotube crystals and twisted carbon nanotube/polymer fibers are orthotropic with transverse isotropy, five constants are enough to represent the fiber elastic behavior. Here, we summarize the relations between the engineering constants (E_{11}, E_{22}=E_{33}, G_{12}, υ_{12}, υ_{23}= υ_{32}) and the elastic constants [79].

$$v_{21} = v_{31} = \frac{v_{12} E_{22}}{E_{11}} \tag{A2.1}$$

$$\Delta = \frac{1}{E_{11} E_{22}^2} \begin{vmatrix} 1 & -v_{21} & -v_{21} \\ -v_{12} & 1 & -v_{23} \\ -v_{12} & -v_{23} & 1 \end{vmatrix} \tag{A2.2}$$

$$C_{11} = \frac{1 - v_{23}^2}{\Delta E_{22}^2} \tag{A2.3}$$

$$C_{22} = C_{33} = \frac{1 - v_{12} v_{21}}{\Delta E_{22}^2} \tag{A2.4}$$

$$C_{12} = C_{21} = C_{13} = C_{31} = \frac{v_{12} + v_{12} v_{23}}{\Delta E_{11} E_{22}} \tag{A2.5}$$

$$C_{23} = C_{32} = \frac{v_{23} + v_{21} v_{12}}{\Delta E_{11} E_{22}} \tag{A2.6}$$

$$C_{55} = C_{66} = G_{12} \tag{A2.7}$$

$$C_{44} = G_{23} = \frac{C_{22} - C_{23}}{2} \tag{A2.8}$$

As can be seen here, G_{23} is a function of other engineering constants.